ILMATIETEEN LAITOS
METEOROLOGISKA INSTITUTET
FINNISH METEOROLOGICAL INSTITUTE

138
CONTRIBUTIONS

EVOLUTION OF SEA ICE COVER: RESULT OF INTERPLAY BETWEEN DYNAMICS AND THERMODYNAMICS

ANNU OIKKONEN

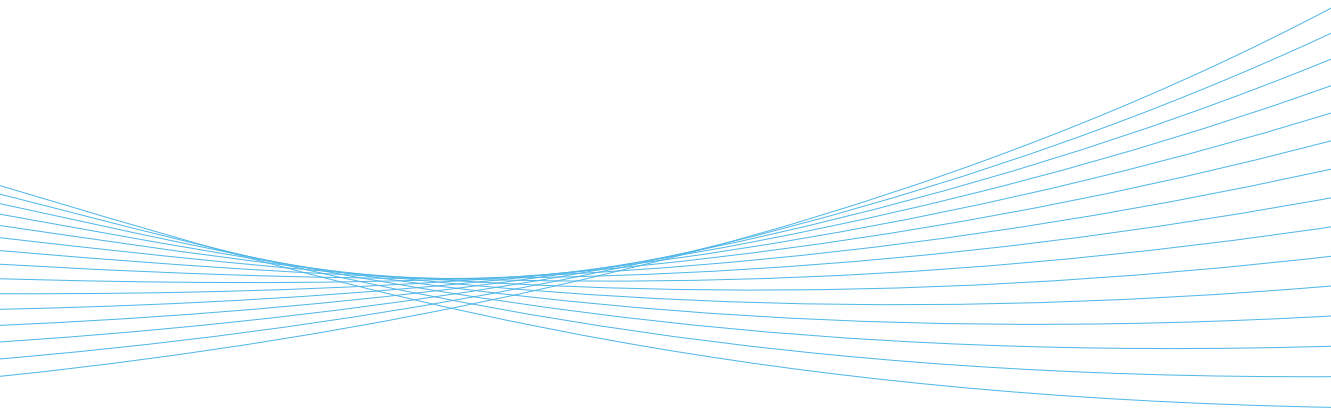

FINNISH METEOROLOGICAL INSTITUTE
CONTRIBUTIONS

No. 138

EVOLUTION OF SEA ICE COVER:
RESULT OF INTERPLAY BETWEEN DYNAMICS AND THERMODYNAMICS

Annu Oikkonen

Department of Physics
Faculty of Science
University of Helsinki
Helsinki, Finland

ACADEMIC DISSERTATION in geophysics

To be presented, with the permission of the Faculty of Science of the University of Helsinki, for public criticism in auditorium Aura (Erik Palménin aukio 1, Helsinki) on 9 November 2017, at 12 noon.

Finnish Meteorological Institute
Helsinki, 2017

ISBN 978-952-336-034-1 (paperback)
ISBN 978-952-336-035-8 (pdf)
ISSN 0782-6117

Erweko
Helsinki 2017

FINNISH METEOROLOGICAL INSTITUTE

Published by	Serier title, number and report code of publication	Date
Finnish Meteorological Institute Erik Palmenin aukio 1, P.O.Box 503 00101 Helsinki	Finnish Meteorological Institute Contributions 138, FMI-CONT-138	November 2017

Author

Annu Oikkonen

Title

Evolution of sea ice cover: Result of interplay between dynamics and thermodynamics

Abstract

The state of the sea ice cover results from an interplay between thermodynamics and dynamics. Changes in the ice cover further affect the way in which the ice responds to forcing, both thermodynamic and dynamic. This thesis discusses several aspects of sea ice thermodynamics and dynamics, and their contribution to the evolution of ice pack, and particularly to changes in the Arctic sea ice cover. The main focus is on the ice dynamics in different types of ice zones and under different conditions, which also enables the examination of the impact of thermodynamic forcing on sea ice dynamics.

Changes in the Arctic sea ice thickness distribution during the period 1975-2000 are studied in detail, and the contribution of thermodynamics and dynamics as driving forcing is discussed. The results show that the shape of the sea ice thickness distribution has changed: the peak of the distribution has generally narrowed and shifted towards thinner ice. A prevalent feature is the loss of thick, mostly deformed ice, which has had a significant role in the decrease in the mean and modal ice thickness. The results also show a decrease in the seasonal variability of the mean ice thickness, but with strong regional differences. Also, the regional variability of the sea ice thickness has decreased, since the thinning has been the most pronounced in regions which formerly had the thickest ice cover. The observed changes in the regional ice draft distributions cannot be explained by local warming of the atmosphere, but changes in the ice drift patterns have had an essential impact. These results emphasize the importance of the description of sea ice dynamics in the models.

Sea ice dynamics, and especially deformation, strongly affect the evolution of ice volume and properties of ice cover. There has still been a need for better understanding of the highly local and intermittent deformation process, as well as its variability that rises from different types of conditions and regions. Several aspects of these questions are covered in this thesis. With coastal and ship radar images, the study of the length scale dependency of sea ice deformation rate is extended to smaller length scales (from 100 m to 10 km) and time scales (from 10 min to 24 h) than were previously possible. Sea ice deformation rate is shown to exhibit a power law with respect to both length scale and time scale at all the scales covered. Both the overall deformation rate and the length scale dependency of deformation rate are found to depend strongly on the time scale considered.

Small scale deformation is studied in different type of ice regions (coastal boundary zone, compact Arctic ice pack and marginal ice zone), and under different weather conditions. One of the key findings is the connection between air temperature and deformation rate: during warm days deformation rates are generally higher than during cold days. The deformation rate is found to respond to changes in air temperature in a time scale of days, which is clearly faster than previously assumed. This response is most likely connected to the effectiveness of the healing process. However, despite of the most effective healing during the coldest winter, the previously damaged areas are found to remain the weak points in the ice cover. This confirms that the deformation history is an important factor in determining how the ice cover responds to dynamic forcing.

FINNISH METEOROLOGICAL INSTITUTE

Publishing unit

Finnish Meteorological Institute

Classification (UDC)	Keywords
551.326.7 551.326 551.467	sea ice, Arctic, Baltic Sea, sea ice thickness distribution, dynamics, thermodynamics, sea ice deformation, length and time scales of deformation, coastal boundary zone

ISSN and series title

0782-6117 Finnish Meteorological Institute Contributions

ISBN	Language	Pages
978-952-336-034-1, 978-952-336-035-8 (pdf)	English	118

FINNISH METEOROLOGICAL INSTITUTE

Julkaisija	Julkaisun sarja, numero ja raporttikoodi	Julkaisuaika
Ilmatieteen laitos Erik Palmenin aukio 1, PL 503 00101 Helsinki	Finnish Meteorological Institute Contributions 138, FMI-CONT-138	Marraskuu 2017

Tekijä

Annu Oikkonen

Nimike

Evolution of sea ice cover: Result of interplay between dynamics and thermodynamics

Tiivistelmä

Merijääpeite muuttuu sekä dynamiikan että termodynamiikan vaikutuksesta. Muutokset jääpeitteessä vaikuttavat edelleen siihen, kuinka merijää reagoi erilaisiin pakotteisiin, niin termodynaamisiin kuin dynaamisiinkin. Tässä työssä käsitellään merijään dynamiikkaa ja termodynamiikkaa sekä niiden osuutta havaituissa muutoksissa Jäämeren jääolosuhteissa. Työ keskittyy erityisesti jään dynamiikkaan eri tyyppisillä alueilla ja erilaisissa olosuhteissa, jolloin myös termodynamiikan vaikutusta dynamiikkaan voidaan tutkia.

Tässä työssä esitetään yksityiskohtaisesti jään paksuusjakauman muutokset Jäämerellä ajanjaksolla 1975-2000, sekä pohditaan termodynamiikan ja dynamiikan merkitystä havaittujen muutosten takana. Tulokset osoittavat, että jään paksuusjakauman muoto on yleisesti muuttunut: jakauman piikki on kaventunut ja siirtynyt kohti ohuempaa jäätä. Huomattavaa on erityisesti paksun, enimmäkseen deformoituneen jään väheneminen. Tällä on ollut suuri merkitys jään paksuuden keskiarvon ja moodin alenemisessa. Useilla alueilla jään keskipaksuuden vuodenaikaisvaihtelu on pienentynyt. Myös alueellinen vaihtelevuus on alentunut jään ohenemisen oltua voimakkainta alueilla, joilla jään paksuus oli suurin tutkimusjakson alussa. Havaittuja muutoksia ja niiden alueellisia eroja ei voida selittää ilmakehän lämpenemisellä vaan jääkentän liikkeellä on ollut merkittävä vaikutus.

Merijään dynamiikka ja erityisesti deformoituminen vaikuttaa merkittävästi jään kokonaismäärään sekä jääkentän ominaisuuksiin. Jääkentän deformoituminen on hyvin paikallinen ja lyhytaikainen ilmiö, jota ei vielä tunneta riittävän hyvin. Alueellisten erojen sekä erilaisten olosuhteiden vaikutusta deformaatioprosessiin ei ole aiemmin juurikaan tutkittu. Tässä työssä näitä kysymyksiä käsitellään usealta kannalta. Rannikko- ja laivatutkakuvia käyttämällä ajojääkentän deformoitumista ja deformaationopeuden pituusskaalariippuvuutta voitiin tutkia pienemissä pituusskaaloissa (100 m – 10 km) ja aikaskaaloissa (10 min – 24 h) kuin aiemmin käytetyillä menetelmillä on ollut mahdollista. Deformaationopeuden todettiin noudattavan potenssilakia sekä pituus- että aikaskaalan suhteen myös näin pienissä skaaloissa. Sekä deformaationopeuden että sen pituusskaalariippuvuuden havaittiin riippuvan voimakkaasti käytetystä aikaskaalasta.

Merijään pienen skaalan deformaatioita tutkittiin erityyppisillä alueilla (rannikkovyöhyke, tiivis ajojääkenttä sekä ajojääkentän reunavyöhyke Jäämerellä) ja erilaisissa sääolosuhteissa. Yhtenä merkittävimpänä tuloksena voidaan pitää löydettyä yhteyttä ilman lämpötilan ja jääkentän deformaationopeuden välillä. Deformaationopeuden havaittiin seuraavan ilmanlämpötilassa tapahtuvia muutoksia muutamana päivän aikajänteellä, mikä on huomattavasti nopeampi vaste kuin aiemmin oletettu. Tämä lämpötilavaste on nopeampi, kuin jään mekaanisen lujuuden vaste lämpötilamuutoksiin. Niinpä havaittu ilmiö on todennäköisesti yhteydessä jääkenttään muodostuneiden vaurioiden (halkeamat ja railot) jäätymisen, ja siten jääkentän lujuuden palautumisen nopeuteen. Vaikka jääkentän vauriot korjautuvat nopeiten kylmien jaksojen aikana, jääkentän deformaatiohistoria vaikuttaa jääkentän käyttäytymiseen myös kylmimmän talven aikana. Laivatutkakuvista nähtiin, kuinka uudet deformaatiotapahtumat saivat aina alkunsa aiemmin vaurioituneista alueista.

FINNISH METEOROLOGICAL INSTITUTE

Julkaisijayksikkö

Ilmatieteen laitos

Luokitus (UDK)	Asiasanat
	merijää, Jäämeri, Itämeri, jään paksuusjakauma, dynamiikka, termodynamiikka, merijään deformaatio, deformaation pituus- ja aikaskaala, rannikkovyöhyke

ISSN ja avainnimike

0782-6117 Finnish Meteorological Institute Contributions

ISBN	Kieli	Sivumäärä
978-952-336-034-1, 978-952-336-035-8 (pdf)	englanti	118

PREFACE

The way to this point where I finally have the thesis completed has not been very straightforward. During the years that it took there have been several projects, working environments and colleagues. All those I would like to thank here.

The first part of the PhD research I did in the geophysics group in the University of Helsinki, under the supervision of professor Matti Leppäranta. This part of the work was funded by Academy of Finland project 122412. I want to thank Matti for giving me that opportunity and excellent working environment. Already during my undergraduate studies, Matti had the key role in introducing me to geophysics and, especially, to fascinating world of the cryosphere. The most of what I know about sea ice I have learned from him.

After couple of years working in the university, I changed to the private sector, to Aker Arctic Technology Inc. I really enjoyed my time there, especially the enthusiastic working atmosphere and the company of the greatest colleagues I could ever imagine. During those numerous hours that I spent in Aker Arctic's ice model test laboratory I also learned a lot about sea ice mechanics in a very practical manner.

The second part of the work leading to this thesis I did in the Finnish Meteorological Institute, under the supervision of research professor Jari Haapala. The work was part of Academy of Finland project 279310. I don't exaggerate at all when I say that without Jari this thesis would have never been completed. He made me an irresistible offer to work in a very interesting project, which also enabled completing my doctoral degree. It was an easy decision to take his offer, since I already knew how amazingly encouraging supervisor, and enthusiastic and competent scientist Jari is.

I thank my co-authors and all other colleagues who have supported me in this work. Especially, I want to express my gratitude to Andrea Gierisch, who has been not only a great office mate, but also helped me with millions of little technical problems I managed to create. Also, the discussions with her helped me seeing what is relevant for this work.

I want to thank the pre-examiners of this thesis, professor Petteri Uotila and professor Jukka Tuhkuri, for their thorough review and encouraging comments.

All the time that I have been doing this PhD research, I have had a privilege to also be a mother. Of course, combining these two roles has been sometimes challenging, but there have been several people making it possible. In addition to my own family, my sincerest thanks goes to Jouko and Anna, and Ritva and Erkki. Also, I want to thank our group leader Eero Rinne for giving me the freedom to find my own working rhythm and spaces, which has made it much easier to combine these different roles in my life. During the most hectic period that was crucial.

Finally, Otso. Tämä on omistettu sinulle.

Annu Oikkonen
Helsinki, November 2017

Contents

LIST OF PUBLICATIONS

I **Oikkonen, A.** and J. Haapala, 2011. Variability and changes of Arctic sea ice draft distribution – submarine sonar measurements revisited, *The Cryosphere*, 5, 917–929, doi:10.5194/tc-5-917-2011

II Leppäranta, M., **A. Oikkonen**, K. Shirasawa and Y. Fukamachi, 2012. A treatise on frequency spectrum of drift ice velocity, *Cold Regions Science and Technology*, 76–77, 83–91, doi:10.1016/j.coldregions.2011.12.005

III **Oikkonen, A**., J. Haapala, M. Lensu and J. Karvonen, 2016. Sea ice drift and deformation in coastal boundary zone, *Geophysical Research Letters„ 43]*, 10303–10,310, doi:10.1002/2016GL069632

IV **Oikkonen, A**., J. Haapala, M. Lensu, J. Karvonen and P. Itkin, *submitted in JGR-Oceans*. Small scale sea ice deformation during N-ICE2015: From compact pack ice to marginal ice zone, *Journal of Geophysical Research Oceans, 122*, 5105–5120, doi:10.1002/2016JC012387

AUTHORS CONTRIBUTION

I The author conducted all the data analysis and wrote the paper. Jari Haapala contributed with valuable comments and suggestions throughout the whole process.

II The author conducted the analyses of observational data from the Baltic Sea and the Sea of Okhotsk. M. Leppäranta was responsible for the modeling work, as well as for the writing of the paper.

III The author conducted all the data analyses, and wrote the paper. Jari Haapala and Mikko Lensu contributed with valuable comments and suggestions throughout the whole process. Juha Karvonen provided assistance regarding the use of his Virtual Buoy tracking method.

IV The author conducted all the data analyses, except for the time series of the distance to ice edge, and wrote the paper. Jari Haapala and Mikko Lensu contributed with valuable comments and suggestions throughout the whole process. Juha Karvonen provided assistance regarding the use of his Virtual Buoy tracking method. Polona Itkin provided the time series of the distance to ice edge and gave useful comments about the manuscript.

1 Introduction

Changes in the Arctic sea ice cover over the past decades have been the topic of numerous studies. The evolution of ice cover is driven by the atmosphere and ocean, but the response of sea ice to certain forcing depends on several properties of the ice pack as well as on geographical constraints, and exhibits large seasonal and regional differences. As the Arctic sea ice cover is changing, its response to forcing may change from what has been known before. The contribution of all the mechanisms interplaying in this complex system is not yet fully understood.

This thesis discusses several aspects of sea ice thermodynamics and dynamics, and their contribution to the evolution of the ice pack, and particularly to changes in the Arctic sea ice cover. The main focus is on the ice dynamics in different types of ice zones and under different conditions, which also enables the examination of the impact of thermodynamic forcing on sea ice dynamics.

The state of the Arctic sea ice cover is most commonly studied in terms of ice thickness, extent and circulation. All these variables exhibit large natural variability in seasonal to decadal time scales, and they have also been showing distinct trends during the recent decades. Interannual variation is largely driven by large scale atmospheric circulation, which affects the sea ice circulation patterns, as well as the surface heat balance through the changes in heat and moisture transport from mid-latitudes. The state of the atmospheric circulation is commonly described by climate indeces. The Arctic oscillation (AO) index is related to the magnitude of zonal circulation in the Arctic. The variation of AO has been found to have a significant impact on variations of Arctic sea ice circulation, thickness and extent (Rigor et al., 2002). Figure 1.1 shows how years with a high AO index result in a weakened Beaufort Gyre and a westward-shifted Transpolar Drift (Rigor et al., 2002). Years with a high AO index are also connected to increased cyclone activity (Serreze et al., 1997) and warmer air temperature (Thompson et al., 2000). Together all these factors lead to a decrease in ice volume during high AO index years.

A clear decrease in the Arctic sea ice thickness has been reported in numerous studies since the 1990s. Since then, the thinning has continued and

even accelerated. Rothrock et al. (2008) found a decline of 36% in the annual mean thickness from 1975 to 2000. When compared to 2012, the decrease of annual mean ice thickness is clearly even greater: from 3.6 m in 1975 to 1.3 m in 2012, resulting in thinning of 65% (Lindsay and Schweiger, 2015). During the satellite era (from 1979 onwards) the Arctic sea ice extent has decreased by a trend of -4.1% decade^{-1} (Cavalieri and Parkinson, 2012). The strongest decrease, -13.4% decade^{-1}, is found in September, which is the month of the annual minimum extent (Figure 1.2a) (Perovich et al., 2016). Also, the Arctic sea ice has become younger and the fraction of multiyear ice (MYI) smaller (Figure 1.2b) (Perovich et al., 2016). This thinner and younger Arctic sea ice cover has been found to drift faster and deform at a higher rate (Rampal et al., 2009; Spreen et al., 2011). Olason and Notz (2014) showed that this acceleration of ice drift has been strongest in summer (Figure 1.3).

Changes in the ice cover result from, and also cause, changes in the atmosphere and ocean. In the Arctic, air temperature has increased at over double rate when compared to the lower latitudes (Overland et al, 2016). The melt season in the Arctic has lengthened at a rate of 5 days decade^{-1}, which has led to an increase in the solar heat stored in the upper ocean by approximately 752 MJm^{-2} (Stroeve et al., 2014). This additional heating has increased the sea surface temperatures by 0.5 to 1.5°C. Warmer sea surface temperatures can be a driver of intensified cyclonic activity in the Arctic due

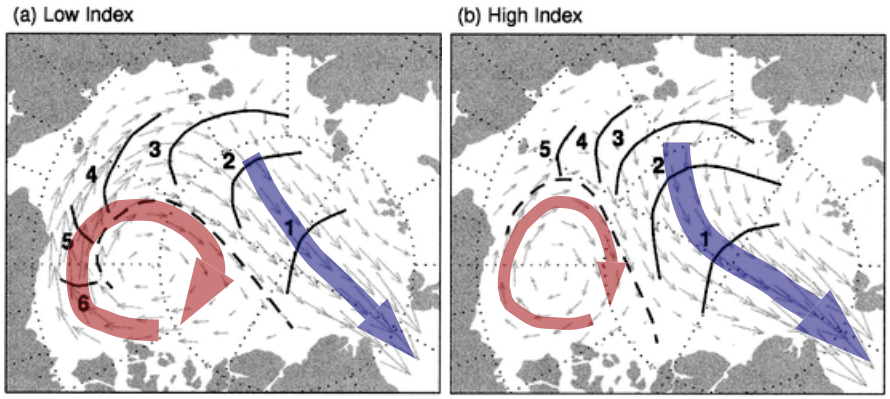

Figure 1.1: The mean circulation of Arctic sea ice during the phases of (a) a low and (b) a high AO index. Isochrone lines show the number of years required for a parcel of ice to exit from the Arctic through the Fram Strait. The dashed line delimits the area in which ice either recirculates in the Beaufort Gyre (highlighted with red) or is advected through the Fram Strait in the Transpolar Drift (highlighted with blue). Modified from Rigor et al., 2002.

to larger heat fluxes from the ocean to the atmosphere in the marginal ice zones (Inoue and Hori 2011).

During the past decades both the thermodynamics and the dynamics in the Arctic have changed due to changes in the atmosphere and ocean, but the role and importance of these different types of forcing mechanisms on recorded changes of Arctic sea ice cover is not fully understood. The connection between thermodynamics and sea ice volume is obvious as the increased heat in the atmosphere and ocean reduces ice growth and enhances melting, but sea ice dynamics are known to have a significant impact as well. During winter, dynamics increase sea ice volume notably via both the formation of thick pressure ridges and the opening of leads. Lead opening results in rapid ice growth, and seasonal ice production in leads is estimated to account for 25-40 % of the total ice production of the Arctic Ocean (Kwok, 2006). In summer, leads have the opposite impact to their impact in winter as the presence of open water increases the absorption of solar heat and enhances the melting. Even in areas with persistent convergence, and thus very infrequent lead openings, dynamics are important for ice volume. Kwok and Cunningham (2016) estimated that deformation explaines over 30% of the overall variance in monthly thickness changes north of the coasts of Greenland and the Canadian Arctic Archipelago.

The complexity of the system is not limited to the combined impact of thermodynamics and dynamics on sea ice volume described above. A change in one forcing mechanism can lead to a change in some ice property, which can further affect the response that ice pack has to this particular, or some

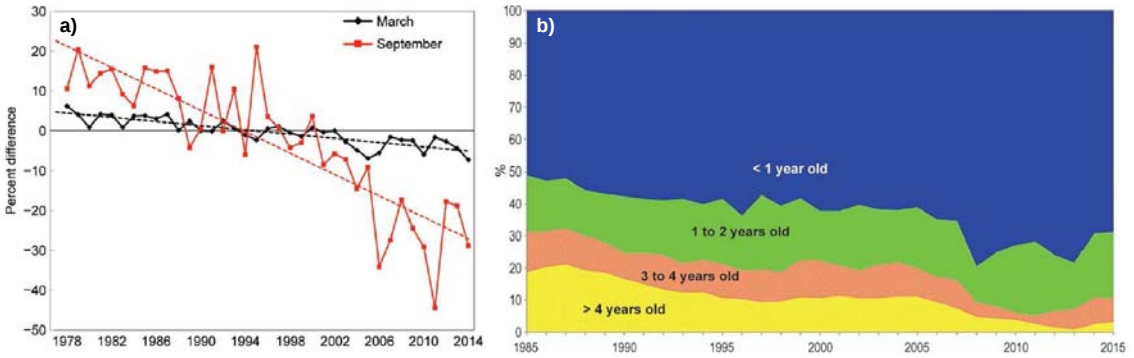

Figure 1.2: a) A time series of the sea ice extent anomaly in March (the month of maximum extent) and September (the month of minimum extent). The anomaly value represents the difference (in %) in the ice extent relative to the mean values for the period 1981-2010. b) A time series of ice age. From Perovich et al., 2016.

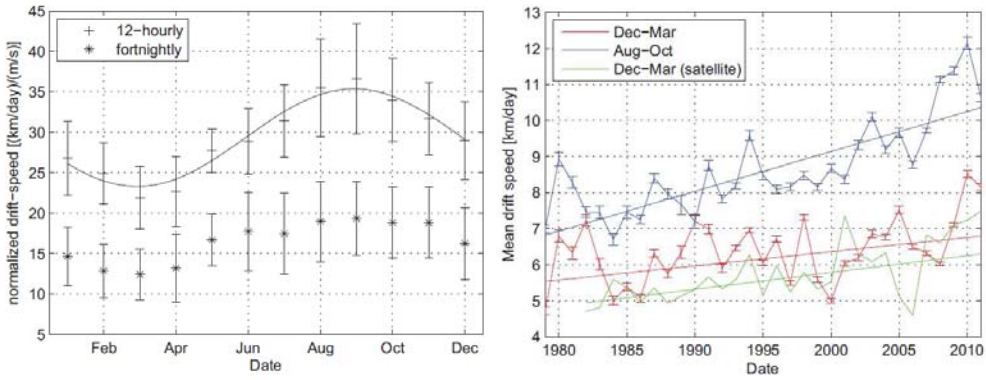

Figure 1.3: The seasonal cycle (left) and long-time trend (right) of Arctic sea ice drift speed obtained from drifting buoys. The seasonal cycle is shown as a monthly mean drift speed with 12 hour interval and with two week interval. The long-term trend is calculated separately for winter (December-March, red) and summer (August-October, blue). For winter, drift speed obtained from satellite images is also shown (green). From Olason and Notz, 2014.

other, forcing. For instance, thermodynamic-driven thinning of ice reduces its ability to resist dynamic wind forcing and makes it more sensitive to drift and deform. Another example is the impact of fracturing under dynamic forcing, which lowers the ice pack strength and makes it more vulnerable to further deformations. A result of this complexity is shown for instance by Olason and Notz (2014). They conclude that although the Arctic sea ice drift is wind driven, the principle drivers of variation and trends in drift speed (Figure 1.3) are sea ice concentration and thickness, but with seasonal variation in their contribution. Also, the fracturing of ice cover and localization of deformation were found to be important drivers of the drift speed variation in spring.

Sea ice fracturing and deformation is known to be a very localized and intermittent process. Mechanical failure of the ice generates a pattern of faults. Fracturing events only last a few minutes (Marsan et al., 2011) and occur along faults in the order of tens of meters (Schulson, 2004). In the scales above these, the sea ice deformation rate (ϵ) follows the power law with respect to both length (L) and time scale (τ): $\epsilon \sim L^{-\beta}$ and $\epsilon \sim \tau^{-\alpha}$. An important feature of the power law is the invariance of the exponent with respect to changes in scales. This implies that there is no characteristic scale, but all the scales are linked. Previous studies on sea ice deformation have covered length scales $\sim$ 10-1000 km, and the power law has been found

for this entire range (e.g. Marsan et al., 2004; Stern and Lindsay, 2009; Hutchings et al., 2011; Hutchings et al. 2012). The power law describes how the deformation rate depends on the length or time scale. The downscaling of the obtained power law has predicted very high deformation rates at small scales, supporting the view that a substantial part of the deformation is brittle (Marsan et al., 2004; Stern and Lindsay, 2009). However, previous studies based on drifting buoys or satellite images have not been able to cover length scales smaller than ∼10 km or time scales smaller than ∼1 h, and so far estimations of small scale deformation have been based on downscaling from larger scales.

In sea ice modelling, a wide variety of different kinds of approaches have been used in attempts to describe this complex physical system with several feedback mechanisms. In general, climate models have not been able to capture the fast decline in the sea ice extent, although the new generation climate models (CMIP5 models, used for the Intergovernmental Panel on Climate Change (IPCC) Fifth Assessment Report in 2013) depict the declining trend better than the earlier CMIP3 models (used for the IPCC Fourth Assessment Report in 2010) (Figure 1.4). Rampal et al. (2011) showed that

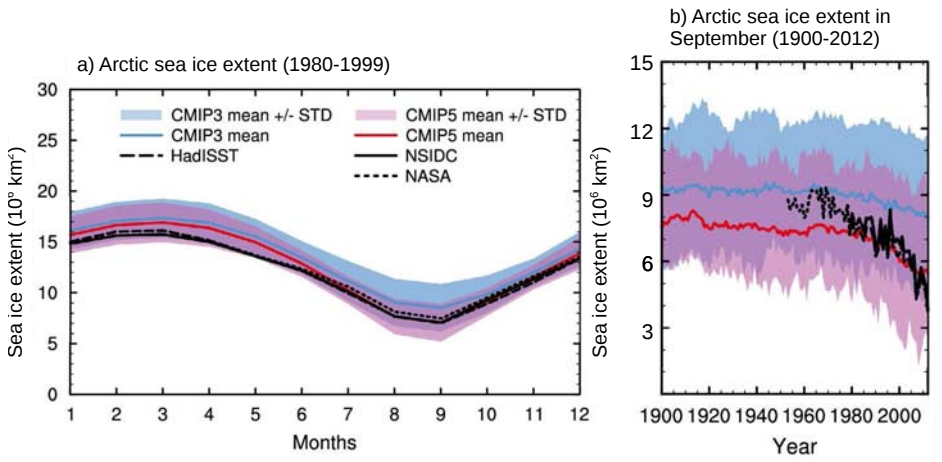

Figure 1.4: Arctic sea ice extent obtained from observations and climate models. a) The annual cycle of the ice extent and b) the September ice extent during the period 1900-2012. The results from CMIP3 models are shown in blue (the line shows the mean, the shadowed area mean±standard deviation) and the results from CMIP5 models are shown in red. The extents obtained from satellites have been provided by National Snow and Ice Data Center (NSIDC), National Aeronautics and Space Administration (NASA) and Hadley Center (HadISST). From Flato et al. (2013).

climate models underestimate the decrease in ice extent and thickness, as well as the increase in ice kinematics, partly due to the weak coupling between ice state (thickness and concentration) and kinematics. This, together with the studies showing the importance of brittle deformation (Marsan et al., 2004; Stern and Lindsay, 2009), has driven more attention to model's ability to represent the heterogeneity of sea ice deformation. Traditionally in modelling sea ice has been seen as a continuum, but the importance of brittle deformation has encouraged the idea that sea ice would be better described with fracturing mechanics instead of continuum mechanics (Stern and Lindsay, 2009; Girard et al., 2011).

Overall, a realistic description of the dynamics and deformation is essential for models to reproduce the evolution of sea ice cover correctly. This study deepens the understanding of seasonal and even shorter time scale variations in the properties of ice cover, and their impact on sea ice drift and deformation. Also, the examination of sea ice dynamics and the scale dependence of sea ice deformation is extended to smaller length scales ($L > 100$ m) and time scales ($\tau > 10$ min) than previously possible.

The objectives of this study are to:

- determine changes in the Arctic sea ice thickness distribution regionally and seasonally, and to estimate the impact of thermodynamic and dynamic forcing on the observed changes.
- improve the understanding of sea ice drift and deformation by studying them at smaller length and time scales than previously possible.
- examine how sea ice deformation varies in different ice zones.
- study the impact of weather conditions on sea ice drift and deformation.

2 Theoretical background

2.1 THERMODYNAMICS OF SEA ICE

Ice grows and melts vertically as a response to the imbalance between net heat fluxes at the upper and lower boundary, and the internal heat conduction. In general, this can be formulated as a one-dimensional heat equation of ice (Makshtas, 1998):

$$c_i \rho_i \frac{\partial T}{\partial t} = \frac{\partial}{\partial z}\left(k_i \frac{\partial T}{\partial z} + I\right), \tag{2.1}$$

where c_i is heat capacity and ρ_i is density of ice, $T = T(t, z)$ is temperature within ice, t is time and z is vertical distance from the upper surface, k_i is thermal conductivity of ice, and I denotes intensity of internal heating due to short wave radiation penetrating into the ice at the upper surface.

The boundary conditions of the heat equation (2.1) at the upper surface are

$$F_0 = k_i \frac{\partial T}{\partial z} \quad , \quad T_0 < T_f \tag{2.2}$$

$$L_i \rho_i \frac{\partial h}{\partial t} = -k_i \frac{\partial T}{\partial z} + F_0 \quad , \quad T_0 \geq T_f \tag{2.3}$$

where F_0 denotes total heat flux at the upper surface and L_i is latent heat of fusion, and T_0 and T_f are surface temperature and freezing point. The total heat flux at the upper surface, F_0 is a sum of several components:

$$F_0 = (1 - \alpha)F_{SW} - I_0 + F_{LW} \Downarrow - F_{LW} \Uparrow + F_s + F_l. \tag{2.4}$$

Terms of the net heat flux are incoming shortwave radiation (F_{SW}), surface albedo (α), the short wave radiation penetrating into the ice (I_0), downward ($F_{LW} \Downarrow$) and upward longwave radiation ($F_{LW} \Uparrow$), sensible heat flux (F_s) and latent heat flux (F_l). The formulation of the different components can be found in Weeks (2010).

At the lower surface, in the ice-ocean interphase, the boundary condition

of Equation 2.1 is

$$L_i \rho_i \frac{\partial h}{\partial t} = -k_i \frac{\partial T}{\partial z} - F_w, \tag{2.5}$$

where F_w is oceanic heat flux. When ice grows in the ice-ocean interphase, latent heat is released and has to be conducted through the ice and snow to the atmosphere. This conductive heat flux, $F_c = -k_i \frac{\partial T}{\partial z}$, depends on the thermal conductivity of the ice, k_i and the local temperature gradient at the depth z. The temperature profile through the ice is not linear, which makes exact thermodynamic calculations difficult. Only in the case of thin ice or very slow changes in the surface energy balance can the heat conduction be approximated with linear temperature gradient (Eicken, 2003).

As the latent heat released by freezing is conducted upward through the ice thickness, the ice growth rate is strongly dependent on the ice thickness. In the central Arctic, very thin ice can grow over 10 cm per day in winter, while ice with 1 m thickness grows only about 1 cm per day in similar conditions (Thorndike et al. 1975). In summer, melting occurs both at the top and the bottom of the ice, and the melting rate is not thickness dependent. However, ice ridges with deep keels may enhance turbulence and thus increase oceanic heat flux and bottom melting. Since the annual ice growth decreases as ice gets older and thicker but the summer melt remains nearly on the same level, the thickness of MYI approaches so called equilibrium thickness. This equilibrium thickness depends on the local climate and can be taken as the maximum thickness of thermodynamically grown sea ice. Maykut and Untersteiner (1971) estimated the equilibrium thickness of Arctic sea ice to vary from about 3 to 5 m at the end of the growth season.

As Equation 2.5 shows, ice growth depends on the temperature gradient through the ice thickness. In the case of $F_w = 0$, ice grows as long as the temperature gradient exists, that is to say as long as $T_0 < T_f$. Therefore, the surface air temperature (SAT) is naturally an important factor in ice mass balance and often used as a proxy for ice growth. In the central Arctic, oceanic heat flux has typically been very small, about 2 Wm^{-2} (Barry et al., 1993), and ice has reached great thicknesses by thermodynamic growth. Clearly higher values (up to 15 Wm^{-2}) are found in the Pacific sector of the Arctic and in the marginal ice zones (Krishfield and Perovich, 2005). With continued decline in sea ice cover, and enhanced coupling of the atmosphere to the ocean, the impact of oceanic heat flux is likely to also increase in the central Arctic (Carmack et al., 2015).

Snow on top of the ice has a prominent effect on the heat balance and ice growth/melt. Snow has low thermal conductivity. It is an insulator that

lowers the ice growth rate in winter and thus has a decreasing impact on the ice mass balance. In summer, the impact is the opposite: snow shields the ice from direct solar radiation and delays the onset of intense ice melt.

2.2 SEA ICE DRIFT AND DEFORMATION

Sea ice drifts as a response to stresses at both the upper and the lower surface caused by wind and ocean current, respectively. The equation of the motion of sea ice is (Leppäranta, 2005)

$$\rho h \left[\frac{\partial \boldsymbol{u}}{\partial t} + \boldsymbol{u} \cdot \nabla \boldsymbol{u} + f \boldsymbol{k} \times \boldsymbol{u} \right] = \nabla \cdot \boldsymbol{\sigma} + \boldsymbol{\tau_a} + \boldsymbol{\tau_w} - \rho h g \boldsymbol{\beta} - h \nabla p_a. \quad (2.6)$$

The terms in the Equation 2.6, from left to right, are local acceleration, advective acceleration, Coriolis term, internal ice stress, air stress, water stress, sea surface tilt and air pressure. Bold symbols denote vectors. In the case of a compact ice pack, the dominating terms in the equation of motion are wind and water stresses and internal stress. Air and water stresses are propotional to the square of wind and water velocity relative to the ice surface (McPhee, 1975):

$$\boldsymbol{\tau_a} = \rho_a C_a U_a \boldsymbol{U_a} \quad (2.7)$$

$$\boldsymbol{\tau_w} = \rho_w C_w |\boldsymbol{U_w} - \boldsymbol{u}| (\boldsymbol{U_w} - \boldsymbol{u}). \quad (2.8)$$

ρ_a and ρ_w are air and water density, C_a and C_w are drag coefficient of air and water, $\boldsymbol{U_a}$ and $\boldsymbol{U_w}$ are velocities of surface layer wind and ocean current, and $\boldsymbol{u}$ is velocity of ice. In the case of air stress (Equation 2.7), ice motion has been neglected, since $U_a \gg u$.

Internal ice stress ($\boldsymbol{\sigma}$) represents different types of mechanical interactions in the ice pack. This includes frictional forces between ice floes and shearing, as well as crushing during convergent deformation and ridge formation (Weiss, 2013). Internal ice stresses may be caused by differential winds and currents, and they are generally very difficult to measure and model on the scale of an ice pack. In the case of a compact ice pack, internal ice stress is one of the dominating terms in the equation of motion (Equation 2.6), and resolving it becomes an important question.

Stresses cause deformations of the ice cover. The behaviour of a compact ice pack under internal stress can be described with rheology, which depicts the relationship between stresses and strains. The three basic models of

rheology are the elastic, plastic and viscous models. The maximum strain (displacement per unit length) that a material, here sea ice, can withstand and still return to its original shape is called the yield point. When strain is below the yield point, material deforms under a load but returns to its original shape if the load is removed. This reversible type of deformation is called elastic deformation. In the linear-elastic model, stress is propotional to strain. When strain exceeds the yield point, the original shape cannot be recovered even if the load is removed. This irreversible type of deformation causing permanent damage is called plastic deformation. In the third basic model of rheology, the viscous model, stress depends on the strain rate, and the material behaves like a viscous fluid.

When strain reaches the end of the elastic and the plastic region of the stress-strain curve, fracturing of material occurs. A fracture is the separation of a material into two or more pieces under a stress. There are two types of fracturing, ductile and brittle, and sea ice has been found to exhibit both types depending on the strain rate. At low strain rates, sea ice behaves like a ductile material. As stress increases, a ductile material undergoes considerable plastic deformation before reaching the fracture point. For sea ice, strain can exceed 0.1 without a macroscopic failure (Schulson, 2001). At higher strain rates ($\gtrsim 10^{-4}$ s^{-1}), sea ice is a brittle material (Schulson, 2001). Brittle material fractures rapidly after the end of the elastic region, with fast crack propagation.

The deformation rate of sea ice pack is usually examined using the strain rate tensor of the velocity field. The extent of sea ice cover is so large compared to its thickness, that in sea ice geophysics the strain rate tensor is usually studied in two dimensions on a horizontal plane. This means that deformation is seen as differential horizontal motion. Elastic deformations of sea ice are small and therefore on the geophysical scale fractures, leads or slip lines are usually required for deformation to happen. Elasticity can only become important in the case of thin ice (thickness $\lesssim 0.1$ m), when buckling may also occur.

The two principal components of strain rate are the divergence (ϵ_{div}) and shear (ϵ_{shear}):

$$\epsilon_{div} = \frac{\partial u}{\partial x} + \frac{\partial v}{\partial y}, \tag{2.9}$$

$$\epsilon_{shear} = \frac{1}{2}\left[\left(\frac{\partial u}{\partial x} - \frac{\partial v}{\partial y}\right)^2 + \left(\frac{\partial u}{\partial y} + \frac{\partial v}{\partial x}\right)^2\right]^{\frac{1}{2}} \tag{2.10}$$

where u and v are velocities in the x and y direction. The total deformation rate (ϵ_{tot}) is a product of shear and divergence:

$$\epsilon_{tot} = \sqrt{\epsilon_{shear}^2 + \epsilon_{div}^2}. \tag{2.11}$$

Studies in the Arctic have shown, that shear is typically the dominating mode of deformation (Stern et al., 1995; Stern and Moritz, 2002), but shear and divergence are strongly correlated in space (Weiss and Schulson, 2009; Weiss, 2013). These reflect the typical deformation field where faulting is shear induced but associated with divergence (Weiss, 2013).

Most of the research on sea ice deformation has been based on data recorded with drifting buoys (Rampal et al., 2008; Hutchings et al., 2011; Hutchings et al., 2012) and satellite-derived RADARSAT Geophysical Processor System (RGPS) data (Marsan et al., 2004; Kwok, 2006; Stern and Lindsay, 2009). The strain rate is typically calculated following areas formed by objects in the ice field. These objects can be buoys or features recognizable in satellite images, and the areas are obtained by connecting three or more of the objects. In addition to the strain rate tensor, the sea ice deformation rate has also been resolved by the dispersion of drifting buoys (Rampal, 2008).

The sea ice deformation rate is found to exhibit a power law with respect to the length scale L

$$\epsilon_{tot} \sim L^{-\beta}. \tag{2.12}$$

This means that the mean deformation rate (ϵ_{tot}) is related to the scale (L) over which it is measured with exponent β. An example of this length scale dependency of the sea ice deformation rate is shown in Figure 2.1. With RGPS data, length scales of 10 to 1000 km have been covered with a time scale of 3 days, while with drifting buoys deformation rates have been resolved for length scales ranging from few kilometers to 100 km, with a time scale of 1 h. The scaling law has been found to hold for the entire range of length scales covered. β is reported to be in the range of 0.2 to 0.5, with seasonal and regional variation. β has been found to be larger in magnitude in summertime than in wintertime (Marsan et al., 2004), and in the areas with a low MYI fraction (Stren and Lindsay, 2009).

As the scaling law (Equation 2.12) applies to all length scales up to the basin scale, there is no characteristic length scale associated with deformation over the length scales studied (Weiss, 2013). Girard et al. (2009) concluded that this is an indication of long-range elastic interactions in the ice cover, which enables stresses to be transmitted over very long distances. The value of the scaling exponent β can been seen as an indication of over how long

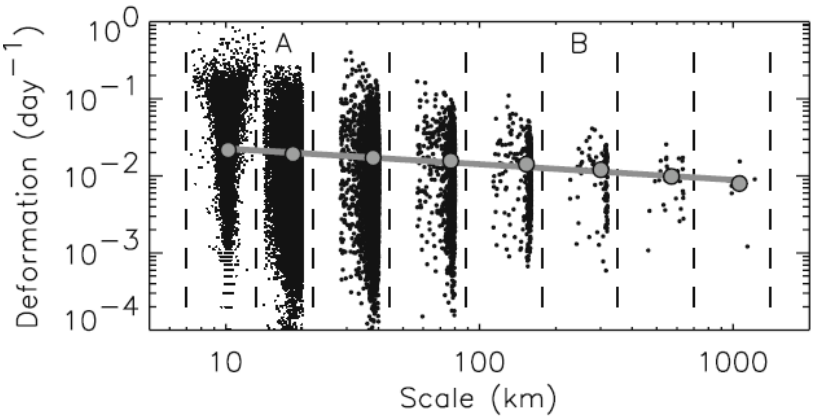

Figure 2.1: The length scale dependency of the sea ice deformation rate from RGPS data (with a 3-day time interval). The small black dots are the deformation rates of RGPS grid cells and grey circles denote the mean deformation rates of the size groups (separated with vertical dashed lines). The power law exponent β is the slope of the line fitted to the size group mean deformation rates in this log-log space. From Marsan et al. (2004).

distances internal stress is transmitted. The smaller in magnitude β is, the further the internal stresses are transmitted. Thick MYI transmits stresses further than thinner first year ice (FYI), just as a compact winter ice pack does when compared to looser summer ice cover, corresponding to the differences in β found between perennial and seasonal ice pack (Stren and Lindsay, 2009) and between winter and summer (Marsan et al., 2004).

As described earlier, the failure of sea ice depends on the strain rate and transits from ductile to brittle when $\epsilon_{tot} > 10^{-4}$ s^{-1} (Schulson, 2001). Based on the length scale dependency (Equation 2.12), deformation rates can be predicted for smaller scales than those covered with observations. This type of downscaling was done by Marsan et al. (2004) and Stern and Lindsay (2009), who came to the conclusion that the majority of deformation in the central Arctic is brittle.

In addition to the length scale, the sea ice deformation rate exhibits scaling with respect to the time scale (τ) as well:

$$\epsilon_{tot} \sim \tau^{-\alpha} \tag{2.13}$$

(Rampal et al., 2008; Hutchings et al., 2011; Weiss and Dansereau, 2016). Also, the length scale dependence of sea ice deformation rate is found to depend on the time scale, and the time scale dependence on the length scale, and thus $\beta = \beta(\tau)$ and $\alpha = \alpha(L)$ (Rampal et al., 2008).

Equations 2.12 and 2.13 manifest the localized and intermittent nature of sea ice deformation: the highest deformation rates are measured with small length and time scales. This is due to the heterogeneity of sea ice deformation. The fracturing of sea ice generates a pattern of faults, which have a linear shape (Schulson, 2004). The length of such linear features can extend from tens of meters to hundreds of kilometers and they can be seen in aerial photographs and satellite images of the ice pack. Although fracturing events only last a few minutes (Marsan et al., 2011), the formation of a fault may cause a lead opening also over a clearly longer time scale (hours or even days). Around the faults, velocity gradients are spatially discontinuous and thus shear and divergence are concentrated (Schulson, 2004). Therefore, these zones are often called linear kinematic features (LKF) (Kwok, 2001). In the sea ice deformation field, they can be best captured on small scales. On larger scales they abate as a larger grid cell often contains several of LKFs and within one cell divergence and convergence typically occur simultaneously, for instance. The impact of scales is enhanced as strain has an inverse propotionality to the length scale and strain rate has an inverse propotionality to the time scale.

In sea ice modeling, several different types of rheologies have been used. In the first dynamics models that included rheologies, sea ice was treated as a viscous fluid or a plastic material. In the 1970s, a non-linear elastic-plastic rheology was developed (Coon, 1974). The elastic deformation of sea ice is very small but makes the numerical solution complicated since the strain history must be stored due to the reversible nature of elasticity. Hibler (1979) introduced a non-linear viscous-plastic rheology where small elastic deformation was replaced by viscous behaviour. This made the numerical solution much simpler and viscous-plastic rheology became a standard in sea ice dynamics models. This rheology allows the ice pack to diverge with little or no stress, but resists compression and shearing under convergent conditions.

In the majority of viscous-plastic models, the ice pack strength has a linear dependency on ice thickness and exponential dependence on ice concentration. This approach has some inadequacies in representing the evolution of sea ice cover. Rampal et al. (2011) showed that the climate models with viscous-plastic rheology underestimate the decrease in ice extent and thickness, as well as the increase in ice kinematics, partly due to the weak coupling between ice state and kinematics. On the other hand, the work of Rampal et al. (2013) considered CMIP3 models, and the next generation models (CMIP5 models) have shown better ability in capturing the declining trend as well as the seasonal cycle of the Arctic sea ice extent (Figure 1.4). Recently,

Hutter et al. (2016) showed that with very high resolution (1 km) a large scale sea ice model with viscous-plastic rheology reproduces leads in the ice cover. As the high strain rates are localized along these leads, the modelled sea ice deformation rate follows the power law with respect to both length and time scale, contrary to earlier results obtained with coarser resolutions.

The studies suggesting that the sea ice deformation is largely brittle (Marsan et al., 2004; Stern and Lindsay, 2009) have motivated the development of new a rheological framework. Girard et al. (2011) introduced an elasto-brittle rheology where sea ice is considered as a continuous elastic plate with progressive damages that simulate cracks and leads (Weiss, 2013). In the development and validation of this rheology, high importance has been attatched to the model's ability to represent the heterogeneity of sea ice deformation. Modelled ice deformation fields have been shown to follow similar strong length scale dependence to that found in nature (Bouillon and Rampal, 2015).

2.3 INTERPLAY BETWEEN THERMODYNAMICS AND DYNAMICS

Typically, an ice pack consists of ice floes of different thicknesses which respond differently to similar forcing. Ice thickness affects the response to both thermodynamic and dynamic forcing. As described in section 2.1, the thermodynamic growth rate depends strongly on ice thickness. Also, the ice pack strength is impacted by ice thickness since thicker ice cover can resists higher stresses. Therefore, it is useful to know the relative extent of different ice thicknesses in the ice pack. This is described by ice thickness distribution

$$\int_{h_1}^{h_2} g(h)dh = \frac{1}{R}A(h_1, h_2) \tag{2.14}$$

where R is total area of the region, $A(h_1, h_2)$ is the area within R covered by ice with thickness in the range $h_1 \leq h \leq h_2$ (Thorndike 1975).

Changes in the ice thickness distribution $g(h)$ can be described by the ice conservation equation (Thorndike, 1975):

$$\frac{\partial g}{\partial t} = -\frac{\partial}{\partial h}(fg) - \nabla \cdot (\boldsymbol{u}g) + \Psi. \tag{2.15}$$

The first term on the right hand side governs the thermodynamic changes, as $f(h, \boldsymbol{x}, t) = \frac{\partial h}{\partial t} \mid_{thermal}$ is thermodynamic ice growth or melt rate of ice with thickness h at the location $\boldsymbol{x}$ and time t. The second and third term describe changes due to dynamics. $-\nabla \cdot (\boldsymbol{u}g)$ is divergence, and Ψ redistribution

function, describing how ice changes from one thickness category to another by mechanical deformations.

Thermodynamic ice growth/melt tends to lead to level ice approaching the equlibrium thickness, that is to say to the infinitesimally narrow peak in $g(h)$. The impact of dynamics is the opposite as drift and deformations create extremes: open water and rafting or ridging. The thickest ice is found in ridges, where thickness can exceed 40 m (Wadhams, 1998). In winter, the impact of dynamics also increases the ice volume through the opening of leads, since the open water areas freez quickly. Seasonal ice production in leads is even estimated to account for 25-40 % of the total ice production of the Arctic Ocean (Kwok, 2006). In summer, the impact is the contrary since open water absorbs more solar radiation which enhances the melting.

In the ice conservation equation 2.15, the redistribution function Ψ is the least well known term. It depends on ice strength, ice fracturing mechanism and small scale ice properties. All these are influenced by thermodynamics as well. The term ice strength can be used for the small scale material property of ice, a property that could in principal be measured by applying a load to a block of ice. In this work, this type of strength is called *ice mechanical strength*. Ice strength can be used in a much larger scale context as well, as a property of ice cover. In this sense it describes how high stresses the ice pack can resist before deformations, seen as differential horizontal motion on geophysical scale, occur. This type of strength is here referred to as *ice pack strength*. Ice pack strength depends on several factors, including ice thickness, ice concentration, ice mechanical strength, floe size and previous fractures.

Both of these types of ice strength are impacted upon by thermodynamics. Ice mechanical strength decreases as the temperature of ice increases, which is mostly seen as a seasonal scale variation. This temperature dependence of ice mechanical strength is connected to the salinity of sea ice. When sea ice is formed from saline ocean water, majority of salt is released into the underlying water column, but some brine is captured in between the ice crystals, in brine pockets. The volume of brine pockets depends on the ice temperature, and the colder the ice is the smaller is the brine volume and the higher is the ice mechanical strength. Regarding the ice pack strength the connection to thermodynamics is more complex and comes via changes in ice thickness, ice mechanical strength and concentration. Also, thermodynamics affect the recovery of ice pack strength after previous damages, so-called healing process. There is also a feedback loop between dynamics and ice pack strength. The response of ice cover to dynamic forcing depends on ice pack strength, and if deformation happens, it lowers the ice pack strength and makes the ice cover more vulnerable to further deformations.

During the melt season in summer some new aspects arise in the interplay between dynamics and thermodynamics. Arntsen et al. (2015) showed how the dynamic break up of Arctic sea ice is influenced by meltponds. As melting accelerates, the breaking pattern of floes is strongly affected by the distribution of melt ponds as the breaking occurs along the ponds. Also, the presence of thick ice ridges may enhance melting if the keel of the ridge enhances turbulence in the ice–ocean boundary layer, leading to an increase in oceanic heat flux (Yu et al., 2004).

3 Data and methods

3.1 PAPER I

Paper I is based on upward-looking sonar measurements recorded by submarines of UK Royal Navy and US Navy (National Snow and Ice Data Center, 2006). Upward-looking sonar does not measure the whole ice thickness but the distance from water level to the bottom of the ice, sea ice draft, which corresponds to approximately 90% of the ice thickness. In Paper I, all analyses are made and all results are reported in terms of draft instead of thickness, because an accurate conversion to thickness would require knowledge of sea ice density and ridge geometry, as well as the thickness and the density of the snow cover.

In this study, data from 31 cruises accomplished during the period 1975–2000 is used. Data has been recorded partly in analogue format and partly in digital format. The error in the comparability of these two types of data is ±6 cm (Wensnahan and Rothrock, 2005), which is small compared with draft values that are typically of several meters. Therefore, data collected in both formats is used. The standard deviation of submarine sonar measurements is 25 cm, and measurements are biased by +29 cm compared with the true draft (Rothrock and Wensnahan, 2007).

Draft distributions are calculated with 0.2 m bin width. Examination is conducted separately for autumn (September-October) and spring (April-May), the first including the annual minimum and the latter including the annual maximun of Arctic ice thickness and extent. The whole area covered with the submarine sonar data is divided into six regions (Figure 3.1). The variability of sea ice thickness distribution is studied in seasonal and regional senses, and changes are determined by comparing the periods 1975–1987 and 1988–2000.

The variability of and changes in the Arctic sea ice cover are examined also by calculating sea ice volume. The probability density function of sea ice volume, $g(V)$, is determined following Yu et al. (2004), but as a function of draft ,D, in stead of thickness: $g(V) = g(D)D$. This function is dimensionless and describes the fraction of total ice volume with the draft D. It integrates

to the mean draft

$$\overline{D} = \int_0^\infty V(D)dD \tag{3.1}$$

and corresponds to a volume over a unit area (Yu et al., 2004).

Paper I presents the evolution of three ice categories, which are classified by draft. Category 1 includes all the ice with $D < 2$ m in spring and $D < 1$ m in autumn, consisting mainly of FYI. Category 2 is dominated by MYI, and the upper limit is set at $D = 5$ m. Category 3 consists of ice with a draft of $D > 5$ m and is dominated by deformed ice.

The impact of different forcing mechanisms possibly leading to observed changes is discussed in Paper I. Changes in dynamic forcing are estimated based on observed ice drift using International Arctic Buoy Programme (IABP) buoy data (Rigor, 2002). The mean drift patterns are calculated for the periods 1979–1987 and 1988–2000. IABP operations started in 1979, four years later than the submarine data, and thus the years of the first period in the comparison do not fully match with the years included in draft analyses. Discussion on thermodynamic forcing is based on SAT data in ERA-40 reanalyses (Uppala et al., 2005). Differences in SAT between the two study periods (1975–1987 and 1988–2000) are calculated for the entire Arctic and separately for the preceding months of both seasons considered, in other words for the growth season in winter (November-March) and the melt season in summer (June-August).

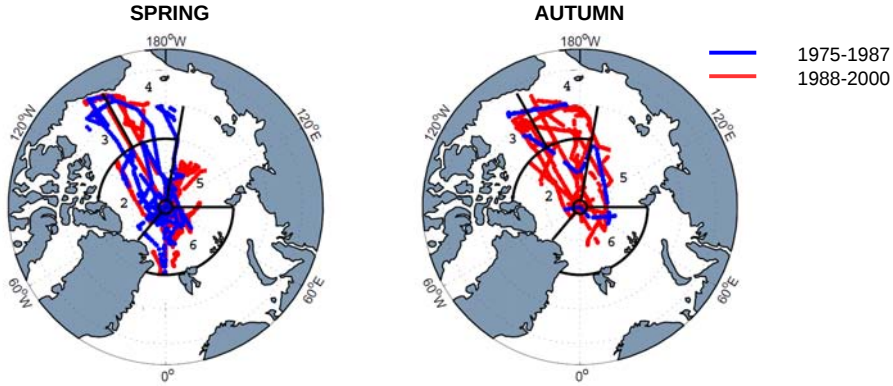

Figure 3.1: The tracks of the submarine cruises accomplished in spring (on the left) and in autumn (on the right) during the periods 1975-1987 (blue) and 1988-2000 (red). The whole study area is divided into six regions: North Pole (1), Canada Basin (2), Beaufort Sea (3), Chukchi Sea (4), Eastern Arctic (5) and Nansen Basin (6). From Paper I.

3.2 PAPER II

In Paper II, sea ice velocity spectra are studied with a mathematical model and observations. Observational data is from the Baltic Sea and the Sea of Okhotsk. In the Baltic, data was recorded during a field campaign aboard R/V Aranda in March 2009 in the Bay of Bothnia. Ice motion is obtained from the positions of the ship when moored to ice. Data from two ice stations (referred to as S2 and S3) are used. The positions (with an accuracy of 5 m) were recorded every 10 s. Ice velocity is calculated from 5 min average positions at the same interval.

Sea ice drift in the Sea of Okhotsk is obtained from drifting buoys and an Accoustic Doppler Current Profiler (ADCP) in winter 2005. Three drifting buoys (referred as buoys #4, #5 and #6) were deployed on sea ice in the coastal zone at Hokkaido. The locations of the buoys were recorded every hour, with positioning accuracy of 10 m. The ADCP was moored in the proximity of the north coast of Hokkaido (position 44°28'N, 143°25'E, depth 48 m). The ADCP used bottom tracking and measured the velocity of ice drifting over the mooring site with a sampling interval of 15 min. The ADCP provides Eulerian ice velocity, while drifting buoys represent the Lagrangian type. Buoy #6 drifted most of the time in the proximity of the ADCP, and the data that was collected less than 100 km away from the ADCP mooring site was used for the comparison of Eulerian and Lagrangian frequency spectra.

3.3 PAPER III

Paper III is mainly based on the coastal radar images from Tankar Island in the Northern Baltic Sea (Figure 3.2). The coastal radar station was established for navigational purposes, but the Finnish Meteorological Institute (FMI) has instrumented it for environmental research. The radar system, as well as the data collection and transmission, is described in more detail by Karvonen (2016). A temporal median filter (15-20 seconds) is applied to the raw data, and in this work these preprocessed images with an interval of two minutes are used. The radar images cover the area of 40×40 kilometers and have the resolution of 33 meters.

Thanks to the high temporal resolution of the images, the trajectories of identifiable sea ice objects can be resolved in sub-pixel scale using the Virtual Buoy (VB) tracking method developed by Karvonen (2016). The error of 2 min VB positions is approximately 6 m. Both sea ice drift and the deformation rate are calculated from the hourly averaged positions of VBs. Hourly averaging redfirst year iceuces the error of VB positions to

Figure 3.2: In Paper III, sea ice drift and deformation rate are obtained using coastal radar images recorded on Tankar Island, in the Bothnian Bay. The area covered with coastal radar images is shown with the red box on the left. An example of coastal radar images is on the right. In Paper III, coastal sea ice dynamics are studied considering alongshore and cross-shore component drift velocity. The positive direction of these is shown with white arrows on the left (x for cross-shore drift and y for alongshore drift).

approximately 1 m.

Paper III focuses on winter 2011. Coastal radar images from the period 15 February to 15 May are used. Interruptions in data collection caused four gaps of 1 to 3 days, and one longer break of 12 days in late April and early May.

The impact of weather conditions on ice drift and deformation rate throughout the season is discussed in Paper III. This is based on hourly recorded wind and air temperature data from the weather station located on the same island as the radar. Ice thickness in the study region was recorded using an air-borne electro-magnetic instrument (EM) during the field campaign running from 2 to 7 March 2011. Due to several ridging events and colder-than-average temperatures in early winter, the ice was thicker than during a typical winter, with the mean thickness of 1.05 m in EM-recordings over the study area. Additional information on ice conditions is obtained from ice charts provided by the FMI Ice Service.

In order to capture the characteristics of ice drift in the coastal boundary zone (CBZ), the study area is divided into 2 km wide bands aligned with the shore. In addition to scalar drift speed, ice drift is examined in alongshore and cross-shore direction. Coastal ice drift is studied on hourly, daily and seasonal scales at different distances from the shore.

The sea ice deformation rate is only calculated for drifting ice pack. For most of the study period, coastal radar images revealed stable fast ice reaching band 6 (12 km off the shore). During the last two weeks of the season (30 April to 13 May), the entire ice field was broken up, and no fast ice area existed anymore. Thereby, the drifting ice pack is defined as the bands > 6 until 30 April, and as the whole area from that date onwards.

For the deformation analyses, triangles are formed from VBs using Delaunay triangulation. Due to the highly variable lifetime of VBs, the triangulation is reset at the beginning of each day. In order to study the length scale dependence of the deformation rate, triangles in six different size groups are always formed. Length scale is determined as a square root of the triangle's area, $L = \sqrt{A}$. The minimum size of triangles is set to $L = 200$ m, which is clearly larger than the smallest length scale for which the deformation rate can be resolved reliably ($L \gg 10$ m, detailed error analysis can be found in the Supporting information of Paper III). The shape criteria of triangles is applied to avoid erroneous high deformation rate values being caused by distorted cells. The minimum angle of a triangle corner included in the analyses is set to 15° .

Deformation rates are resolved using strain rate tensor (Eq 2.9-2.11). Following Bouillon and Rampal (2015), the spatial derivatives in these equations are approximated as

$$\frac{\partial u}{\partial x} = \frac{1}{A}\sum_{i=1}^{n}(u_{i+1} + u_i)(y_{i+1} - y_i), \tag{3.2}$$

$$\frac{\partial v}{\partial y} = \frac{1}{A}\sum_{i=1}^{n}(v_{i+1} + v_i)(x_{i+1} - x_i), \tag{3.3}$$

$$\frac{\partial u}{\partial y} = \frac{1}{A}\sum_{i=1}^{n}(u_{i+1} + u_i)(x_{i+1} - x_i), \tag{3.4}$$

$$\frac{\partial v}{\partial x} = \frac{1}{A}\sum_{i=1}^{n}(v_{i+1} + v_i)(y_{i+1} - y_i), \tag{3.5}$$

where A is the area, i is the index of a corner, n is the number of corner points (3) and $n + 1 = 1$. Unfortunately, in Paper III, the term "deformation" is used in stead of correct term "deformation rate". The strain rate tensor gives divergence, shear and total deformation rate, and they all are dimensionally the reciprocal of time, presented with unit h^{-1} in Paper III.

The length scale dependence of the sea ice deformation rate is examined by determining the exponent of the power law $\epsilon_{tot} \sim L^{-\beta}$. β is obtained from a least square fit to the average deformation rates of the triangle size groups

in log-log space. The quality of the fit is evaluated by several means: the square correlation (R^2), 95% confidence interval and bootstrap method. The bootstrap method is used to obtain the error estimate for β, defined as the standard deviation of β in 10 000 bootstrap repetitions.

In order to study the impact of weather conditions on the deformation rate and its length scale dependence, power law scaling is repeated for selected days with specified conditions. The sensitivity to weather conditions is tested using three different factors: scalar wind speed, cross-shore wind and air temperature. Each factor is studied by comparing cases when this factor is below or above the defined cut-off value. The pairs in comparison are wind speed < 7 m/s versus wind speed > 7 m/s, cross-shore wind < 0 m/s (wind directed off the coast) versus cross-shore wind > 0 m/s (wind directed towards the coast) and air temperature < 0°C versus air temperature > 0°C. For each of the three factors, some additional criteria are applied in order to minimize the effect of other factors.

3.4 PAPER IV

In paper IV, the small scale sea ice deformation rate is calculated using ship radar images recorded during the N-ICE2015 campaign. During the campaign, R/V Lance was frozen in and drifting with the ice pack north of Svalbard. The campaign included four drifting stations (named Floe 1 to 4) and provided data from nearly four months between January and June 2015. The drift tracks of Floes 1 to 4 are shown in Figure 3.3.

Ship radar images are similar to the coastal radar images used in Paper III but with different areal coverage and resolution. The images recorded on board R/V Lance cover an area of 15 km $\times$ 15 km with a resolution of 12.5 m, and they are recorded with a 1 min interval. Similar to Paper III, ice motion is obtained using the VB tracking method (Karvonen, 2016). The error in 1 min positions is approximately 3 m (Karvonen, 2016).

The sea ice deformation rate is calculated similarly to Paper III: forming different sized triangles from VBs, approximating velocity gradients by Equations 3.2-3.5 and calculating deformation rates using Equations 2.9-2.11. In Paper IV, this is done using five different time intervals: 10 min, 1 h, 3 h, 6 h and 24 h. For all the time intervals, 10 min average positions of VBs are used and longer time intervals are obtained through sub-sampling of the 10 min position time series. Another difference compared to Paper III is the reset of triangulation: in Paper IV a new set of triangles is formed at the beginning of each time step. The smallest length scale included in the analyses (the size of the smallest triangles) is 50 m, which is clearly larger than the minimum

length scale ($L = 9$ m) for which the deformation rate can be resolved reliably with defined accuracy of position.

Since the deformation rate is calculated using six size groups of triangles and five time intervals, the power law scaling can be conducted with respect to both length and time scale, $\epsilon_{tot} \sim L^{-\beta}$ and $\epsilon_{tot} \sim \tau^{-\alpha}$.

During N-ICE2015, the ship was drifting within the ice pack and the data covers regions from compact pack ice to the marginal ice zone (MIZ, the part of the ice cover which is close enough to the open ocean to be affected by its presence). Figure 3.3 (right hand side) shows how the distance to ice edge (l) varied from over 300 km to only a few kilometers during the campaign. This allows the examination of the impact of l on the sea ice deformation rate.

In addition to the distance to ice edge, the impact of drift and wind speed as well as air temperature is discussed. Wind speed and direction and air temperature were recorded by a weather station deployed on ice a few hundred meters away from the ship (Hudson et al., 2015). Drift speed and direction are calculated from the recorded ship positions.

The localization of deformations is examined in detail. Localization is evaluated by calculating the fractional area (the percentage of the total area) that accommodates 15% of the largest deformation rates. This is done separately for the total deformation rate, shear and absolute divergence, and for the different time scales.

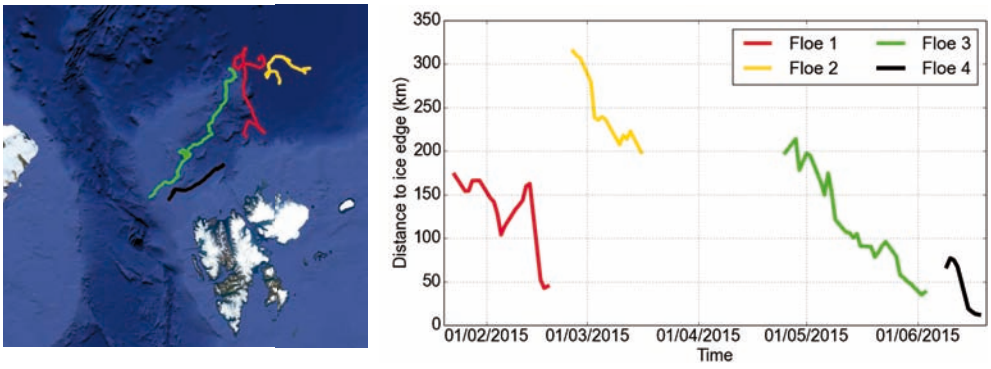

Figure 3.3: In Paper IV, data collected during the N-ICE2015 campaign was used. The drift tracks of four ice stations of N-ICE2015 are shown on the left. The campaign lasted nearly six months. During that time, the location of the ice edge altered. Also, the ice floes followed were drifting, generally towards the ice edge. Therefore, the distance to ice edge varied considerably. The time series of distance to the ice edge is shown on the right.

4 Results and discussion

4.1 CHANGES IN THE ARCTIC SEA ICE THICKNESS DISTRIBUTION

Submarine sonar data has been used in several earlier studies (Rothrock et a., 1999; Wadhams and Davis, 2001; Yu et al., 2004; Rothrock and Zhang, 2005; Rothrock et al., 2008; Kwok and Rothrock, 2009) but the approach in Paper I is different from all of these and reveals a new, more detailed picture of changing Arctic sea ice cover. Previous work has mostly focused on mean ice thickness, and the few that show thickness distribution (Wadhams and Davis, 2001, Yu et al., 2004) are based on a very limited amount of data. In Paper I, Arctic sea ice draft distributions from the period 1975-1988 are compared to the period 1988-2000. The comparison is done for two season, spring and autumn, and for six regions (Figure 3.1), enabling the examination of seasonal and regional variability and changes.

The results show that the peak of the ice draft distribution has generally narrowed and shifted towards thinner ice (Figure 4.1). This has led to a reductions in both mean and modal ice draft. In spring, the modal draft in the Beaufort and Chukchi Seas shifted from the level MYI draft range to values of level FYI. In the Beaufort Sea, the Autumn draft distribution shows a clear change from a bi-modal shape to the dominance of open water and very thin ice, meaning a shift from the typical shape of distribution in perennial ice zone (PIZ) to typical shape in seasonal ice zone (SIZ).

The decrease of mean draft is generally stronger in spring than in autumn. In spring, thinning exceeds 0.6 m decade^{-1} in all other regions except the Nansen Basin and the Chukchi Sea, with maximum change of -1.1 m decade^{-1} in the Eastern Arctic. More modest changes in autumn mean drafts (maximum -0.6 m decade^{-1} in the Canada Basin) led to a decrease in seasonal variability. Regional variability showed a decrease as well since the overall thinning was the most pronounced in the regions which initially had the thickest ice.

As Figure 4.2 shows, the decrease in mean draft is largely due to volume loss in the thickest ice category (ice category 3, $D > 5$m). In spring, the loss

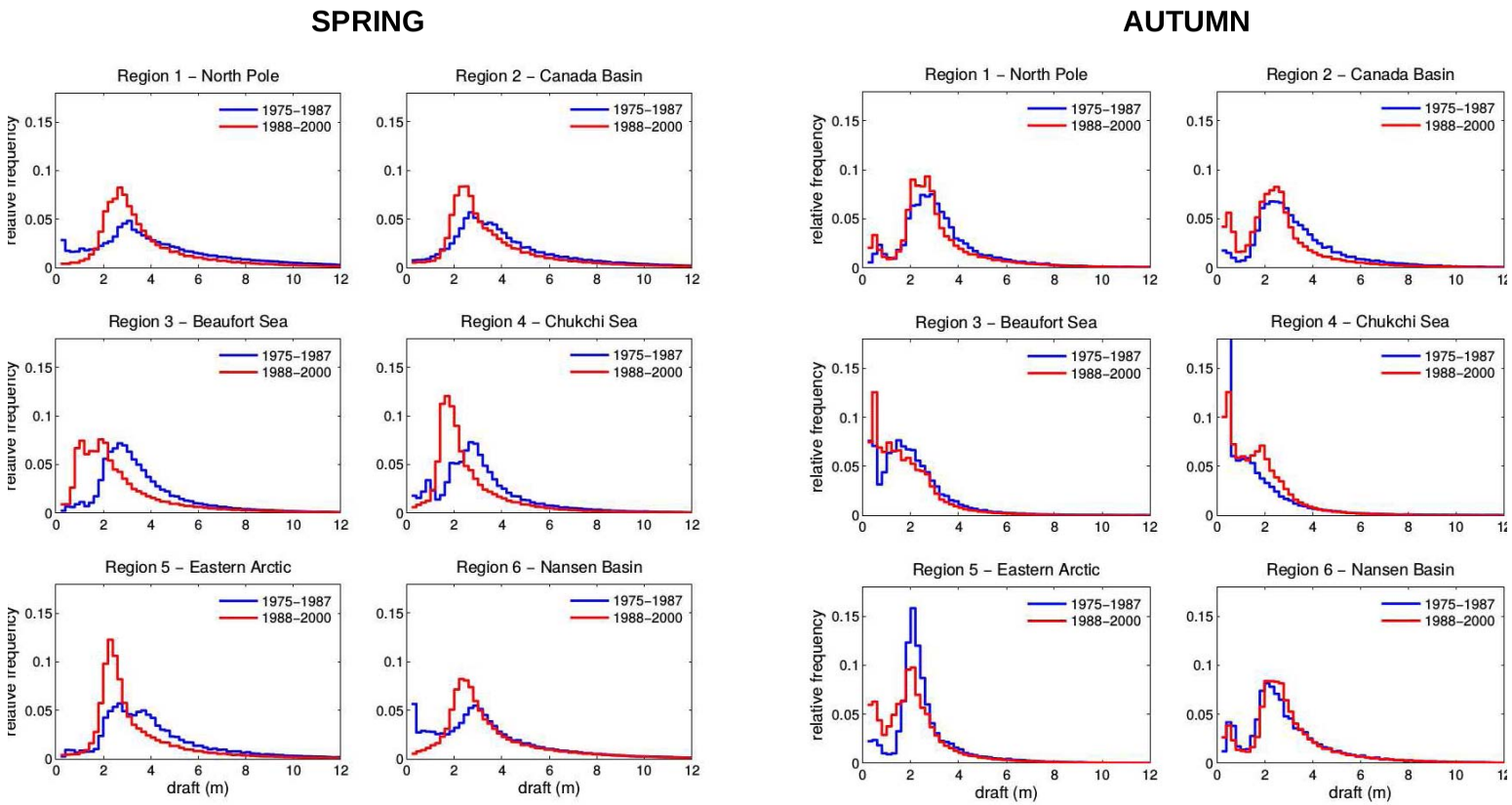

Figure 4.1: Regional sea ice draft distributions in spring (April-May, on the left) and in autumn (September-October, on the right). The period 1975-1987 is presented in blue and the period 1988-2000 is marked with a red line. Distributions are calculated with 0.2 m bins. From Paper I.

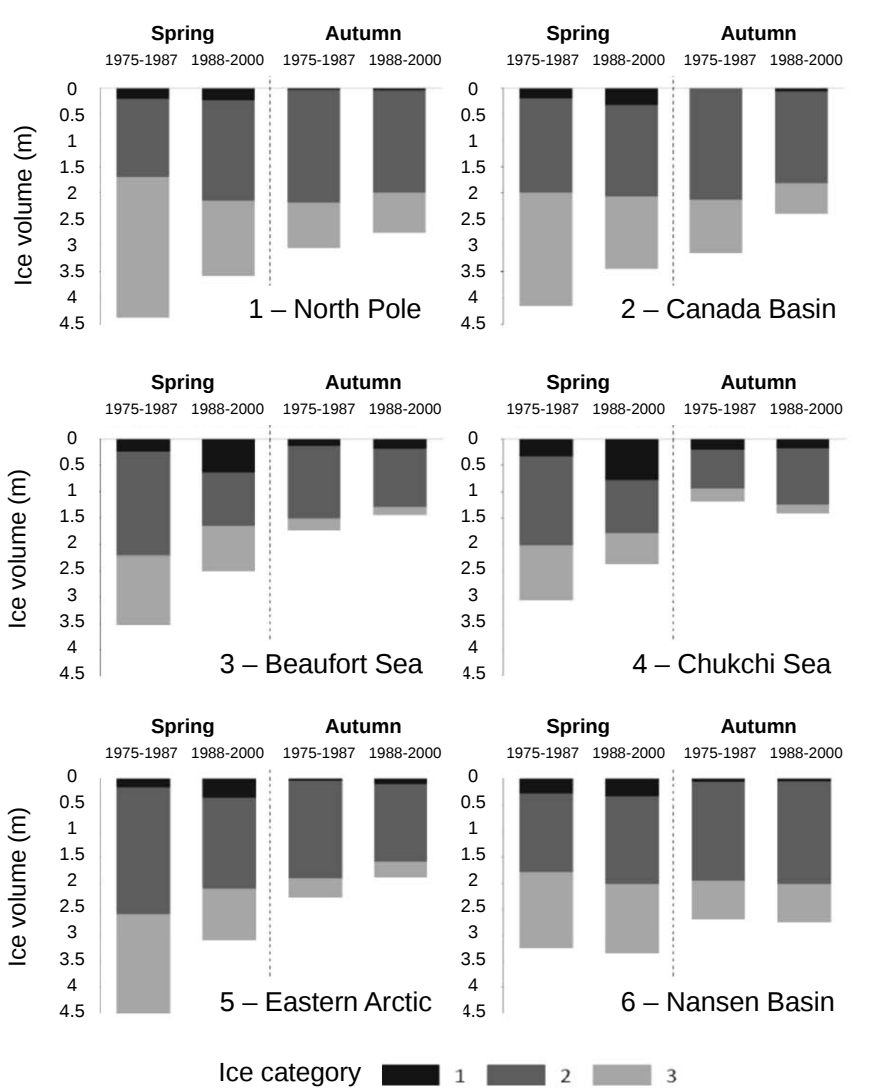

Figure 4.2: Regional mean ice draft and its composition. Ice category 1 includes ice with a draft of < 2 m in spring and < 1 m in autumn, ice in category 2 has a draft of 2-5 m in spring and 1-5 m in autumn, and ice in category 3 has a draft of > 5 m in both seasons. From Paper I.

of the volume in this category exceeds 35% in all regions except the Nansen Basin, and the reduction is over 45% in the North Pole region and the Eastern Arctic. In autumn, the volume of thickest ice category has decreased by over 40% in the Canada Basin, and the reduction is more than 30% in the Beaufort

and the Chukchi Seas as well.

The Beaufort Sea is a region with remarkable changes. The dominance of MYI during 1975-1987 changed to a nearly equal contribution of FYI and MYI in 1988-2000, and the region changed from clearly PIZ towards SIZ. More recent studies have shown that this new state has endured. Richter-Menge and Farrel (2013) estimated, that during the years 2009-2013 ice cover in Beaufort and Chukchi Seas was dominated by FYI, accounting for about 75% of the ice extent.

During the period 1975-2000, the Nansen Basin differed from other regions with very slight changes. Later, clear thinning was also recorded in Fram Strait, at the southern edge of the Nansen Basin. Renner et al. (2014) reported that ice thickness at the end of the melt season decreased by over 50% during 2003–2012.

4.1.1 THE IMPORTANCE OF THERMODYNAMICS AND DYNAMICS

The observed notable changes in the ice draft distribution and composition of Arctic sea ice cover raised a question about the forcing mechanisms behind them. Therefore, the impact of changes in the thermodynamic and dynamic forcing are discussed in Paper I.

SAT can be used as a proxy for energy balance changes in wintertime. The difference in SAT between the two study periods (1975–1987 and 1988–2000) was calculated from ERA-40 re-analyzed data (Uppala et al., 2005). This was done separately for the preceding months in both seasons considered, in other words for the growth season in winter (November-March) and the melt season in summer (June-August).

The changes in surface energy balance in the winter period appear to have only had a modest impact. The later period was only significantly warmer over the land area in Siberia. Over the Arctic Ocean, slight warming (less than 0.5°C) was only observed in the region north of Greenland. In the summer, changes in SAT were negligible over the entire Arctic Ocean. This is to be expected since, as long as the ice cover prevails, SAT is bound to the melting point of ice due to the action of sensible heat flux.

However, the thermodynamic forcing has changed as the length of the melt season has increased in the entire Arctic Ocean (Belchansky et al., 2004). A clear change started in 1989 (Belchansky et al., 2004b), right at the beginning of the later period studied. Therefore, the period 1988-2000 was characterized by enhanced melt and reduced ice growth when compared to the period 1975-1987. Snow fall may have a significant impact on thermodynamics. Although

direct measurements do not exist, it has been estimated that in the regime dominated by cyclonic circulation, which was the case during most of the period 1988–2000, precipitation over the Arctic Ocean increases in all seasons. An increase in snow fall could reduce the ice growth in winter due to insulation and slow down the ice melt in summer due to increased albedo.

All these thermodynamic factors could explain some level of thinning of the Arctic ice cover. However, they do not provide any explanation for the notable regional differences in changes observed from submarine sonar data.

Dynamic forcing was estimated based on the mean drift patterns of IABP buoys during the periods 1979-1987 and 1988-2000 (Figure 4.3). During the former period, the Beaufort Gyre was much stronger than during the later period. Also, there was a westward shift of the Transpolar Drift, and during the later period, a large fraction of ice entering the Fram Strait drifted over the North Pole.

As described earlier, the highest thinning rate was found in the Eastern Arctic (-1.1 m decade^{-1} in spring). This may be explained by the changes in the ice circulation patterns. During the former period, ice from the strong Beaufort Gyre was entering the Eastern Arctic region. During the later period, a larger proportion of the ice advected into this region was coming from the Siberian coast, being thinner FYI. In the western Arctic, the weakening

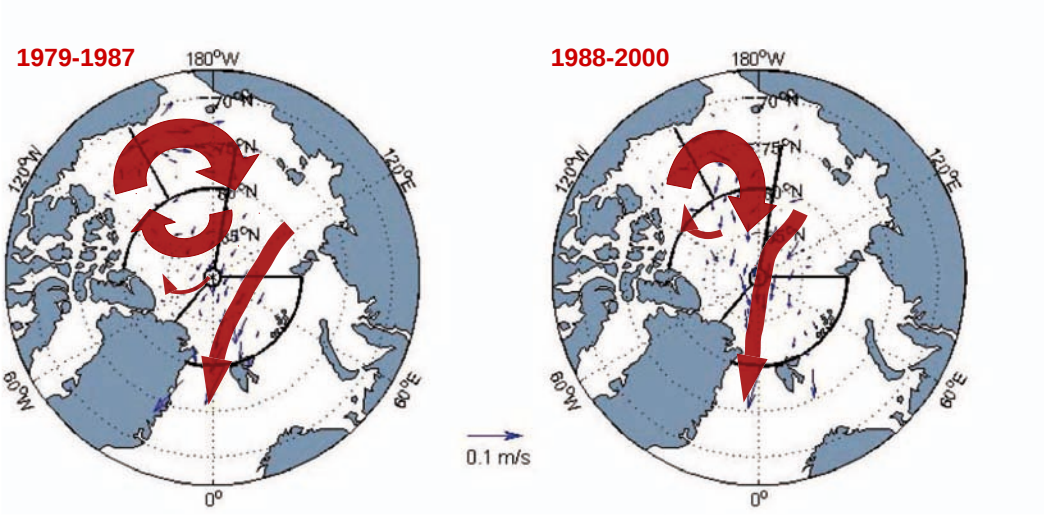

Figure 4.3: Mean ice drift pattern during the periods 1979-1987 and 1988-2000. Drift is calculated from IABP buoys. Modified from Figure 7 in Paper I.

of the Beaufort Gyre led to a decrease in both the average age of the ice and the level of compression and deformation, corresponding to changes in the Beaufort Sea and Canada Basin.

The Nansen Basin showed a very different evolution with nearly unchanged ice conditions. There, the influence of a change in the advection pattern was the opposite compared to that of the Eastern Arctic. During the former period, ice entering the Nansen Basin mostly originated from the SIZ of the Kara and Laptev Seas, while in the latter period advection over the North Pole prevailed as stronger and included more thick ice from the central Arctic and the Beaufort Gyre.

In the Arctic, the large scale ice drift patterns are following changes in the atmospheric circulation patterns. The major atmospheric circulation patterns of the Arctic are well described by the modes of AO and DA (Wang et al., 2009). The AO is related to the magnitude of the zonal circulation. It impacts the Beaufort Gyre, which is stronger during the negative phase of the AO (Rigor et al., 2002). The DA is a measure of the strength of atmospheric meridional circulation from the Pacific sector to the North Atlantic (Wu et al., 2006; Watanabe et al., 2006). The DA has a particularly strong effect on ice conditions during its positive phase. Then it strengthens the Transpolar Drift and ice export through the Fram Strait and enhances the inflow of Pacific water into the Arctic (Wu et al., 2006).

The two study periods (1975–1987 and 1988-2000) have clearly different distributions in the AO/DA-space. Negative AO and DA years dominated the 1975–1987 period. The later period also includes some negative AO and DA years between 1996–2000 but positive AO and DA years prevailed at the beginning of this period. As described earlier, the observed changes in the ice draft distributions were largely related to changes in the ice drift patterns, which, on the other hand, can be seen as a result of changes in the large scale atmospheric circulation.

4.2 ICE DYNAMICS IN THE SEASONAL ICE ZONES OF BALTIC SEA AND SEA OF OKHOTSK

Sea ice dynamics in two SIZs, the Baltic Sea and the Sea of Okhotks, are studied in Paper II and III. In the Baltic Sea, ice drift is wind driven, while in the Sea of Okhotsk permanent current system and tides are important forcing mechanisms in addition to winds. In Paper II, sea ice velocity spectra is shown for both of these areas. These spectra reflect the differences in the forcing: in the Baltic Sea spectra are dominated by synoptic frequencies, while in the Sea of Okhotsk some level of tidal and inertial signals are found.

The data from the Sea of Okhotsk provided a unique opportunity to compare Lagrangian and Eulerian velocity spectra. As described in Paper II, the Eulerian spectrum should theoretically be on a higher level than the Lagrangian one, as it should contain the variance due to variations in the floe characteristics. However, this had not been shown from the observations before, due to the lack of simultaneous Eulerian and Lagrangian velocity measurements of the same region. As one of the buoys utilized in Paper II drifted in the vicinity of the bottom moored ADCP, the comparison between Lagrangian and Eulerian velocities could be done. The results confirmed the hypothesis and the Eulerian spectrum was found to be on a higher level than Lagrangian, with overall fairly similar shape.

Due to the narrow shape of the basins in the Baltic Sea, a substantial part of the ice covered sea area is impacted by the vicinity of the shore. Ice dynamics in the coastal boundary zone (CBZ) is discussed in detail in Paper III. Closest to the shore, where the sea is shallow, CBZ includes an area of fast ice. The fast ice area was found to be stable nearly the entire study period of Paper III, and the edge of the fast ice was reaching about 12 km off the shore. Only during the last couple of weeks of the ice season, the entire ice cover in the range of coastal radar was broken up and drifting.

Outside of the fast ice area, ice drift speed increases strongly when going further from the shore. This area with strong velocity gradient is called shear zone and it is clearly visible in Figure 4.4 (bands 7 to 10, i.e. 12 to 20 km off the shore). Overall, the drift outside of the fast ice area was anisotropic and the average magnitude of the alongshore drift was nearly double compared the to cross-shore drift. As Figure 4.4 shows, this anisotropy was clear in the shear zone, where alongshore drift speed increased faster than the cross-shore speed. However, the difference between alongshore and cross-shore components was nearly equally strong still in the outermost bands (20 to 30 km off the shore). Examination of the wind velocities suggests that this asymmetry is not wind induced, but a characteristic of the CBZ. An impact of the coast reaches further than just the shear zone, and this entire area where the influence of the coast can bee seen is here defined to be part of the CBZ.

As Figure 4.4 shows, the seasonal average of drift speed is very low in the CBZ of the Baltic Sea. During the whole study season there were only 8 days when the average drift speed in some of the bands exceeded 0.05 m/s, and the maximum daily average was 0.12 m/s. However, the study season included several events when part of the ice pack was drifting at a much higher velocity. These events were local and short, and they only become visible in the hourly time series.

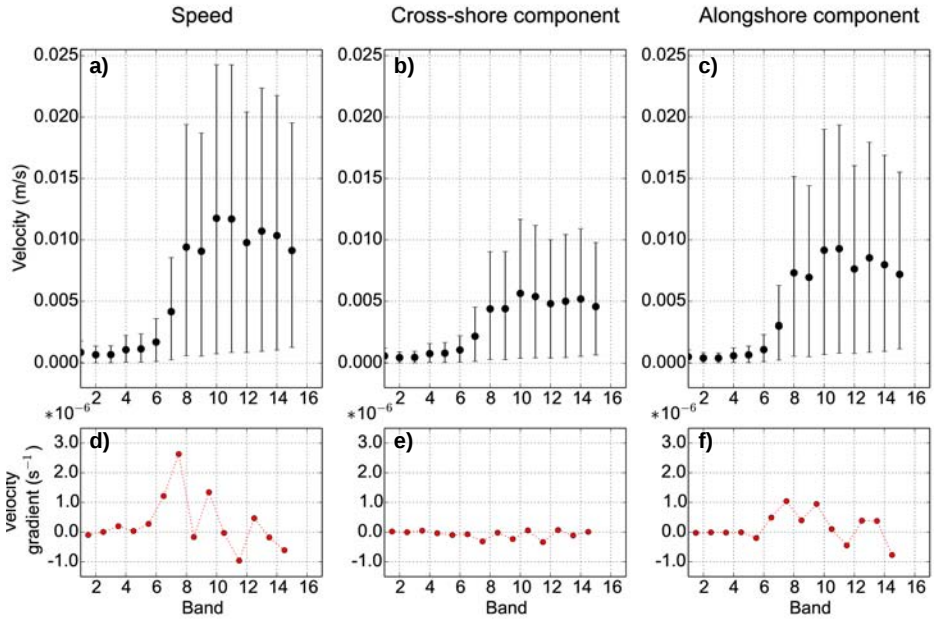

Figure 4.4: The whole study season average of (a) ice drift speed and of the magnitude of (b) cross-shore and (c) alongshore drift component, at different bands. Bars show the range from upper to lower 2.5 percentile of hourly velocities. Seasonal averages of velocity gradients are shown in the lower panel for (d) scalar drift speed and for (e) cross shore and (f) alongshore drift. Velocity gradients are calculated hourly as the difference between mean velocity of neighboring bands divided by the width of the bands (2 km). From Paper III.

4.3 SMALL SCALE SEA ICE DEFORMATION

Previous research on sea ice deformation has mostly been based on drifting buoy and RGPS data, covering length scales from $\sim$ 10 km to 1000 km. With buoys, the deformation rate has been resolved at an hourly time scale, while the time interval of RGPS data is three days. However, sea ice deformation is known to be highly a localized and intermittent process. Now, in studies based on coastal and ship radar images (Papers III and IV) the sea ice deformation rate is resolved over clearly smaller length scales than were previously possible. Thanks to the high temporal resolution of radar images, ice motion can be tracked at sub-pixel scale (Karvonen, 2016) and the smallest length scale covered is 200 m and 50 m for coastal and ship radar data, respectively. For the coastal radar data, the time interval of the deformation rate calculation is 1 h. In Paper IV, the analyses are extended to different time scales,

ranging from 10 min to 24 h. Since the sea ice deformation rate from ship radar images is studied using five different time scales the impact of the time scale on both the deformation rate and the localization of the deformation could be examined.

Previous studies have shown that the sea ice deformation rate exhibits power law scaling with respect to length scale, $\epsilon_{tot} \sim L^{-\beta}$, over the length scales ranging from a few km to 1000 km. In RGPS-based studies in the Arctic, β has been found to be in the range of 0.2 to 0.5 ($\tau = 3$ days), with the greatest values in magnitude in summertime (Marsan et al., 2004) and in regions with a low MYI fraction (Stern and Lindsay, 2009). Hutchings et al. (2012) also reported similar value of β, 0.2, in an Antarctic study based on buoy data ($\tau = 1$ h). The time scale dependence of the deformation rate, $\epsilon_{tot} \sim \tau^{-\alpha}$, and the impact of time scale on the length scale dependence, $\beta = \beta(\tau)$, have not been discussed much, although Rampal et al. (2008) showed the importance of the time scale as well.

Papers III and IV show, that sea ice deformation rate follows the power law scaling $\epsilon_{tot} \sim L^{-\beta}$ even on length scales ranging down to $\sim$ 100 m and time scales ranging down to 10 min. For a 1 h time interval, the obtained power law scaling exponents (0.7 to 0.9) are of greater magnitude than reported in previous studies for the same time scale (Hutchings et al., 2011; Hutchings et al., 2012). β is found to have a similar magnitude both in the Baltic Sea (Paper III) and in the Arctic (Paper IV). The examination of the impact of time scale in Paper IV shows that β depends strongly on the time scale considered (Figure 4.5.d). The relation between τ and β in Figure 4.5.d can be extrapolated to the time scale of RGPS data, τ =3 days. This gives a prediction of $\beta(\tau = 3 \text{ days}) \approx 0.4$. The values in Figure 4.5.d represent thin first and second year ice, and can be compared to the higher end of the β range of RGPS studies. Therefore, the magnitudes of β found for τ of 10 min to 24 h are in good agreement with the results reported for $\tau = 3$ days by Marsan et al. (2004) and Stern and Lindsay (2009).

In Paper III, the coastal radar images of one ice season (2011) in the Baltic Sea are used. Paper IV is based on the ship radar images recorded during the drift of R/V Lance, covering areas from the compact ice pack to the MIZ and lasting from the coldest winter to the onset of summer melt.These unique data sets cover a wide range of conditions. Therefore, it was possible to examine the impact of several factors on sea ice deformation and thereby improve the understanding about how deformation rates vary under different weather conditions in different kinds of ice zones.

Both the coastal radar images recorded in the Baltic and the ship radar images recorded in the Arctic show more intense deformations during warm

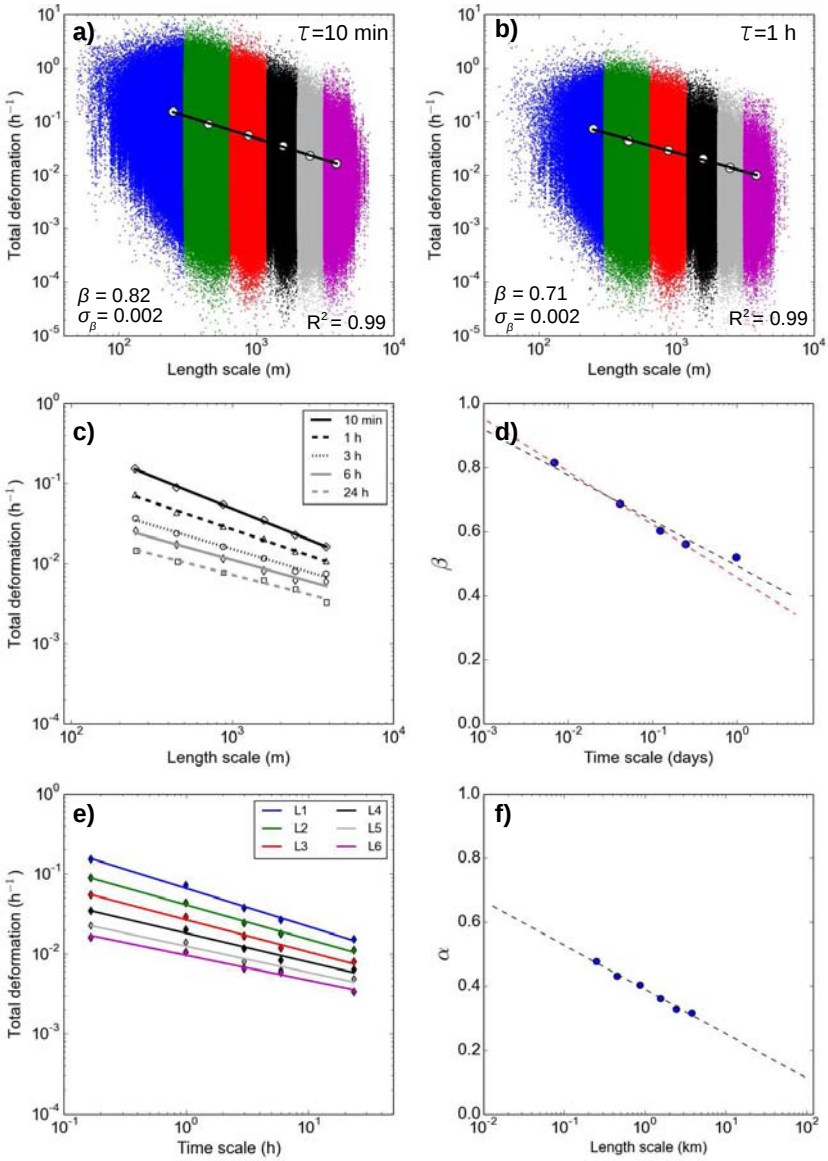

Figure 4.5: The total deformation rate (h^{-1}) of different-sized triangles with (a) a 10 min time interval and (b) a 1 h time interval. Different triangle size groups are presented in different colors, and white circles denote the averages of the groups. Black lines show the least squares fits of the average deformation rates in log-log space and β is obtained as the slope of the fit. The uncertainty of β, σ_β, is estimated as a standard deviation of 10000 bootstrap repetitions. (c) The least square fits for all the time intervals (10 min, 1h, 3h, 6 h and 24 h) and (d) the obtained magnitudes of β. (e) The mean deformation rates of each size group at different time intervals, and the least square fits (colors of the lines correspond to the colors in [a] and [b]). (f) The magnitudes of α (slope of the fitted line in [e]) at different length scales. From Paper IV.

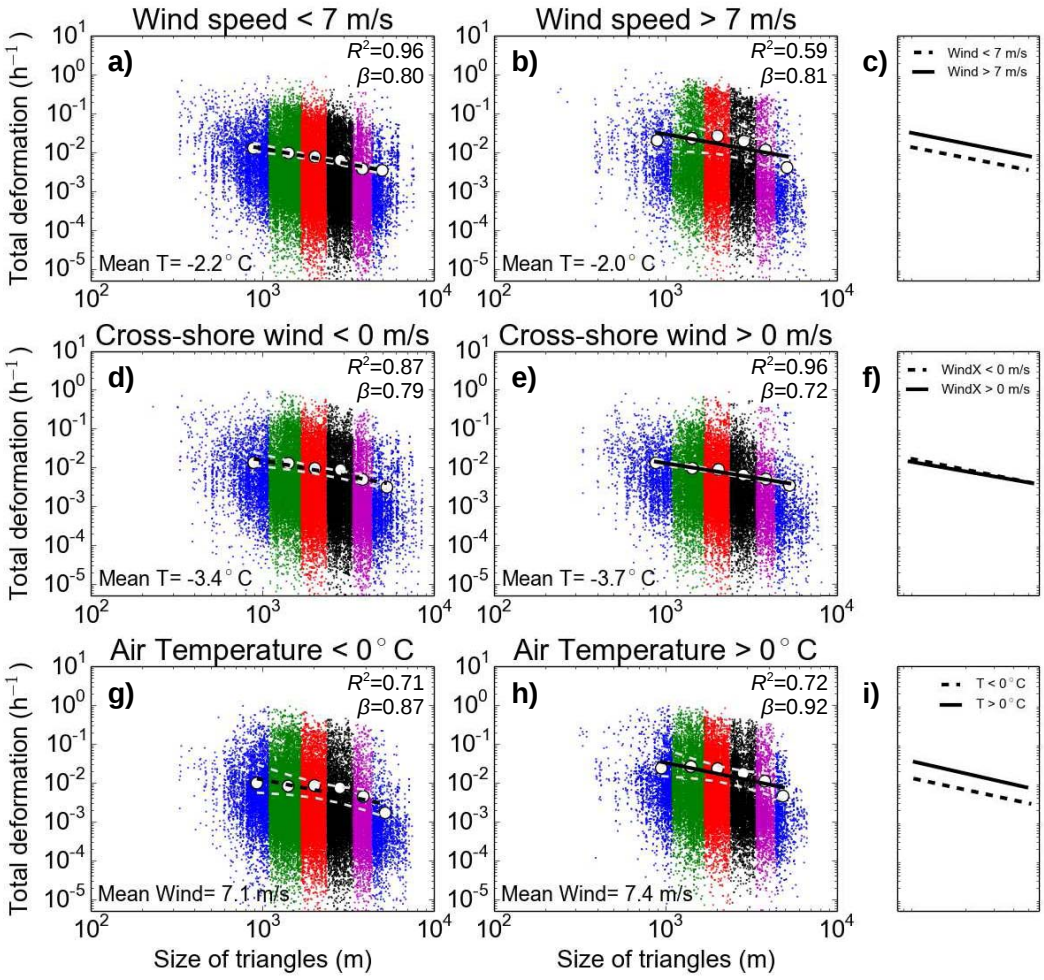

Figure 4.6: Length scale dependency of the sea ice deformation rate under different weather conditions. The impact of weather conditions is shown for three pairs of comparisons: wind speed < 7 m/s (a) vs wind speed > 7 m/s (b), cross-shore wind directed off the coast (d) vs cross-shore wind directed towards the coast (e), and air temperature T< 0°C (g) vs T> 0°C (h). The hourly total deformation rate of different triangle size groups are shown in different colors, and white circles denote the mean deformation rate values of size groups. Black lines (solid and dashed) show the least squares fits of the average deformation rates in log-log space. The 95% confidence interval of the fit is shown with white dashed lines. The fitted lines of each pair are compared in (c), (f) and (i). From Paper III.

periods. As Figure 4.6 shows, the impact of air temperature is seen in all the length scales covered, and it is even on a comparable level with the impact of wind speed in the Baltic Sea. This difference in the deformation rate does not reflect a seasonal time scale variance, but results from the temperature alternation in the time scale of days. In this short time scale, the ice mechanical strength cannot change significantly, and the difference in the deformation rate has to be due to changes in the ice pack strength. This result suggests that the ice pack strength responds to the variation of air temperature clearly faster than previously assumed, and this response is most likely connected to the effectiveness of the healing process.

During the drift of R/V Lance in N-ICE2015, the distance to the ice edge, l, was varying from over 300 km to only a few km. In Paper IV, deformation is studied with respect to l. Deep in the ice pack ($l > 200$ km) high deformation rates were connected to high wind and drift speed, while in the MIZ intense deformations were also observed during calm periods. Also, the length scale dependence changes with respect to l and the greatest magnitude of β was found closest to the ice edge.

Previous studies have concluded that the majority of deformation is brittle in the central Arctic (Marsan et al., 2004; Rampal et al., 2008; Stern and Lindsay, 2009). The failure of sea ice is found to transit from ductile to brittle when the strain rate $\epsilon_{tot} > 10$ day^{-1} (Weiss, 2013). By downscaling the obtained length scale dependence of the compact ice pack, the mean deformation rate was found to exceed this limit, when $L <\sim 10$ m . The MIZ differs clearly from the compact ice pack. Ship radar data showed that also in the MIZ deformation rate exhibits scaling, but with an exponent β of a very high magnitude, indicating that forces are transmitted over shorter distances. This confirms the theory presented by Weiss (2013) proposing that the mechanical behaviour of ice pack changes from elasto-brittle to being more granular-like when moving from the central ice pack to the MIZ. Since the granular medium, the assembly of floes, can still transmit forces, the deformation rates follow the power law scaling (Weiss, 2013).

In Paper IV, the localization of deformation was studied in detail. The results reveal that localization is captured better with smaller time interval. Overall, divergence is a more local process than shear. Also, the total deformation rate, shear and divergence are all less localized at the times of intense deformations. This indicates that the increase in the mean deformation rate results from an increase in the number of cells with significant deformation, rather than from an increase in the deformation rate of the cells with the largest deformations.

Ship radar images recorded during the N-ICE2015 campaign captured

various different types of deformation events and showed the importance of deformation history. During some periods, deformation rates were closely following wind and drift speeds, while some deformation events were induced by swell propagation. Despite the different nature of deformation events, they all started with a similar kind of fracturing in the previously damaged areas. These lines of damage (LDs) can be seen in ship radar images as a lighter color due to higher surface roughness (Figure 4.7). They already formed a dense and complex matrix at the beginning of each ice station. All the deformation events were initialized along these LDs, and, during intense deformation events the matrix of LDs was partly reorganized and new LDs were formed.

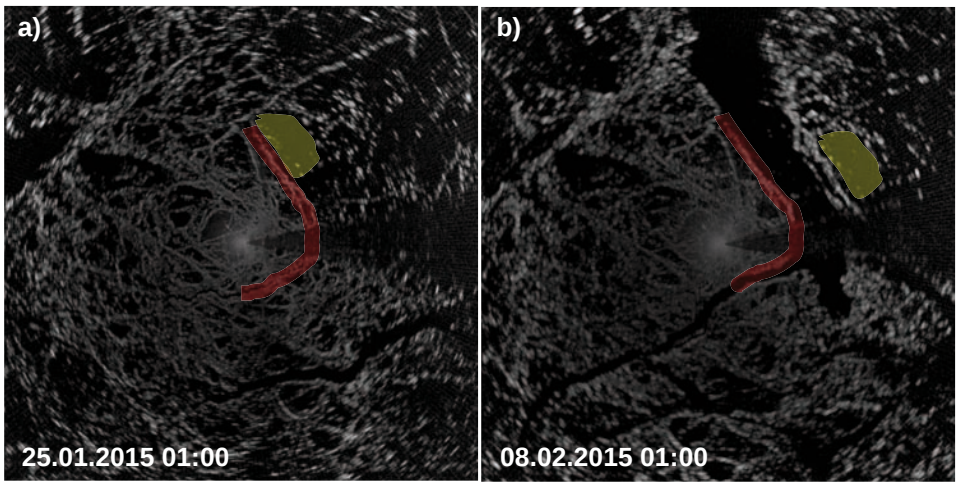

Figure 4.7: Ship radar image on a) 25 January at 01:00 and b) 8 February at 01:00. The red line in (a) and (b) shows the line of damage along which the opening of a wide lead was initiated on 7 February. This line was already visible on 25 January, but it remained inactive until 7 February. For a better view of the lead opening, a level ice area that can be clearly identified both in (a) and (b) is marked a with yellow patch. The images have been cropped and cover an area of approximately 9 km×9 km. From Paper IV.

5 Conclusions

The Arctic has always been an area with large seasonal and interannual variability, which is also seen in the ice cover and results from the interplay between thermodynamics and dynamics. During past decades there have been distinct changes in the atmosphere and ocean that affect both thermodynamic and dynamic forcing of the Arctic sea ice. This has led to an ice cover that responds to forcing in different ways than those known in the past.

Changes in Arctic ice draft distributions, mean and modal draft, and their regional and seasonal variability under different large scale atmospheric circulation modes are determined in Paper I. The results show that the shape of the sea ice draft distribution has changed: the peak of the distribution has generally narrowed and shifted towards thinner ice. A prevalent feature, apparent in all regions in both spring and autumn, is the loss of thick, mostly deformed ice. This had a significant role in the decrease in the mean and modal ice draft. The results also show a decrease in the seasonal variability of the mean ice draft but with strong regional differences. Also, the regional variability of the sea ice draft has decreased, since the thinning has been most pronounced in regions which formerly had the thickest ice cover.

The significant changes in the regional ice draft distributions cannot be directly explained by warming of the atmosphere but changes in the ice drift patterns had an essential impact. The weakening of the Beaufort Gyre and a shift in the strength and east-west position of the Transpolar Drift correspond well with the observed strong thinning in the Beaufort Sea, the Canada Basin and the Eastern Arctic, and also with the unchanged thickness in the Nansen Basin. These changes in the dynamic forcing are connected to large scale atmospheric circulation, which can be described with the AO and DA indices.

These results emphasize the importance of the description of sea ice dynamics in the models. It has been shown that climate models suffer from an inability to reproduce the variation and increase in the ice drift speed and deformation rate, likely due to weak coupling between ice state and kinematics (Rampal et al., 2011). The simple, commonly used parameterization of ice pack strength as a thickness and concentration dependent variable in viscoplastic models is not sufficient to capture seasonal and regional variations.

Consequently, the climate models underestimate the decrease of ice thickness and extent in the Arctic. In the new elasto-brittle rheological framework much more attention is given to the fracturing of ice cover and to the strong length scale dependency of the deformation process.

The response that the ice pack has under dynamic forcing is the result of several factors, including thermodynamic processes. Changes in the Arctic, including the decrease in the ice thickness, extent and age, have led to an increase in the drift speed and deformation rate. On the other hand, these changes in ice kinematics strongly affect the evolution of ice volume and properties of ice cover. There has still been a need for better understanding on highly local and intermittent deformation process, as well as its variability that rises from different types of conditions and regions. Several aspects on these questions are covered in Papers III and IV.

With coastal and ship radar images, the study of the length scale dependency of the sea ice deformation rate is extended to smaller length and time scales than those that were previously possible. The sea ice deformation rate is shown to follow power law scaling, $\epsilon_{tot} \sim L^{-\beta}$, down to the length scale of $L \sim 100$ m and the time scale of τ =10 min. Both the overall deformation rate and its the length scale dependence are found to depend strongly on the time scale considered. This emphasizes that the impact of the time scale has to be taken into account when comparing the deformation rates or the values of β obtained in different studies. For $\tau = 1$ h, the values of β (0.7 to 0.9) are generally of greater magnitude than those reported before for the same time scale. However, the obtained time scale dependence of β predicts a value of 0.4 for the time scale of RGPS-based studies ($\tau = 3$ days), which is in good agreement with Marsan et al. (2004) and Stern and Lindsay (2009). Overall, the results confirm the highly localized and intermittent nature of deformation, and show that the localization is better captured with small time scales and that the intermittency is stronger with small length scales.

Small scale deformation is studied in different types of ice regions (coastal boundary zone, compact Arctic ice pack and marginal ice zone), and under different weather conditions. One of the key findings is the connection between air temperature and the deformation rate: during warm days deformation rates are generally higher than during cold days. The deformation rate is found to respond to changes in air temperature on a time scale of days, which is clearly faster than previously assumed. The ice mechanical strength cannot change significantly in this short time scale, and the difference in the deformation rate is assumed to be due to changes in the ice pack strength. This response is most likely connected to the effectiveness of the healing process.

The results emphasize the importance of the healing process. However, despite the most effective healing occurring during the coldest winter, the lines of damage, LDs, were found to remain as the weak points of the ice cover. Ship radar images from the Arctic ice pack revealed, that all the deformation events were initialized along the LDs. This confirms that the deformation history is an important factor determining how the ice cover responds to dynamic forcing.

Bibliography

Barry, R. G., M. C. Serreze and J. A. Maslanik (1993), The Arctic sea-ice climate system: Observations and modeling, *Rev. Geophys. 31*, 4, 397–422.

Bekryaev, R.V., I.V. Polyakov and V.A. Alexeev (2010), Role of Polar Amplification in Long-Term Surface Air Temperature Variations and Modern Arctic Warming, *J. CLimate*, *23*, 3888–3906.

Belchansky, G., D. Douglas, and N. Platonov (2004a), Duration of the Arctic Sea Ice Melt Season: Regional and Interannual Variability, 1979–2001, *J. Climate, 17*, 67–80.

Belchansky, G. I., D. C. Douglas, I. V. Alpatsky and N. G Platonov (2004b), Spatial and temporal multiyear sea ice distribution in the Arctic: A neural network analysis of SSM/I data, 1988–2001, *J. Geophys. Res.*, *109*, C10017.

Bouillon, S. and P. Rampal (2015a), On producing sea ice deformation data sets from SAR-derived sea ice motion, *Cryosphere*, *9*, 663–673.

Bouillon, S. and P. Rampal (2015b), Presentation of the dynamical core of neXtSIM, a new sea ice model, *Ocean Model.*, *91*, 23-37.

Carmack, E. , I. Polyakov, L. Padman, I. Fer, E. Hunke, J. Hutchings, J. Jackson, D. Kelley, R. Kwok, C. Layton, H. Melling, D. Perovich, O. Persson, B. Ruddick, M.-L. Timmermans, J. Toole, T. Ross, S. Vavrus and P. Winsor (2015), Toward Quantifying the Increasing Role of Oceanic Heat in Sea Ice Loss in the New Arctic, *Bull. Amer. Meteor. Soc., 96*, 12, 2079–2105.

Cavalier, D. J. and C. L.. parkinson (2012), Arctic sea ice variability and trends, 1979–2010. *Cryosphere*, *6*, 881–889.

Coon, M. D. , G. A. Maykut, R. S. Pritchard, D. A. Rothrock and A. S. Thorndike (1974), Modeling the pack ice as elastic-plastic material, *AIDJEX Bulletin, 24*, 1–105.

Eicken, H.(2003), From the microscopic, to the macroscopic, to the regional scale: Growth, microstructure and properties of sea ice, in *Sea ice, An Introduction to its physics, chemistry, biology and geology* (Ed. D.N. Thomas and G.S. Dieckemann), 22–81, Blackwell Science Ltd.

Flato, G., J. Marotzke, B. Abiodun, P. Braconnot, S.C. Chou, W. Collins, P. Cox, F. Driouech, S. Emori, V. Eyring, C. Forest, P. Gleckler, E. Guilyardi, C. Jakob, V. Kattsov, C. Reason and M. Rummukainen (2013), Evaluation of Climate Models. In: C*limate Change 2013: The Physical Science Basis. Contribution of Working Group I to the Fifth Assessment Report of the Intergovernmental Panel on Climate Change* [Stocker, T.F., D. Qin, G.-K. Plattner, M. Tignor, S.K. Allen, J. Boschung, A. Nauels, Y. Xia, V. Bex and P.M. Midgley (eds.)]. Cambridge University Press, Cambridge, United Kingdom and New York, NY, USA, pp. 741–866.

Hibler. W. D. (1979), A dynamic-thermodynamic sea ice model, *J. Physical Oceanography, 32*, 11, 3039–3057.

Holland, M., C. M. Bitz, E. C. Hunke, W. H. Lipscom, J. L. Schramm (2006), Influence of the sea ice thickness distribution on polar climate in CCSM3, *J. Clim., 19,*, 2398–2414.

Hudson, S., L. Cohen and V. Walden (2015), N-ICE2015 surface meteorology v2. Norwegian Polar Institute, https://data.npolar.no/dataset/056a61d1-d089-483a-a256-081de4f3308d.

Hunke E. C. and J. K. Dukowicz (1997), An Elastic-Viscous-Plastic Model for Sea Ice Dynamics, *J. Phys. Oceanography, 27,* 1849–1867.

Hutchings, J. K., A. Roberts, C. A. Geiger and J. Richter-Menge (2010), Spatial and temporal characterisation of sea ice deformation, *Ann. Glaciol.*, *52*, 360—368.

Hutchings, J. K., P. Heil, A. Steer and D. Hibler (2012), Subsynoptic scale spatial variability of sea ice deformation in the western Weddell Sea during early summer, *J. Geophys. Res.*, *117*, *C01002*.

Hutter, N., M. Losch and D. Menemenlis (2016), Scaling properties of Arctic sea ice deformation in high-resolution viscous-plastic sea ice models, 5th FAMOS Workshop, Woods Hole Oceanographic Institution, *poster*, hdl:10013/epic.48927.d001.

Karvonen, J., (2016), Virtual radar ice buoys – a method for measuring fine-scale sea ice drift, *Cryosphere*, *10*, 29–42.

Krishfield, R. A. and D. K. Perovich (2005), Spatial and temporal variability of oceanic heat flux to the Arctic ice pack, *J. Geophys. Res., 110*, C07021.

Kwok, R. (2001), Deformation of the Arctic Ocean sea ice cover between November 1996 and April 1997: A qualitative study, in *Scaling Laws in Ice Mechanics*, edited by J. P. Dempsey and H. H. Shen, pp. 315–322, Kluwer Acad., Norwell, Mass.

Kwok, R. (2006), Contrasts in sea ice deformation and production in theArctic seasonal and perennial ice zones, *J. Geophys. Res.*, *111*, C11S22.

Kwok, R. and D.A. Rothrock (2009), Decline in Arctic sea ice thickness from submarine and ICESat records: 1958-2008, *Geophys. Res. Letters*, *36*, L15501.

Kwok, R. and G. F. Cunningham (2016), Contributions of growth and deformation to monthly variability in sea ice thickness north of the coasts of Greenland and the Canadian Arctic Archipelago, *Geophys. Res. Letters*, *43*, 8097–8105.

Lindsay, R., A. Schweiger (2015), Arctic sea ice thickness loss determined using subsurface, aircraft, and satellite observations, *The Cryospghere*, *9*, 269–283.

Leppäranta, M. (2005), *The Drift of Sea Ice*, Praxis Publishing Ltd Chichester, UK.

Makshtas, A. P. (1998), Thermodynamics of sea ice, In: *Physics of Ice Covered Seas, Vol. 1* (ed. M. Leppäranta), Helsinki University Printing House.

Marsan, D., H. Stern, R. Lindsay and J. Weiss (2004), Dependence and Localization of the Deformation of Arctic Sea Ice, *Phys. Rev. Letters*, *93*, *17*, 178501.

Marsan, D., J. Weiss, J.-P. Metaxian, J. Grangeon, P.-F.Roux and J. Haapala (2011), Low-frequency bursts of horizontally polarized waves in the Arctic sea-ice cover. *J. Glaciol. 57,* 231–237.

National Snow and Ice Data Center, 1998, updated 2006. Submarine upward looking sonar ice draft profile data and statistics. Boulder, Colorado USA: National Snow and Ice Data Center. http://dx.doi.org/10.7265/N54Q7RWK.

Olason, E., and D. Notz (2014), Drivers of variability in Arctic sea-ice drift speed, *J. Geophys. Res. Oceans*, *119*, 5755–5775.

Overland, J., E. Hanna, I. Hanssen-Bauer, S.-J. Kim, J. Walsh, M. Wang, U. S. Bhatt, and R. L. Thoman (2016), Air temperature, in State of the Climate 2015, *Bull. Amer. Meteor. Soc., 97(8)*, S130–S131.

Parkinson, C. L. (2014), Global Sea Ice Coverage from Satellite Data: Annual Cycle and 35-Yr Trends, *J. Climate*, *27*, 9377–9382.

Perovich, D., W. Meier, M. Tschudi, S. Farrell, S. Gerland, and S. Hendricks (2016), Sea ice cover, in State of the Climate 2015, *Bull. Amer. Meteor. Soc., 97(8)*, 134–135.

Rampal, P., J. Weiss, D. Marsan, R. Lindsay and H. Stern (2008), Scaling properties of sea ice deformation from buoy dispersion analysis, *J. Geophys. Res.*, *113*, C03002.

Rampal, P., J. Weiss and D. Marsan (2009), Positive trend in the mean speed and deformation rate of Arctic Sea ice, 1979-2007, *J. Geophys. Res.*, *114*, C05013.

Rampal, P., J. Weiss, C. Dubois and J.-M. Campin (2011), IPCC climate models do not capture Arctic sea ice drift acceleration: Consequences in terms of projected sea ice thinning and decline, *J. Geophys. Res.*, *116*, C00D07.

Renner, A. H. H., S. Gerland, C. Haas, G. Spreen, J. F. Beckers, E. Hansen, M. Nicolaus and H. Goodwin (2014), Evidence of Arctic sea ice thinning from direct observations, *Geophys. Res. Letters*, *41*, 5029-–5036.

Richter-Menge, J. A. and S. Farrell (2013), Arctic sea ice conditions in spring 2009–2013 prior to melt, *Geophys. Res. Letters*, *40*, 5888–5893.

Rigor, I. G., J. M. Wallace and R. Colony (2002), Response of sea ice to the Arctic Oscillation, *J. Climate, 15*, 2648–2663.

Rigor, I. (2002), IABP drifting buoy, pressure, temperature, position, and interpolated ice velocity. Compiled by the Polar Science Center, Applied Physics Laboratory, University of Washington, Seattle, in association with NSIDC. Boulder, CO: National Snow and Ice Data Center. http://dx.doi.org/10.7265/N53X84K7.

Rothrock, D. A., Y. Yu,, and G. A Maykut (1999), Thinning of the Arctic sea-ice cover, *Geophys. Res. Lett., 26*, 3469–3472.

Rothrock, D. A. and J. Zhang (2005), Arctic ocean sea ice volume: What explains its recent depletion?, *J. Geophys. Res., 110*, C01002.

Rothrock, D. A., D. B. Percival and M. Wensnahan (2008), The decline in arctic sea-ice thickness: Separating the spatial, annual and interannual variability in quarter century of submarine data, *J. Geophys. Res.*, *113*, C05003.

Schulson, E. M. (2004), Compressive shear faults within the arctic sea ice: Fracture on scales large and small, *J. Geophys. Res. 109*, C07016.

Schulson, E. M. (2001), Brittle failure of ice, *Engineering Fracture Mechanics*, *68*, 1839–1887.

Spreen, G., R. Kwok. and D. Menemenlis (2011), Trends in Arctic sea ice drift and role of wind forcing: 1992-2009, *Geophys. Res. Letters*, *38*, L19501.

Stern, H. L. and R. W. Lindsay (2009), Spatial scaling of Arctic sea ice deformation, *J. Geophys. Res.*, *114*, C10017.

Stern, H. L. and R. E. Moritz (2002), Sea ice kinematics and surface properties from RADARSAT synthetic aperture radar during the SHEBA drift, *J. Geophys. Res.*, *107*, C10, 8028.

Stroeve, J., T. Markus, L. Boisvert, J. Miller and A. Barrett (2014), Changes in Arctic melt season and implications for sea ice, *Geophys. Res. Lett., 41*, 1216–1225.

Thorndike, A. S., D. A. Rothrock, G. A. Maykut and R. Colony (1975), The thickness distribution of sea ice, *J. Geophys. Res.*, *80*, 33, 2851–2854.

Uppala, S. M., P. W. Kållberg, A. J. Simmons, U. Andrae, V. Da Costa Bechtold, M. Fiorino, J. K. Gibson, J. Haseler, A. Hernandez, G. A. Kelly, X. Li, K. Onogi, S. Saarinen, N. Sokka, R. P. Allan, E. Andersson, K. Arpe, M. A. Balmased, A. C. M. Beljaars, L. Van de Berg, J. Bidlot, N. Bormann, S. Caires, F. Chevallier, A. Dethof, M. Dragosavac, M. Fisher, M. Fuentes, S. Hagemann, E. Hólm, B. J. Hoskins, L. Isaksen, P. A. E. M. Janssen, R. Jenne, A. P. McNally, J.-F. Mahfouf, J.-J. Morcrette, N. A. Rayner, R. W. Saunders, P. Simon, A. Sterl, K. E. Trenberth, A. Untch, D. Vasiljevic, P. Viterbo, and J. Woollen (2005), The ERA-40 re-analysis, *Q. J. R. Meteorol. Soc., 131,* 2961–3012.

Wadhams, P (1998), Sea ice morphology in *Physics of Ice Covered Seas, Vol. 1* (Ed. M. Leppäranta), 231–287, Helsinki University Printing House.

Wadhams, P. and N.R. Davis (2001), Arctic sea-ice morphological characteristics in summer 1996, *Ann. Glaciol., 33,* 165–170.

Wang, J., J. Zhang, E. Watanabe, M. Ikeda, K. Mizobata, J. Walsh, X. Bai and B. Wu (2009), Is the Dipole Anomaly a major driver to record lows in Arctic summer sea ice extent?, *Geophys. Res. Lett., 36*. L05706

Watanabe, E., J. Wang, J. Zhang, A. Sumi and H. Hasumi (2006), Arctic dipole anomaly and its conttribution to sea ice export from the Arctic Ocean in the 20th century, *Geophys. Res. Lett., 33*, L23703.

Weeks, W. F. (2010), *On Sea Ice*, University of Alaska Press, USA.

Weiss, J. (2013), *Drift, Deformation and Fracture of Sea Ice: A Perspective Across Scale*, Springer, Dordrecht, Netherlands.

Weiss, J. and V. Dansereau (2016), Linking scales in sea ice mechanics, *Phil. Trans.R. Soc., A 375*: 20150352.

Wensnahan, M. and D.A. Rothrock, (2005), Sea-ice draft from submarine-based sonar: Establishing a consistent record from analog and digitally recorded data, *Geophys. Res. Lett., 32*, L11502.

Wu, B., J. Wang and J. Walsh (2006), Dipole Anomaly in the winter Arctic atmosphere and its association with sea ice motion, *J. Climate, 19*, 210–225, 2006.

Yu, Y., Maykut, G. A., and Rothrock, D. A., Changes in the thickness distribution of Arctic sea ice between 1958–1970 and 1993–1997, *J. Geophys. Res.*, *109*, C08004.

Zhang, J., D. A. Rothrock and M. Steele (2000), Recent changes in Arctic sea ice: The interplay between ice dynamics and dynamics, *J. Climate, 13*, 3009–3114.

I

Reprtinted, with permission, from
The Cryosphere, 5, 917-929
doi:10.5194/tc-5-917-2011

The Cryosphere, 5, 917–929, 2011
www.the-cryosphere.net/5/917/2011/
doi:10.5194/tc-5-917-2011

The Cryosphere

Variability and changes of Arctic sea ice draft distribution – submarine sonar measurements revisited

A. Oikkonen[1] **and J. Haapala**[2]

[1]University of Helsinki, Department of Physics, P.O. Box 48, 00014 University of Helsinki, Finland
[2]Finnish Meteorological Institute, Helsinki, Finland

Received: 21 December 2010 – Published in The Cryosphere Discuss.: 12 January 2011
Revised: 16 September 2011 – Accepted: 27 September 2011 – Published: 24 October 2011

Abstract. Changes in the mean sea ice thickness and concentration in the Arctic are well known. However, quantitative information about changes in the ice thickness distribution and the composition of the pack ice is lacking. In this paper we determine the ice draft distributions, mean and modal thicknesses, and their regional and seasonal variability in the Arctic for the time period 1975–2000. We compare characteristics of the Arctic pack ice for the years 1975–1987 and 1988–2000. These periods represent different large-scale atmospheric circulation modes and sea ice circulation patterns, most evident in clearly weaker Beaufort Gyre and stronger as well as westward shifted Transpolar Drift during the later period. The comparison of these two periods reveals that the peak of sea ice draft distributions has narrowed and shifted toward thinner ice, with reductions in both mean and modal ice draft. These noticeable changes are attributed to the loss of thick, mostly deformed ice. Springtime, loss of ice volume with draft greater than 5 m exceeds 35 % in all regions except the Nansen Basin, with as much as 45 % or more at the North Pole and in the Eastern Arctic. Autumn volume reduction, mostly of deformed ice, exceeds 40 % in the Canada Basin only, but is above 30 % also in the Beaufort and Chukchi Seas. During the later period, the volume of ice category consisting thin, mostly level first-year ice, is clearly larger than during the former period, especially in the spring. In the Beaufort Sea region, changes in the composition of ice cover have resulted in a shift of modal draft from level multiyear ice draft range to values of level first-year ice. The regional and seasonal variability of sea ice draft has decreased, since the thinning has been most pronounced in regions with the thickest pack ice (the Western Arctic), and during the spring (0.6–0.8 m per decade).

Correspondence to: A. Oikkonen
(annu.oikkonen@helsinki.fi)

1 Introduction

The Arctic Ocean exhibits large climate variations on a time scale of decades. This variability is largely driven by the large-scale atmospheric circulation, which affects meridional heat and moisture transport from the mid-latitudes to the Arctic region and, as a consequence, alters the surface heat balance of the Arctic Ocean. Another, perhaps more significant, effect is that sea ice and ocean surface circulation patterns are modified in accordance with the atmospheric changes.

The state of the atmospheric circulation is commonly described by the empirical orthogonal function (EOF) of the surface air pressure field. The first EOF is called the Arctic Oscillation (AO) or Northern Annular Mode (Thompson and Wallace, 1998). This mode is related to the magnitude of the zonal circulation (Rigor et al., 2002; Zhang et al., 2000). The second mode is called the Dipole Anomaly (DA) (Wu et al., 2006; Watanabe et al., 2006). The DA is a measure of the strength of an atmospheric meridional circulation from the Pacific sector to the North Atlantic. Wu et al. (2006) state that the influence of the DA on winter sea ice motion is greater than that of the AO, especially in the central Arctic basin, and north of Fram Strait. During its positive phase the DA has a particularly strong effect on the ice conditions, since in addition to the strengthening of the transpolar drift, and export of sea ice from the Arctic Ocean through Fram Strait, it also enhances an inflow of Pacific water into the Arctic.

While many papers have focused on sea ice changes and the relationship between the atmospheric circulation and sea ice conditions (e.g. Hilmer and Lemke, 2000; Zhang et al., 2000; Holloway and Sou, 2002; Makshtas et al., 2003; Bitz and Roe, 2004; Rothrock and Zhang, 2005; Kwok, 2009), analyses have been mostly limited to considering mean sea ice thickness, concentration, or drift. However, the state of the pack ice is best characterized by the sea ice thickness

distribution $g(h)$, defined as follows

$$\int_{h_1}^{h_2} g(h)dh = \frac{1}{R}A(h_1,h_2), \quad (1)$$

where R denotes the total area of the region, and $A(h_1,h_2)$ is the area within region R covered by ice with thickness h in the range $h_1 \leq h < h_2$ (Thorndike et al., 1975).

Pack ice can be understood as being composed of three main ice types: level first-year ice (FYI), level multi-year ice (MYI), and deformed ice. In addition, the pack ice may contain areas of open water. Ice types cannot be separated unambiguously within an observed ice thickness distribution, since their thicknesses overlap. However, certain ice thickness categories are dominated by a particular ice type. FYI has undergone at most one growth/melt season, and on the basis of the model of Maykut and Untersteiner (1971) it can be assumed to reach a maximum of about 2 m at the end of the growth season, and about 1 m in the autumn after the summer melt, providing upper bounds on level FYI thickness at the time of annual maximum and minimum thickness. In the sea ice thickness distribution $g(h)$, ice thicker than level FYI consists of level MYI and deformed ice. The thickness of level MYI approaches the equilibrium thickness, which can be set as the upper limit for level MYI, i.e. 3–5 m depending on climatological conditions. Ice thicker than the equilibrium thickness is mostly deformed.

Ice thickness distributions in perennial ice zone (PIZ) and seasonal ice zone (SIZ) have distinct characteristics that vary seasonally. In the spring, $g(h)$ typically exhibits a pronounced peak corresponding to level FYI in the SIZ and level MYI in the PIZ. In the autumn, the PIZ thickness distribution can be bi-modal, if a second maximum is formed in open water or very thin ice. In the autumn SIZ, $g(h)$ is dominated by very thin FYI and open water, with low abundance of thicker ice types.

The evolution of $g(h)$ depends on the thermodynamic and dynamic forcing. Changes in those factors have different impacts on the shape of $g(h)$, and in some situations an evaluation of changes in $g(h)$ reveals whether the observed changes in the pack ice are due to predominantly thermodynamic or dynamic processes.

Ice growth and melt change the position of the modal peaks of level FYI and MYI. Pure thermodynamic forcing (in the case of landfast ice) would result in a single-peak distribution. Kurtosis, i.e. an indication of the peakedness of $g(h)$, is a measure of the relative contribution of dynamic processes (opening, redistribution, and advection of pack ice), which broaden the single-peak distribution. On a regional scale, changes in the circulation and influx of sea ice could result in large changes in $g(h)$. Shifts in differential ice drift have an effect on both ends of $g(h)$. Changes in lead opening are reflected in the fraction of open water and thin ice, and changes in ridging are seen in the tail of $g(h)$. However, sea ice thermodynamic and dynamic processes are strongly coupled, and in some situations it is difficult to separate these effects. For example, the longer the ice circulates in the Arctic, the more time it has to thicken both thermodynamically and through deformation. Thus, the change in the drift pattern and average travel time can cause significant changes both in the modal thickness and in the fraction of ridged ice.

In this study we utilize data from submarine cruises of the U.S Navy and the Royal Navy from the years 1975–2000. The data are archived and publicly available at US National Snow and Ice Data Center. The 26 years covered by the available data are divided into two periods, 1975–1987 and 1988–2000. The objective of the present paper is to examine changes of the sea ice draft distribution in detail. The analysis is conducted for spring and autumn, i.e. for the periods of annual maximum and minimum ice thickness. Particular attention is given to the analysis of changes in the composition of pack ice, and to the impact of thermodynamics and dynamics on the evolution of the Arctic sea ice cover. Changes in the ice dynamics are studied based on the IABP (International Arctic Buoy Program) ice drift observations.

The submarine sonar data have been examined in several earlier studies. However, many of these were limited to consider mean sea ice thickness or draft, e.g. Rothrock et al. (1999), Rothrock and Zhang (2005), Rothrock et al. (2008) and Kwok and Rothrock (2009). Only few studies (Wadhams and Davis, 2001; Yu et al., 2004) have presented the ice thickness distributions. In this paper we show ice thickness distributions for six regions, two seasons and two 13-year periods. Our results are based on the data from 31 submarine cruises, which is much more than used in previous studies; the number of cruises analyzed in the work of Wadhams and Davis (2001) is only 2, and in the work of Yu et al. (2004) the corresponding number is 7. In Wadhams and Davis (2001) analyses are regionally limited, covering the Greenland Sea and the Eurasian Basin. While the work of Tucker et al. (2001) is also based on submarine sonar measurements, they do not show changes in ice draft distributions other than relative fraction of four coarse ice draft classes. Our analysis extends prior work and provides a more detailed, quantitative view of changes in the Arctic sea ice thickness distribution.

2 Data and analysis

The US Navy and Royal Navy upward-looking sonar data set includes sea ice draft measurements from 37 cruises accomplished during the years 1975–2000, covering over 120 000 km of track in total. Data are archived for public use at the US National Snow and Ice Data Center (NSIDC). Data has been recorded partly in analog, and partly in digital format. The error in the comparability of analog data with digitally recorded data is ± 6 cm (Wensnahan and Rothrock, 2005), which is very small compared with draft values of typically several meters, and in this study data collected in both formats have been used. The standard deviation of submarine sonar measurements is 25 cm, and the draft

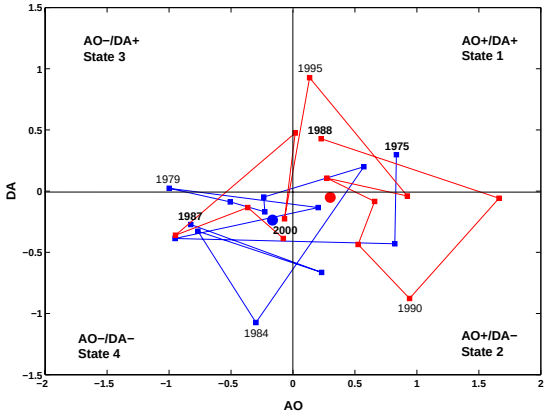

Fig. 1. Annual Arctic Oscillation index (AO) and Dipole Anomaly index (DA). Years 1975–1987 are marked with blue and years 1988–2000 with red color. Circles denote the mean values of these 13-year periods.

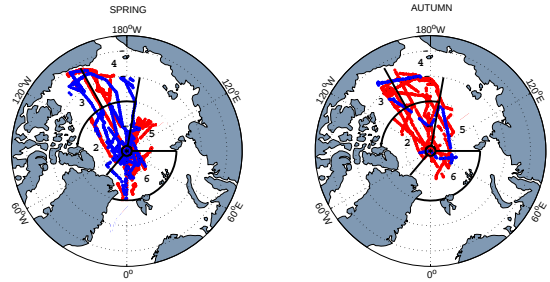

Fig. 2. Cruise tracks of utilized submarine data from periods 1975–1987 (blue) and 1988–2000 (red) in Spring (on the left) and Autumn (on the right). The whole study area is divided into 6 regions: 1. North Pole, 2. Canada Basin, 3. Beaufort Sea, 4. Chukchi Sea, 5. Eastern Arctic and 6. Nansen Basin.

Table 1. Length of the submarine track in kilometers.

	Spring		Autumn	
Region	1975–1987	1988–2000	1975–1987	1988–2000
1 North Pole	1748	1836	86	1141
2 Canada Basin	5969	5411	296	6991
3 Beaufort Sea	3887	2355	368	4342
4 Chukchi Sea	1617	7128	316	7463
5 Eastern Arctic	376	5420	346	4682
6 Nansen Basin	4475	8593	306	2934

measurements are biased by +29 cm compared with the true draft (Rothrock and Wensnahan, 2007). Very recent work of Rodrigues (2011) states that error of submarine based draft measurements depend on the measuring depth, beam width of the sonar and the roughness of ice bottom surface, and may be higher than reported in earlier studies. Unfortunately public archive in NSIDC does not include all the information needed (depth of a submarine, beam width) for data processing suggested by Rodrigues (2011). On the other hand, our results are now comparable with earlier works (e.g. Rothrock et al., 1999; Tucker et al., 2001; Yu et al., 2004). This study focuses on spring (April and May) and autumn (September and October), providing the highest data density, and the possibility to track annual maximum and minimum thicknesses (Rothrock et al., 1999). From here on, Spring refers to April and May, and Autumn refers to September and October. The cruises were equally distributed within each season during the whole study period, and no temporal adjustment is made for the date of the measurements.

The 26 years covered by the available data are divided into two periods, 1975–1987 and 1988–2000. Although the division is somewhat arbitrary, it coincides with changes in climatologic and oceanographic conditions in the Arctic, e.g. a decrease of sea level pressure (SLP) in the central Arctic at the end of the 1980s (Walsh et al., 1996), and a change in the AO index from a mostly negative to a strongly positive phase in 1988 (Rigor et al., 2002). As Wang et al. (2009) showed, the major atmospheric circulation patterns of the Arctic are well described by the modes of AO and DA. Figure 1 depicts how the individual years of the two periods examined in this paper are placed in an AO/DA space. It is clear that the period 1975–1987 was dominated by negative AO and DA years: average AO and DA values were –0.17 and –0.24, respectively. The later period also includes negative AO and DA years, between 1996–2000, but positive AO and DA years prevailed at the beginning of the period.

In total, the former half (1975–1987) includes data from 12 cruises, of which 9 were accomplished in Spring and 3 in Autumn, while the later half (1988–2000) includes data from 11 Spring cruises and 8 Autumn cruises. To examine potential changes in regional variability, the covered area is divided into six regions (Fig. 2). As Fig. 2 shows, Spring cruise tracks provide better and more even coverage of all regions during both periods. In Autumn, especially in Chukchi Sea (region 4), data from the former period is collected in lower latitudes than data from latter period.

Analysis is based on profile data that includes all measurements at an interval of about one meter. Regional mean drafts and draft distributions are calculated from all the point measurements recorded within one region during the period and season concerned. In total the number of recordings utilized is over 78 000 000, corresponding to roughly 78 000 km of submarine track. The length of analyzed submarine track is listed in Table 1.

All analyses are based on and reported in terms of draft instead of thickness, because an accurate conversion to thickness would require knowledge of sea ice density, as well as

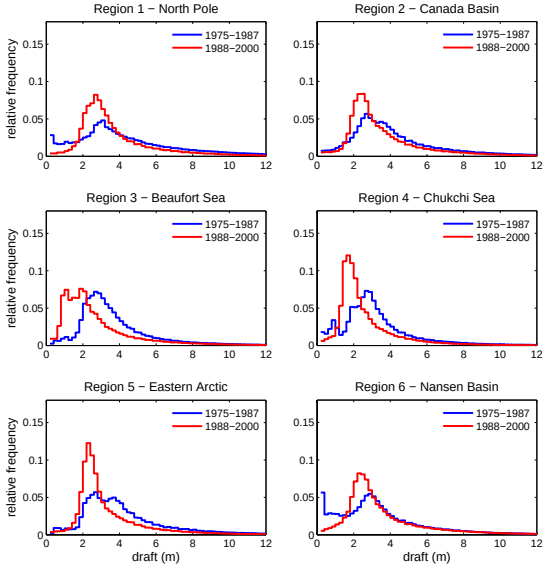

Fig. 3. Regional Spring draft distributions during periods 1975–1987 (blue line) and 1988–2000 (red line). Bin width 0.2 m.

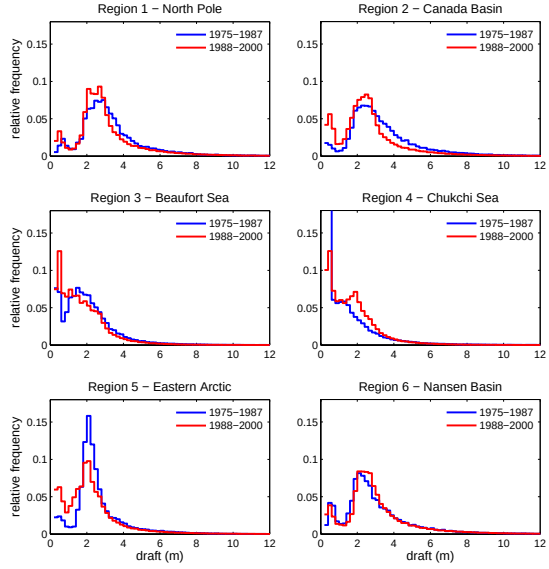

Fig. 4. Regional Autumn draft distributions during periods 1975–1987 (blue line) and 1988–2000 (red line). Bin width 0.2 m.

the thickness and the density of the snow cover. Mean draft values also include recordings of open water. The variability and changes of the Arctic sea ice cover are also examined through the evolution of three ice categories, classified by draft (D). Category 1 includes all the ice with $D < 2$ m in Spring and $D < 1$ m in Autumn. Hence, this category consists mainly of level FYI. Category 2 is dominated by level MYI, and the upper limit is set at $D = 5$ m. Category 3 consists of ice with draft $D > 5$ m, and this category is dominated by deformed ice (Wadhams and Davis, 2001).

3 Results

3.1 Ice draft distribution

Probability density functions of ice draft, i.e. draft distributions $g(D)$ are calculated with an interval of 20 cm for each region, for Spring and Autumn in 1975–1987 and 1988–2000 (Figs. 3 and 4). Corresponding modal drafts are listed in Table 2. All regional Spring draft distributions from the first period (Fig. 3, blue line) have a uniform shape with one wide peak at draft 2–3 m, which falls into ice category 2, and into the typical range of level MYI. Regional differences are most pronounced in the fraction of open water and thin ice, $D < 0.5$ m. In region 6 the fraction of ice in the thinnest bin is so high that it results in a second maximum. Compared to the first period, Spring draft distributions from 1988–2000 (Fig. 3, red line) have much higher and narrower peaks, located in thinner ice, $D = 1.5 - -2.5$ m, and their regional variability is larger. In regions 1, 2, 5 and 6, i.e. in the central and eastern Arctic, Spring draft distributions show clear narrowing and heightening of the peak, due to a noticeable increase of ice with a draft of 1–3 m and a decrease of other thicknesses. In regions 1 and 2 modal draft in Spring is in MYI-dominated category 2 during both periods, despite a modest thinning (–0.4 m and –0.2 m, respectively, Table 2). In region 5 Spring modal draft has decreased from 2.5 m to 2.1 m, but the shape of the peak has changed noticeably to a narrower and higher form. This is caused by an increase of ice with a draft of 1–3 m, and a clear decrease of ice with $D > 3$ m. In the western Arctic, in regions 3 and 4, the modal draft in Spring has decreased from 2.5 m to 1.7 m, and from 2.5 m to 1.5 m, respectively. In these regions the peak has shifted from ice category 2 to category 1. Although ice category 1 is assumed to be dominated by FYI, the increase in this category may be partly also due to the thinning of MYI cover. Eicken et al. (2001) observed in Chukchi Sea during the spring 1998 that the dominant ice type was level second year ice with the modal thickness less than 2 m.

Autumn draft distributions from 1975–1987 (Fig. 4, blue line) differ clearly from Spring cases. The shape of Autumn draft distributions has a large regional variability. However, all the distributions, except region 4, have a local minimum around $D = 0.5$–1 m, at the boundary between level FYI and level MYI. Draft distributions from 1988–2000 (Fig. 4, red line) show a more pronounced bi-modal structure in the central Arctic (regions 1 and 2) as the concentration of thin FYI has increased, and the concentration of thick, mostly

Table 2. Regional Spring and Autumn mean and modal draft in 1975–1987 and 1988–2000. The difference between regional mean drafts of these two periods is normalized over a decade.

Region	Season	Mean/modal draft (m) 1975–1987	1988–2000	Change (m/decade)
1 North Pole	Spring	4.4/2.9	3.6/2.5	–0.6/–0.3
	Autumn	3.1/2.7	2.8/2.5	–0.2/–0.2
2 Canada Basin	Spring	4.2/2.5	3.4/2.3	–0.6/–0.2
	Autumn	3.1/2.1	2.4/2.3	–0.6/+0.2
3 Beaufort Sea	Spring	3.5/2.5	2.5/1.7	–0.8/–0.6
	Autumn	1.7/1.3	1.5/0.3	–0.2/–0.8
4 Chukchi Sea	Spring	3.1/2.5	2.4/1.5	–0.5/–0.8
	Autumn	1.2/0.1	1.4/0.3	+0.2/+0.2
5 Eastern Arctic	Spring	4.5/2.5	3.1/2.1	–1.1/–0.3
	Autumn	2.3/1.9	1.9/1.9	–0.3/0
6 Nansen Basin	Spring	3.3/0.1	3.4/2.1	+0.1/+1.5
	Autumn	2.7/1.9	2.8/1.9	+0.0/0

deformed ice has decreased. The concentration of very thin ice ($D < 0.4$ m) has strongly increased in central Arctic: roughly doubled in region 1 and tripled in region 2, resulting in a clear second maximum at $D = 0.3$ m. Also ice with $D = 1.5 - 2.5$ m (mostly thin MYI) has increased in these two regions, while thicker ice has decreased. In Autumn the modal draft has remained unchanged in region 5. However, the shape of the draft distribution has changed from one high peak to a clearly bi-modal structure, as the fraction of open water and thin ice with $D < 0.4$ m has more than doubled, and the fraction of ice around $D = 2$ m (mainly level MYI) has decreased by nearly 40 %. In region 6, in Autumn, the draft distributions from periods 1975–1987 and 1988–2000 are very similar. In general, changes in the modal draft are smaller in Autumn than in Spring, and region 3 is the only region showing a strong decrease (–1.0 m) while in regions 2 and 4 the modal draft has increased by 0.2 m (Table 2). In Chukchi Sea this increase may be at least partly due to difference in sampling latitude, as the data from the earlier period derives from only the southern part of the region (Fig. 2).

Draft distributions can be divided into two groups with the characteristics of the PIZ and SIZ. In the PIZ the Autumn draft distribution typically has a bi-modal shape, with a modal draft in MYI and a second maximum in very thin ice or open water. As Fig. 4 shows, this is the case in regions 1, 2, 5 and 6 during both periods, and in region 3 during the first period. In these regions the modal draft is around 2–3 m, the second maximum is in very thin ice ($D = 0.3$ m), and there is a local minimum between them at $D = 0.7$–0.9 m. In the SIZ the Autumn draft distribution is dominated by open water and thin FYI, which is the case in region 4 during both periods and in region 3 during the later period. In these regions the draft distributions do not show any distinguishable minimum between FYI and MYI, since the distribution is high and fairly even for drafts 0.5–2 m, and the concentration of ice thicker than $D = 2$ m decreases rapidly with increasing draft.

In region 3, the characteristics of the ice cover have clearly changed. The height and the width of the peak in the Spring draft distribution have remained the same, but the location has shifted to much thinner ice, from ice category 2 to category 1. As mentioned earlier, this strong increase in ice category 1 may be at least partly due to the thinning of level MYI cover. In Autumn, the change is most pronounced in thin ice ($D < 0.6$ m), which has increased so much that a local minimum around 0.5 m, present in 1975–1987, has disappeared. During the first period the shape of the Autumn draft distribution in region 3 has the characteristics of the PIZ, in contrast to the later period, when the shape of the Autumn draft distribution is very representative of the SIZ.

The regional Spring and Autumn mean drafts for the periods 1975–1987 and 1988–2000 are presented in Table 2. Table 2 also shows the difference between regional mean drafts for these two periods normalized over a decade. In Spring, in regions 3 and 5 the mean draft has noticeably decreased, by about 1 m. In regions 1, 2 and 4 the Spring mean draft also has clearly decreased, by 0.7 m or more. In Autumn, changes in general are more modest, and region 2 is the only region where the decline in the Autumn mean draft exceeds the thinning in Spring. In regions 1, 3 and 5, the decrease of the Autumn mean draft is only about 30 % of the decrease observed in Spring. In region 4 the Autumn mean draft has increased by 0.2 m. In region 6 the mean draft has remained nearly unchanged in both Spring and Autumn, with a slight increase of about 0.1 m. However, in view of the accuracy of the draft measurements, changes with a magnitude of 0.1 m cannot be regarded as significant.

Table 3. Difference in the mean ice draft and in the volume of three ice categories between the periods 1975–1987 and 1988–2000. Ice category 1 consists of ice with draft < 2 m in Spring and < 1 m in Autumn, ice category 2 includes draft range 2–5 m in Spring and 1–5 m in Autumn, and all ice with draft > 5 m falls into ice category 3.

Region	Season	Mean draft	category 1	category 2	category 3
1 North Pole	Spring	–18.2 %	+17.4 %	+27.5 %	–46.4 %
	Autumn	–9.9 %	+8.0 %	–9.0 %	–12.8 %
2 Canada Basin	Spring	–16.9 %	+68.0 %	–3.5 %	–35.6 %
	Autumn	–24.1 %	+1950.3 %	–17.6 %	–43.5 %
3 Beaufort Sea	Spring	–29.3 %	+176.4 %	–48.8 %	–35.7 %
	Autumn	–16.8 %	+44.9 %	–19.5 %	–35.4 %
4 Chukchi Sea	Spring	–22.6 %	+134.3 %	–40.1 %	–44.1 %
	Autumn	+19.0 %	–9.8 %	+43.6 %	–32.8%
5 Eastern Arctic	Spring	–30.9 %	+109 %	–27.9 %	–47.1 %
	Autumn	–16.6 %	+209.8 %	–20.5 %	–16.6 %
6 Nansen Basin	Spring	+3.3 %	+21.6 %	+10.3 %	–7.2 %
	Autumn	+2.1 %	–17.3 %	+3.5 %	+0.3 %

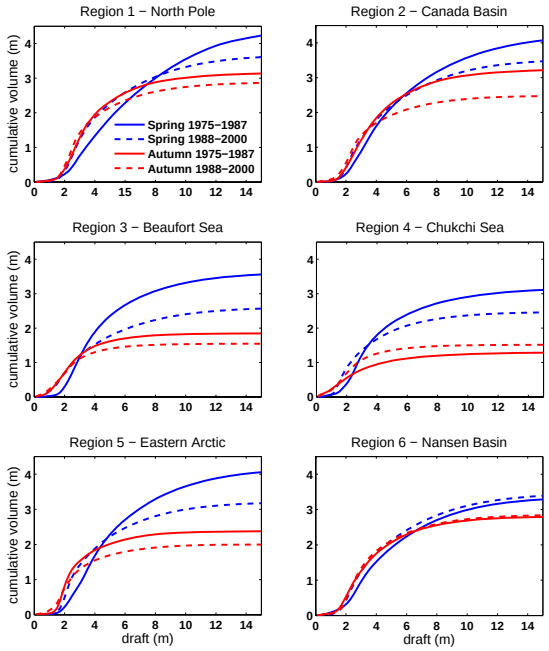

Fig. 5. Regional cumulative ice volume distribution in Spring and Autumn during the periods 1975–1987 and 1988–2000. Bin width 0.2 m. Integration of ice volume distribution results in mean ice draft, which corresponds to ice volume over unit area.

3.2 Ice volume distribution and composition of ice volume

The probability density function of ice volume is calculated after Yu et al. (2004), but as a function of draft D, $V(D) = g(D)D$. This function is dimensionless and describes the fraction of total volume of ice with draft D. It integrates to the mean draft (Yu et al., 2004)

$$\overline{D} = \int_0^\infty V(D) dD, \tag{2}$$

and corresponds to a volume over a unit area. Because they are defined using draft instead of thickness, the volumes presented here correspond to the submerged portion of the total ice volume. As Eq. 2 shows, the total ice volume per unit area equals the mean draft, but the benefit of this approach as compared with calculating the mean draft by directly averaging single measurements is that it makes it possible to determine the composition of the total ice volume.

Cumulative ice volume distributions from the periods 1975–1987 and 1988–2000 in all the regions are shown in Fig. 5 for Spring and Autumn. The total ice volume per unit area, i.e. mean ice draft, is determined as the sum of the volumes in each bin, i.e. the cumulative volume in the thickest ice bin. Percentage changes in the mean ice draft in Spring and Autumn are listed in Table 3.

Region 6 is the only area where the mean ice draft has remained nearly unchanged in both seasons; it even shows a very slight increase. In all other regions the mean Spring ice draft has decreased by over 15 %, resulting from the loss of thick ice. The reduction of the mean Spring ice draft is largest in region 3, where the decline is nearly 30 % due to a considerable reduction of ice with $D > 3$ m. At the same time, the volume of level FYI ($D < 2$ m) is nearly twice as

large during the later period. In region 4, the evolution of the mean ice draft in Spring is very similar to region 3, but in the central Arctic (regions 1 and 2) the decline is more modest (–18 % and –17 %, respectively) and has occurred due to the loss of thicker, mostly deformed ice (with $D > 8$ m and $D > 5$ m, respectively).

In Autumn the change in the mean ice draft is largest in region 2 (–24 %), which is the only region where the decline is greater in Autumn than in Spring. Evolution in Autumn is exceptional in region 4, where the mean ice draft has increased by 19 %, and the increase of ice volume is pronounced in all ice categories with $D > 1$ m. However, this may be a result of the earlier data having been collected further south than the later data.

In addition to these changes in mean draft, the composition of the ice volume has also changed, even in region 6. Figure 6 illustrates the composition of the regional Spring and Autumn ice volumes of the three ice categories during both 13-year periods. The percentage change in the volume of the ice categories is listed in Table 3.

As Table 3 shows, the volume of ice category 1 has increased considerably in most of the regions and in both seasons. The only exceptions with decreasing volume of the thinnest ice category are regions 4 and 6 in autumn. Despite the clear increase in volume of ice category 1, this thinnest ice category comprises less than 10 % of the total ice volume in the PIZ (regions 1, 2, 5 and 6 during both periods, region 3 during former period). The change from perennial to seasonal ice in region 3 is evident in the remarkable increase of ice volume in category 1 (+176 % in Spring and +45 % in Autumn). Because of this large increase, during the later period about 25 % of the total Spring ice volume consists of ice of the thinnest category, while during the former period the corresponding fraction is only 7 %.

The volume of MYI-dominated category 2 has generally decreased. The reduction has been strongest in region 3 (–49 % in Spring and –20 % in Autumn) and in region 5 (–28 % and –21 %). In these regions the volume of ice in categories 1 and 2 (roughly representing the volume of level ice) has decreased in both seasons despite the increasing volume of the thinnest ice type (mainly thin FYI). In Spring a similar evolution, though of smaller magnitude, can be seen also in region 4. In region 1 the volume of ice in category 2 in Spring has increased by more than 27 %. Even though ice of category 2 can be assumed to be dominated by level MYI, this increase does not necessarily mean an increase in level MYI volume. It can, and most likely does, reflect a decrease in the thickness of deformed ice, with a greater proportion of thin deformed ice falling into ice category 2 ($D < 5$ m). In Autumn region 4 is the only region where a clear increase in the volume of ice in category 2 is observed. In region 6 changes are small, but in all other regions the volume of ice in category 2 in Autumn has decreased by about 10–20 %.

Ice in category 3 consists mostly of thick deformed ice. Evolution of this ice category is regionally and seasonally

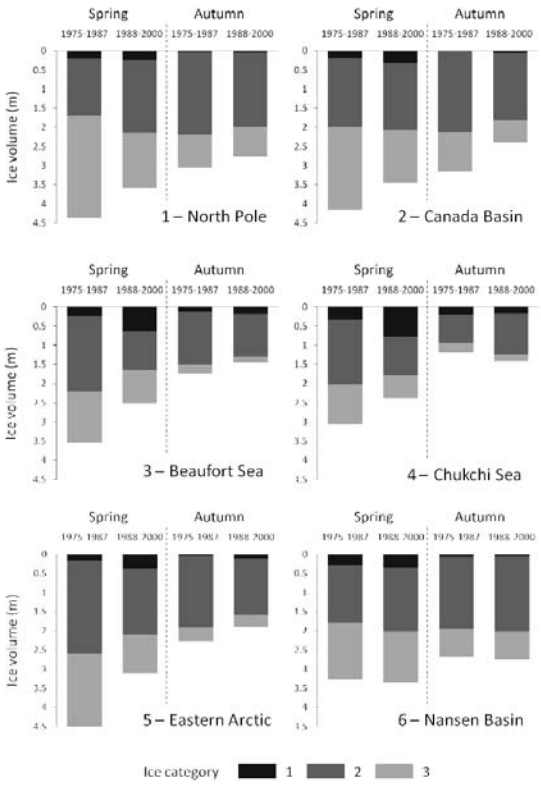

Fig. 6. Regional mean sea ice draft and its composition. Ice category 1 consists of ice with draft < 2 m in Spring and < 1 m in Autumn, ice category 2 includes draft range 2–5 m in Spring and 1–5 m in Autumn, and all ice with draft > 5 m falls into ice category 3.

the most uniform of all the observed changes. As draft distributions show, the concentration of thick deformed ice has decreased in all regions both in Spring and in Autumn. Since the thickest ice types have a great weight in the total ice volume, the decrease in the concentration of deformed ice is largely responsible for the decline in the mean ice draft that is observed in almost all the regions. In general, the volume of the thickest ice category has decreased more strongly in Spring than in Autumn, and only in region 2 we observe a greater decrease in Autumn than in Spring. In Spring the loss of category 3 ice volume exceeds 35 % in all regions except region 6, and the reduction reaches over 45 % in regions 1 and 5. In Autumn the volume of thick, mostly deformed ice (category 3) has decreased by more than 40 % in region 2 only, but the reduction is more than 30 % also in regions 3 and 4. In Region 6 changes have been considerably smaller than in all other regions, –7 % in Spring and no change in Autumn.

Figure 6 as well as Fig. 5 confirm that the loss of thick, deformed ice is largely responsible for the decrease in mean ice draft. This is most evident during Spring in regions 1 and 2, where the volume of ice categories 1 and 2 (roughly corresponding to level ice) has even increased, and thus the decline in the mean ice draft of over 17 % has occurred purely due to the loss in the thickest ice category dominated by deformed ice. However, if the loss of deformed ice volume is not due to a decrease in the number of ice ridges only, but also due to a decreasing ridge thickness, then more deformed ice may fall into ice category 2.

4 Discussion

4.1 Thinning rate

Regional mean drafts (Table 2) have decreased considerably in most regions, but with large regional and seasonal differences. Thinning of the Arctic sea ice cover has been reported in several studies (e.g. Wadhams, 1990; Rothrock et al., 1999; Wadhams and Davis, 2000; Tucker et al., 2001; Rothrock et al., 2003; Yu et al., 2004; Kwok and Rothrock, 2009). These studies are based on submarine sonar measurements, but from different years and seasons as well as from different areas, so that comparison of results is not straightforward. In all previous studies, as well as in our work, the observed thinning follows a similar regional pattern, with the largest changes in the central and western Arctic. These regions have been included in most of the past studies and exhibit the highest data densities. In other regions, results are more variable between studies and based on more sparse data.

Rothrock et al. (1999) and Yu et al. (2004) compared Autumn mean drafts from four historical submarine cruises (from late 1950s to 1970s) with three more recent voyages (1993–1997). They both reported pronounced ice thinning in the central and western Arctic, i.e. in the North Pole region, the Canada Basin and the Beaufort Sea, with a rate of approximately –0.4 m per decade. This is about double the Autumn thinning rate in the North Pole region and the Beaufort Sea (regions 1 and 3) that we present in Table 2, but slightly less than that observed in the Canada Basin (region 2). Rothrock et al. (1999) reported strong thinning also in the Chukchi Sea, while Yu et al. (2004) did not find any significant change in this region. Both of these findings differ from the changes found in the present study, since for the period 1975–2000 the Chukchi Sea (region 4) shows an increase in Autumn mean draft with a rate of +0.2 m per decade. In the Eastern Arctic the thinning rates observed by Rothrock et al. (1999) and Yu et al. (2004) differ from each other (–0.6 and –0.1 m per decade, respectively), and the rate observed in the present study (–0.3 m per decade) lies between them. Comparison of the years 1958–1970 and 1993–1997 in (Rothrock et al., 1999) showed that the Nansen Basin, together with the Eastern Arctic, is the region of strongest thinning, while the present study covering the years 1975–2000 does not show any significant change in the region.

On the other hand, Wadhams (1990) and Wadhams and Davis (2000) observed strong thinning in the Nansen Basin also between the years 1976 and 1996. These studies are based on data not included in the NSIDC archive, and the cruise tracks extended further south than any of the Autumn cruises utilized in the present study. Wadhams and Davis (2000) observed the strongest thinning rates in the southernmost part, between latitudes 81° N–83° N, where the mean draft in 1996 was only about 30 % of the mean in 1976. At latitudes of better data coverage Wadhams and Davis (2000) reported thinning rates clearly larger than those presented here. The explanation for this significant difference is most likely linked to the spatial and temporal averaging method. Wadhams and Davis (2000) compared data from two cruises in a very narrow sector, while the present study considers a larger area and two 13-year periods. On the basis of earlier observations of thinning in the same region (Wadhams, 1990), Wadhams and Davis (2000) concluded that a substantial part of the thinning took place before 1986, during a period not well covered in the Autumn data set of NSIDC.

Tucker et al. (2001) have also examined changes in the mean draft on the basis of submarine sonar data, but in contrast to Rothrock et al. (1999), Yu et al. (2004), Wadhams (1990) and Wadhams and Davis (2000) they used data from Spring cruises. For the period 1986–1994 Tucker et al. (2001) observed substantial thinning in the western Arctic (about –1 m per decade) but the change in the North Pole region was insignificant. The longer time period considered in our analyses reveals smaller thinning rates in the Beaufort Sea and the Canada Basin (–0.8 and –0.6 m per decade, respectively), but in the North Pole region the situation is the opposite, and the longer time period shows much stronger thinning (–0.6 m per decade) than reported by Tucker et al. (2001).

The pronounced thinning in the western and central Arctic, with high initial ice thickness, has led to a decline in regional variability, and to a more uniform distribution of sea ice mass over the Arctic Ocean. A similar spatial pattern has also been observed in several model studies (e.g. Zhang et al., 2000; Bitz and Roe, 2004). In addition to the regional variation, the thinning rates presented in Table 2 also differ considerably between seasons. The thinning has generally been larger in Spring than in Autumn, implying a reduction in net ice growth over the course of the winter. Earlier analyses of submarine sonar measurements have focused on one season only, and therefore they have excluded the seasonal aspect of the thinning rate. Changes in the seasonal variability have not been much discussed in model studies, either. However, it must be taken into account that, as Bitz and Roe (2004) showed, the response of ice to the changing surface air temperature (SAT) depends on the initial thickness, and thus a small increase of SAT in the areas, and during the seasons, of thickest ice can cause a large decline in thickness.

Table 4. Fractional volume of the ice in category 3 defined using two different draft limits, $D > 3.5$ m and $D > 5$ m, in Spring and in Autumn during the periods 1975–1987 and 1988–2000, and the percentage change of the volume between the periods.

		1975–1987		1988–2000		Change	
	$D >$	3.5 m	5 m	3.5 m	5 m	3.5 m	5 m
North Pole	Spring	79.4 %	61.2 %	60.0 %	40.1 %	–38.2 %	–46.4 %
	Autumn	50.2 %	28.5 %	44.8 %	27.6 %	–19.6 %	–12.8 %
Canada Basin	Spring	73.9 %	51.9 %	59.9 %	40.2 %	–32.7 %	–35.7 %
	Autumn	55.8 %	32.5 %	40.6 %	24.2 %	–44.8 %	–43.5 %
Beaufort Sea	Spring	60.7 %	37.4 %	50.3 %	34.0 %	–41.4 %	–35.7 %
	Autumn	29.0 %	13.6 %	23.8 %	10.6 %	–31.7 %	–35.4 %
Chukchi Sea	Spring	54.4 %	33.9 %	40.9 %	24.5 %	–41.8 %	–44.1 %
	Autumn	35.9 %	20.7 %	24.4 %	11.7 %	–19.1 %	–32.8 %
Eastern Arctic	Spring	65.6 %	42.6 %	51.1 %	32.6 %	–46.2 %	–47.1 %
	Autumn	30.9 %	16.7 %	30.2 %	16.7 %	–18.5 %	–16.6 %
Nansen Basin	Spring	65.6 %	45.3 %	58.6 %	40.7 %	–7.7 %	–7.2 %
	Autumn	48.6 %	28.0 %	46.6 %	27.5 %	–2.1 %	0.3 %

4.2 Composition of the ice cover

In this study the three ice categories are classified by ice draft limits. The ice types (level FYI, level MYI and deformed ice) cannot be identified unambiguously by thickness only, because thickness ranges of different ice types are partly overlapping. In Fig. 6 and in Table 3, thickest ice category (category 3) consists of the ice with $D > 5$ m. This limiting draft was chosen to be this high, near the upper bounce of Arctic equilibrium thickness, in order to ensure that the thickest category is dominated by deformed ice. Similar criteria have been applied e.g. in the work of Wadhams and Davis (2001), while Tucker et al. (2001) defined thickest, deformed ice category as $D > 3.5$ m.

To study the sensitivity to the limiting draft value, we calculated the fractional volume and the volume change for ice category 3 using both 3.5 m and 5 m as the lower limit of the category. Table 4 shows that in most of the regions percentage changes in the volume of the thickest ice category do not vary much for different limiting draft values. Furthermore, the difference in the volume change does not exhibit any uniform pattern, i.e. in half of the regions and seasons the volume change is more pronounced for a smaller draft limit (3.5 m), while the opposite holds for the other regions. The biggest difference between the percentage volume change for different draft limits is in region 4 in Autumn, where the volume of ice with $D > 3.5$ m has decreased 19 % and the volume of ice with $D > 5$ m shows a decrease of over 30 %. Apart from this, in most of the cases differences in ice volume changes are within 5 percentage points for the two different limiting drafts.

As described in the previous section, the thinning rates estimated in different studies vary considerably, even though many of them are based partly on the same data. However, all these studies are in close agreement concerning changes in the composition of ice volume, consistent with the results presented in this paper. E.g. Wadhams and Davis (2001), Tucker et al. (2001) and Yu et al. (2004) reported a clear decrease in the concentration and fractional volume of thick, mostly deformed ice. Our study also finds that the most substantial and seasonally and regionally most uniform of all changes is the loss of thick ice, evident in the draft distributions (Figs. 3–4) and even more so in the cumulative ice volume distributions (Fig. 5). From Fig. 5 it is evident that the decline in mean ice draft occurred due to the loss of thick ice, with some regional variation in the limiting draft.

Tucker et al. (2001) reported that in the Canada Basin (at 86° N) the occurrence of deformed ice, which they defined as $D > 3.5$ m, was reduced by 20 % in the 1990s compared to the 1980s. In the North Pole region, Tucker et al. (2001) did not find changes that strong, even though the concentration of FYI showed a slight increase, and the concentration of deformed ice showed a small decrease. Our analysis covers a longer time period and a larger area. In the Canada Basin our results are in very good agreement with Tucker et al. (2001). However, in the North Pole region the longer time period presented here reveals much larger changes than reported by Tucker et al. (2001).

The observation of a shift from a PIZ to a SIZ ice pack in the Beaufort Sea is supported by e.g. Comiso (2002). They observed significant year-to-year variation in the location of the PIZ, depending mostly on ice drift forced by atmospheric circulation, but also a clear reduction in the extent of perennial ice from 1978 to 2000. This reduction was most pronounced in the Beaufort and the Chukchi Seas, along with similar changes in the eastern part of the Arctic Ocean (Comiso, 2002). The ice volume increase in thin-ice categories is not necessarily due to FYI volume increases, but may be at least in part be due to thinning of MYI.

Changes in the extent of Arctic sea ice, and especially in the extent of PIZ, have continued and even accelerated since 2000 (e.g. Maslanik et al., 2007; Comiso et al., 2008). Maslanik et al. (2007) point out that in addition to the retreat of the PIZ as a whole, the amount of the oldest and thickest ice within the remaining MYI pack has decreased significantly. In the mid-1980s 35 % of MYI consisted of ice about 2–3 years old, but by 2007 the corresponding fraction had increased up to nearly 60 % (Maslanik et al., 2007). The decrease of the modal draft up to the year 2000 (Table 2), as well as the reduction of the volume of ice in category 2 (Table 3) reflects a similar change in the average age of the ice. Even though category 2 ice can be assumed to be dominated by MYI, changes in the ice volume in this category do not necessarily directly show a change of level MYI volume, since the thickness ranges of the ice types (FYI, MYI and deformed ice) are partly overlapping. Therefore, in the case of decreasing average ice ridge thickness, more and more deformed ice may fall into ice category 2. Similarly, decrease of the level MYI thickness may result in more MYI in ice category 1.

4.3 Atmospheric forcing

Several studies have pointed out the connection between Arctic sea ice thickness and climate indices. The clear shift in the AO index from a mostly negative to a strongly positive phase in the late 1980s caused the weakening of the anticyclone around the Beaufort Sea, which was at least partly responsible for the observed thinning of Arctic Sea ice (Rigor et al., 2002). On the other hand, Lindsay and Zhang (2005) observed the strong thinning to continue after the AO index returned to near-normal conditions in the late 1990s. In addition to the AO index, variations of the DA index also have an effect on ice drift patterns, and Wu et al. (2006) state that the influence of the DA on winter sea ice motion is greater than that of the AO, especially in the central Arctic basin and north of Fram Strait. The positive phase of the DA includes a weakening of the Beaufort Gyre and a strengthening of the Transpolar Drift, which implies an increase in ice export through Fram Strait and enhanced ice import from the Laptev and East Siberian Seas to the central Arctic (Wu et al., 2006). The DA displays strong interannual variability, but it does not show any apparent trend. In any case, the time series of the DA shows several years of very high values from the late 1980s to the late 1990s (Wu et al., 2006).

Watanabe et al. (2006) studied the effect of different combinations AO and DA indices by defining four states: positive AO and positive DA (state 1), positive AO and negative DA (state 2), negative AO and positive DA (state 3), negative AO and negative DA (state 4). Watanabe et al. (2006) observed that the total sea ice export from the Arctic Ocean reaches a maximum in state 1, and a minimum in state 4. The record lows of summer sea ice extent have occurred in states 1 and 3 (Wang et al., 2009).

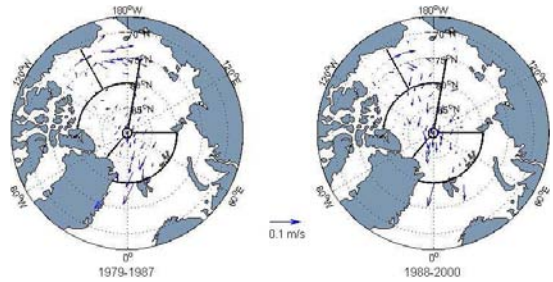

Fig. 7. Mean sea ice drift during the periods 1979–1987 and 1988–2000.

As Fig. 1 shows, our study periods 1975–1987 and 1988–2000 fall largely in different parts of the AO/DA space. During the first period more than half of the years fall in state 4, which is associated with very low ice export. During the later period the yearly values vary more, but most of the years are in state 1 or 2. A notable feature is that all the years of particularly high DA index values are in the later period (years 1988, 1995 and 1997) while very low DA index values are observed mostly in the first period. The AO index is more variable than DA, but as Watanabe et al. (2006) state, due to its strong meridionality DA seems to have a larger impact on the sea ice export than AO. This is supported by the variations in Arctic sea ice outflow through Fram Strait presented by Kwok (2009). The years of highest DA values (1988, 1995, 1997) show up as peaks in the outflow time series, and the years of very low DA values (1984, 1986 and 1991) correspond to low ice export.

We use IABP buoy data to study the differences in sea ice drift during the two periods. Figure 7 shows the average sea ice motion in the Arctic Ocean during the periods 1979–1987 and 1988–2000. IABP operations started in 1979, 4 years later than submarine data used in this study and thus the years 1975–1978 are not included. From Fig. 7 it is evident that during the former period the Beaufort Gyre was much stronger and ice in the Transpolar Drift was originated in clearly more eastern parts of the Arctic than during the later period. Due to the westward shift of the Transpolar Drift, a large fraction of the ice entering Fram Strait drifted over the North Pole, originating from the western Arctic during the later period.

The pronounced thinning in the Eastern Arctic (region 5) can be explained by these changes in ice circulation patterns. In the later period, a larger proportion of the ice advected into this region comes from the Siberian coast, being thinner FYI. A region with a very different evolution, nearly unchanged ice conditions, is the Nansen Basin (region 6). There the influence of a change in the advection pattern is opposite, and it has balanced the effect of increased SAT, the lengthening of the melt season, and the possible increase of the oceanic heat flux. During the former period ice entering the Nansen Basin

originated mostly from the SIZ of the Kara and Laptev Seas, while in the later period advection over the North Pole prevailed stronger, and included more thick ice from the central Arctic and the Beaufort Gyre. Since there are no significant changes in the ice draft distribution in the Nansen Basin, the increase of ice volume outflow in Fram Strait in the 1990s reported by Vinje (2001) has been largely due to increases in ice drift velocity, which is visible also in Fig. 7. In the western Arctic, the weakening of the Beaufort Gyre changes the dynamic forcing, resulting in a decrease in both the average age of the ice and the level of compression.

Comprehensive analysis of how the changes in the surface energy budget influence the ice thickness distribution is beyond the scope of the this paper. However, since the SAT is a result of the energy balance over sea ice, it can be used as a proxy of energy balance changes in wintertime. Figure 8 shows the difference in SAT between our two study periods, 1975–1987 and 1988–2000, calculated from ERA-40 re-analyzed data (Uppala et al., 2005). Since our findings indicate seasonally uneven changes in the ice cover, the examination of SAT is conducted separately for the preceding months in both seasons concerned, i.e. for the growth season in winter (November-March, upper figure) and the melt season in summer (June-August, lower figure). In the winter, SAT shows substantial warming only over the land area in Siberia. Over the Arctic ocean, slight warming (less than 0.5 °C) is observed only in the region north of Greenland. Over the western Arctic, wintertime SAT has even decreased by 1 °C. A simple thermodynamical ice growth model examination (Lepparanta, 1993) shows that 1 °C difference in SAT during the six months ice growing period would result at maximum only about 5 cm difference at end of growth season and thus the surface energy balance changes in winter period appear to have only a modest impact.

In the summer, changes in SAT are negligible over the entire Arctic Ocean. This is expected, since as long as the ice cover prevails, SAT is bound to the melting point of ice due to an action of sensible heat flux. However, the length of the melt season has increased in the entire Arctic Ocean, including also the western parts (Belchansky et al., 2004a). Belchansky et al. (2004b) found a connection between the AO index and the length of the melt season. They observed an increase in melt season duration by up to 2-3 weeks, beginning in year 1989 and concurrent with a strong increase in the winter AO index. Hence, the second time period analyzed in this study is characterized by enhanced melt and reduced ice growth. Third important factor influencing the ice thickness growth rates, is snowfall. Unfortunately accurate measurements of snowfall during the study period are not available. However, Polyakov et al. (1999) stated that in the regime dominated by cyclonic circulation, which was the case during most of the period 1988–2000, precipitation over the Arctic Ocean is increased in all seasons. As described in Sect. 3, changes in the ice cover have been generally more pronounced in Spring than in Autumn. One possible explanation for this seasonality could be increased winter precipitation, since the ice thickness growth rate is effectively decreased by thickening of snow cover. In the summer the impact of increased precipitation would be opposite. Enhanced summer precipitation, if assumed to fall mostly as snow, would increase the surface albedo during the melting season and thus retard melting.

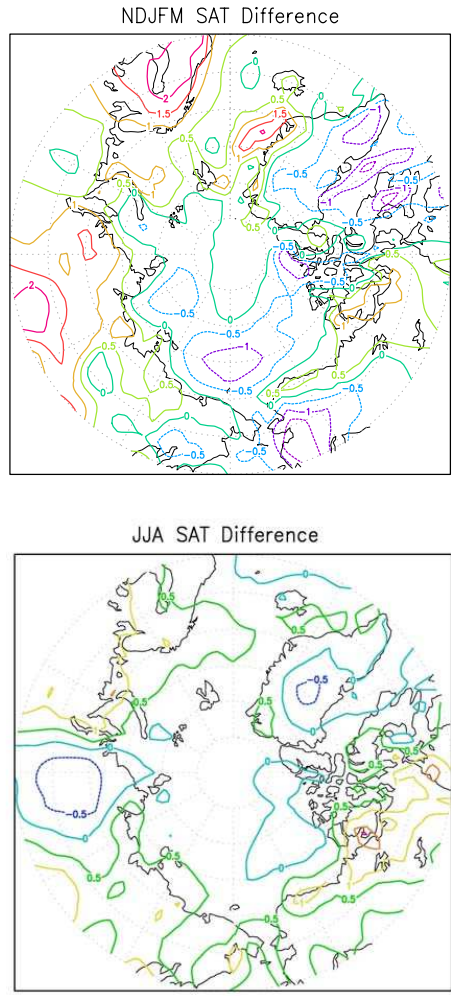

Fig. 8. Difference of surface air temperature between the periods 1975–1987 and 1988–2000. Winter months (November–March) are shown in the upper figure, and summer months (June–August) in lower figure.

5 Conclusions

In this paper we determine changes in Arctic ice draft distributions, mean and modal thicknesses, and their regional and seasonal variability under different large scale atmospheric circulation modes. We have compared characteristics of the Arctic pack ice during the periods 1975–1987 and 1988–2000, which have different distributions in the AO/DA space (Fig. 1).

A major finding of this study is that the shape of the sea ice draft distribution has changed: the peak of the ice draft distribution has generally narrowed and shifted toward thinner ice. A prevalent feature, apparent in all regions both in Spring and Autumn, is the loss of thick, mostly deformed ice, which has had an important impact on the decrease in the mean and modal ice thicknesses. In Spring the loss of the volume of ice thicker than 5 m exceeds 35 % in all regions except the Nansen Basin, and the reduction is as much as 45 % or more in the North Pole region and the Eastern Arctic. In Autumn the volume of thick, mostly deformed ice has decreased by over 40 % in the Canada Basin, with a reduction of more than 30 % in the Beaufort and the Chukchi Seas. Results also reveal a decrease in the seasonal variability of the mean ice thickness, but with strong regional differences. The regional variability of the sea ice thickness has decreased, since the thinning has been most pronounced in regions with formerly the thickest ice cover.

Ice dynamics have an essential impact on ice thickness and its distribution over the Arctic Ocean. Differences in the average ice motion during periods 1979–1987 and 1988–2000 clearly show the changes in the dynamic forcing. The shift in the drift pattern, mostly due to the weakening of the Beaufort Gyre, corresponds well with the observed strong thinning in the Beaufort Sea, the Canada Basin and the Eastern Arctic, and also with the unchanged thickness in the Nansen Basin. In the western Arctic, thinning due to dynamic forcing results from the decrease in the average ice age, and in the level of compression, while in the Eastern Arctic thinning may have been caused by the shift in advected ice source areas, leading to the dominance of SIZ on the Siberian coast. In the Nansen Basin, changes in ice advection balanced the influence of thermodynamics, as the origin of ice entering the region shifted from the dominance of seasonal ice in the Kara Sea and the Laptev Sea to a dominance of perennial ice around the North Pole.

Changes in the Arctic sea ice cover have continued and even accelerated during the last few years, as shown by the extreme minimum in ice extent recorded in September 2007 (Comiso et al., 2008). The changes in sea ice thickness characteristics described here, which occurred in the 1990s, have preconditioned the observed large decrease in the annual minimum sea ice extent. After year 2000 there have been a few submarine cruises in the Arctic Ocean, but the data is not yet freely available. The data collected during these cruises will probably show even larger changes in the draft and volume distributions than presented in this study. Comparison of statistics from the 1990s with the recent measurements of sea ice thickness by an electromagnetic method (Haas et al., 2008, 2010) show that during the last years the peak of draft distributions has changed into an even narrower form, and shifted toward thinner ice in the North Pole region.

Acknowledgements. We want to acknowledge National Snow and Ice Data Center for providing submarine sonar data set and IABP for their buoy database. ECMWF is acknowledged for providing ERA-40 reanalyzed meteorological data. We also wish to thank Jia Wang for providing AO and DA time series. We acknowledge the anonymous reviewers, whose constructive comments and suggestions were very helpful in improving the paper. This study was funded through the EU FP7 project Damocles (Development Arctic Modelling and Observing Capabilities for Long-term environmental Studies). A. Oikkonen was also supported by Academy of Finland (project 11224121).

Edited by: H. Eicken

References

Belchansky, G., Douglas, D., and Platonov, N.: Duration of the Arctic Sea Ice Melt Season: Regional and Interannual Variability, 1979–2001, J. Climate, 17, 67–80, 2004a.

Belchansky, G. I., Douglas, D. C., Alpatsky, I. V., and Platonov, N. G.: Spatial and temporal multiyear sea ice distribution in the Arctic: A neural network analysis of SSM/I data, 1988–2001, J. Geophys. Res., 109, doi:10.1029/2004JC002388, 2004b.

Bitz, C. M. and Roe, G. H.: A mechanism for the high rate of sea ice thinning in the Arctic Ocean, J. Climate, 17, 3623–3632, 2004.

Comiso, J. C.: A rapidly declining perennial sea ice cover in the Arctic, Geophys. Res. Lett., 29, 1956, doi:10.1029/2002GL015650, 2002.

Comiso, J. C., Parkinson, C. L., Gersten, R., and Stock, L.: Accelerated decline in the Arctic sea ice cover, Geophys. Res. Lett., 35, doi:10.1029/2007GL031972, 2008.

Eicken, H., Tucker, W. B., and Perovich, D. K.: Indirect measurements of the mass balance of summer Arctic sea ice with an electromagnetic induction technique, Ann. Glaciol., 33, 194–200, 2001.

Haas, C., Pfaffling, A., Hendricks, S., Rabenstein, L., Etienne, J.-L., and Rigor, I.: Reduced ice thickness in Arctic Transpolar Drift favors rapid ice retreat, Geophys. Res. Lett., 1, doi:10.1029/2008GL034457, 2008.

Haas, C., Hendricks, S., Eicken, H., and Herber, A.: Synoptic airborne thickness surveys reveal state of Arctic sea ice cover, Geophys. Res. Lett., 37, doi:10.1029/2010GL042652, 2010.

Hilmer, M. and Lemke, P.: On the decrease of Arctic sea ice volume, Geophys. Res. Lett., 27, 3751–3754, 2000.

Holloway, G. and Sou, T.: Has Arctic sea ice rapidly thinned?, J. Climate, 15, 1691–1701, 2002.

Kwok, R.: Outflow of Arctic Ocean Sea Ice into the Greenland and Barents Seas: 1979–2007, J. Climate, 22, 2438–2457, 2009.

Kwok, R. and Rothrock, D. A.: Decline in Arctic sea ice thickness from submarine and ICESat records: 1958–2008, Geophys. Res. Lett., 36, doi:10.1029/2009GL039035, 2009.

Lepparanta, M.: A review of analytical models of sea-ice growth, Atms. Ocean., 31, 123–138, 1993.

Lindsay, R. W. and Zhang, J.: The Thinning of Arctic Sea Ice, 1988-2003: Have We Passed a Tipping Point?, J. Climate, 18, 4879–4894, 2005.

Makshtas, A. P., Shoutilin, S. V., and Andreas, E. L.: Possible dynamic and thermal causes for the recent decrease in sea ice in the Arctic Basin, J. Geophys. Res., 108, doi:10.1029/2001JC000878, 2003.

Maslanik, J. A., Fowler, C., Stroeve, J., Drobot, S., Zwally, J., Yi, D., and Emery, W.: A younger, thinner ice cover: Increased potential for rapid, extensive sea-ice loss, Geophys. Res. Lett., 34, doi:10.1029/2007GL032043, 2007.

Maykut, G. A. and Untersteiner, N.: Some results from a time-dependent thermodynamic model of sea ice, J. Geophys. Res., 76, 1550–1575, 1971.

NSIDC: National Snow and Ice Data Center, Submarine upward looking sonar ice draft profile data and statistics, 1998, updated 2006.

Polyakov, I. V., Proshutinsky, A. Y., and Johnson, M. A.: Seasonal cycle in two regimes of Arctic climate, J. Geophys. Res., 104, 25761–25788, 1999.

Rigor, I. G., Wallace, J. M., and Colony, R.: Response of sea ice to the Arctic Oscillation, J. Climate, 15, 2648–2663, 2002.

Rodrigues, J.: Beamwidth effects on sea ice draft measurements from U.K. submarines, Cold Reg. Sci. Technol., 65, 160–171, 2011.

Rothrock, D. A. and Wensnahan, M.: The accuracy of sea-ice draft measured from U.S. Navy submarines, J. Atmos. Ocean. Techn., 24, 1936–1949, 2007.

Rothrock, D. A. and Zhang, J.: Arctic ocean sea ice volume: What explains its recent depletion?, J. Geophys. Res., 110, doi:10.1029/2004JC002282, 2005.

Rothrock, D. A., Yu, Y., and Maykut, G. A.: Thinning of the Arctic sea-ice cover, Geophys. Res. Lett., 26, 3469–3472, 1999.

Rothrock, D. A., Zhang, J., and Yu, Y.: The arctic ice thickness anomaly of the 1990s: A consistent view from observations and models, J. Geophys. Res., 108, doi:10.1029/2001JC001208, 2003.

Rothrock, D. A., Percival, D. B., and Wensnahan, M.: The decline in arctic sea-ice thickness: Separating the spatial, annual and interannual variability in quarter century of submarine data, J. Geophys. Res., 113, doi:10.1029/2007JC004252, 2008.

Thompson, D. W. J. and Wallace, J. M.: The Arctic Oscillation signature in the wintertime geopotential height and temperature fields, Geophys. Res. Lett., 25, 1297–1300, 1998.

Thorndike, A. S., Rothrock, D. A., Maykut, G. A., and Colony, R.: The thickness distribution of sea ice, J. Geophys. Res., 80, 4501–4513, 1975.

Tucker, W. B., Weatherly, J. W., Eppler, D. T., Farmer, L. D., and Bentley, D. L.: Evidence of rapid thinning of sea ice in the western Arctic Ocean at the end of the 1980s, Geophys. Res. Lett., 28, 2851–2854, 2001.

Uppala, S. M., Kållberg, P. W., Simmons, A. J., Andrae, U., Da Costa Bechtold, V., Fiorino, M., Gibson, J. K., Haseler, J., Hernandez, A., Kelly, G. A., Li, X., Onogi, K., Saarinen, S., Sokka, N., Allan, R. P., Andersson, E., Arpe, K., Balmased, M. A., Beljaars, A. C. M., Van de Berg, L., Bidlot, J., Bormann, N., Caires, S., Chevallier, F., Dethof, A., Dragosavac, M., Fisher, M., Fuentes, M., Hagemann, S., Hólm, E., Hoskins, B. J., Isaksen, L., Janssen, P. A. E. M., Jenne, R., McNally, A. P., Mahfouf, J.-F., Morcrette, J.-J., Rayner, N. A., Saunders, R. W., Simon, P. and Sterl, A., Trenberth, K. E., Untch, A., Vasiljevic, D., Viterbo, P., and Woollen, J.: The ERA-40 re-analysis, Q. J. R. Meteorol. Soc., 131, 2961–3012, 2005.

Vinje, T.: Fram Strait ice fluxes and atmospheric circulaiton: 1950–2000, J. Climate, 14, 3508–3517, 2001.

Wadhams, P.: Evidence for thinning of the Arctic ice cover north of Greenland, Nature, 345, 795–797, 1990.

Wadhams, P. and Davis, N. R.: Further evidence of ice thinning in the Arctic Ocean, J. Geophys. Res., 27, 3973–3975, 2000.

Wadhams, P. and Davis, N. R.: Arctic sea-ice morphological characteristics in summer 1996, Ann. Glaciol., 33, 165–170, 2001.

Walsh, J. E., Chapman, W. L., and Shy, T. L.: Recent decrease of sea level pressure in the central Arctic, J. Climate, 9, 480–486, 1996.

Wang, J., Zhang, J., Watanabe, E., Ikeda, M., Mizobata, K., Walsh, J., Bai, X., and Wu, B.: Is the Dipole Anomaly a major driver to record lows in Arctic summer sea ice extent?, Geophys. Res. Lett., 36, doi:10.1029/2008GL036706, 2009.

Watanabe, E., Wang, J., Zhang, J., Sumi, A., and Hasumi, H.: Arctic dipole anomaly and its conttribution to sea ice export from the Arctic Ocean in the 20th century, Geophys. Res. Lett., 33, doi:10.1029/2006GL028112, 2006.

Wensnahan, M. and Rothrock, D. A.: Sea-ice draft from submarine-based sonar: Establishing a consistent record from analog and digitally recorded data, Geophys. Res. Lett., 32, doi:10.1029/2005GL022507, 2005.

Wu, B., Wang, J., and Walsh, J.: Dipole Anomaly in the winter Arctic atmosphere and its association with sea ice motion, J. Climate, 19, 210–225, 2006.

Yu, Y., Maykut, G. A., and Rothrock, D. A.: Changes in the thickness distribution of Arctic sea ice between 1958–1970 and 1993–1997, J. Geophys. Res., 109, doi:10.029/2003JC001982, 2004.

Zhang, J., Rothrock, D. A., and Steele, M.: Recent changes in Arctic sea ice: The interplay between ice dynamics and thermodynamics, J. Climate, 13, 3099–3114, 2000.

II

Reprtinted, with permission, from
The Cold Regions Science ans Technology, 77-76, 83-919
doi:10.1016/j.coldregions.2011.12.005

Cold Regions Science and Technology 76–77 (2012) 83–91

Contents lists available at SciVerse ScienceDirect

Cold Regions Science and Technology

journal homepage: www.elsevier.com/locate/coldregions

A treatise on frequency spectrum of drift ice velocity

Matti Leppäranta [a,*], Annu Oikkonen [a], Kunio Shirasawa [b], Yasushi Fukamachi [b]

[a] Department of Physics, University of Helsinki, Helsinki, Finland
[b] Institute of Low Temperature Science, Hokkaido University, Sapporo, Japan

ARTICLE INFO

Article history:
Received 20 April 2011
Accepted 23 December 2011

Keywords:
Sea ice
Kinematics
Dynamics
Frequency
Spectrum

ABSTRACT

Sea ice dynamics is examined for the frequency spectra of ice velocity using mathematical models and ice motion data. The data are from the Baltic Sea and Sea of Okhotsk. A general spectrum for linear coupled ice–ocean free drift is derived and analysed. Interior dynamics shows singularity in the Coriolis (inertial) frequency and asymptotic high frequency power law of −2. In the presence of internal friction the spectrum is expected to evenly fall to zero with frictional resistance increasing above yield level. In the observations, the main spectral peak is wide at the synoptic time scales. The Okhotsk Sea spectra show inertial and tidal signals but they are missing from the Baltic Sea due to very weak tides and shallow depth damping inertial oscillations. Above semidiurnal frequency ice velocity spectra fall in power law of −5/3, inherited from atmospheric and oceanic dynamics, and at very high frequencies, above 0.5 cph (cycles per hour) the fall seems to slow down to power law below −1. The Eulerian ice velocity spectrum was higher than the Lagrangian spectrum throughout the entire obtained spectrum (0.1–5 cpd (cycles per day)). Theoretical spectra show general agreement with observations except that they have less kinetic energy at very high frequencies and much stronger inertial peak. Thus Eulerian observations are more variable than Lagrangian observations.

1. Introduction

Sea ice motion is forced by winds and ocean currents. It is a granular medium. Each ice floe performs its own individual trajectory, independently in the absence of internal stress. On scales much larger than the floe size, a continuum approximation is commonly assumed. Continuum parcels consist of a large number of ice floes. This large-scale ice is a two-dimensional, compressible and non-linear geophysical fluid at the continuum length scale, and consequently the problem and solutions are of general scientific interest. Wind acts as an independent external force, but the motion of ice is closely coupled with the ocean boundary layer (OBL). Momentum is transferred from wind to drifting ice and further to water body, or from geostrophic ocean currents and tidal currents through OBL to ice. The response of drift ice to forcing is dictated by its inertia, rheology and re-distribution of its thickness field. In closely packed fields of ice floes, internal stress is very important and can even prevent the ice from moving, while in open packing the floes drift free with no significant mutual interactions.

The first records of drift ice kinematics are from Nansen (1902). The motion of *Fram*, crossing the Eurasian side of the Arctic Ocean, was 2% of the surface wind speed directing 30° to the right from the wind direction. In later years, with accumulated database, empirical corrections for different ice conditions were applied on this relationship (Zubov, 1945), to account for the influence of internal ice stress. Also the variation of the atmospheric and oceanic drag parameters due to stratification of the boundary layers and roughness of sea ice was examined by Rossby and Montgomery (1935). These results could explain some of the observed variability in sea ice drift velocity. The presence of internal stress was known from the beginning (Nansen, 1902) but only in 1950s it was first mathematically formulated, then as a linear viscous law (Laikhtman, 1958). Plastic flow laws, corresponding to the present understanding of drift ice mechanics, were introduced 15 years later (Coon et al., 1974).

In free drift, i.e. in the absence of internal stress, atmosphere–ice–ocean forms a linear system in the first approximation (Leppäranta, 1981; McPhee, 1980; Shuleikin, 1938). Nonlinearities arise due to nonlinear ice–water drag force and momentum advection, which, however, is a minor term. In contrast, plastic drift of closely packed or compact ice fields contains highly nonlinear dynamics (Coon et al., 1974; Hibler, 1979; Pritchard, 1975). Plastic yield of drift ice is quite specific, as it shows no resistance to tension but high, strain-hardening resistance to compression. In the regime between plastic flow and free drift there is a state when interactions between ice floes are due to floe collisions (Shen et al., 1986) but the resulting internal ice stress is then small.

The physics of sea ice drift is fairly well understood (e.g., Leppäranta, 2011), but there are still relevant open questions. A particular problem is scaling of sea ice dynamics and its space–time spectrum. Temporal characteristics of ice drift have been treated in papers about drifter data (e.g., Hibler et al., 1974; Leppäranta, 1981;

* Corresponding author at: Department of Physics, University of Helsinki, P.O. Box 48 (Erik Palménin aukio 1), FIN-00014 Helsinki, Finland. Tel.: +358 9 19151016.
E-mail address: matti.lepparanta@helsinki.fi (M. Leppäranta).

0165-232X/$ – see front matter © 2012 Elsevier B.V. All rights reserved.
doi:10.1016/j.coldregions.2011.12.005

Leppäranta and Omstedt, 1990; Leppäranta et al., 2009; McPhee, 1980; Ono, 1978; Schevchenko et al., 2004; Thorndike and Colony, 1980), where the close connection with wind and the presence of Coriolis and tidal signals have been recognised. Inertia of the ice itself shows up only at very high frequencies. Less work has been done on the spatial characteristics of ice drift, and the present knowledge of spatial variability of ice motion is still only qualitative. Thorndike (1986) analysed drift buoy data for correlation structure in longitudinal (along ice motion) and transverse drift directions, and Kheysin (1978), Sanderson (1988) and Richter-Menge et al. (2002) have examined internal ice stress in different length scales. Spatial structures and scales have been discussed by Overland et al. (1995), Marsan et al. (2004), Hutchings and Hibler (2008), Goldstein et al. (2009), Rampal et al. (2009), and Stern and Lindsay (2009).

A better knowledge of scaling dynamics processes is required for research and applications. Comparisons between sea ice velocities from model simulations and Radarsat data have shown that the present models are incapable to produce spatial or temporal scaling laws that match those observed in nature (e.g., Girard et al., 2009; Leppäranta et al., 1998). The time co-ordinate presents a more straightforward problem as it can be approached using the continuum theory, but in spatial scaling one needs to go from a continuum system of ice floes to granular flow and further to interior dynamics of individual ice floes. GPS techniques are now feasible to monitor ice velocity at very high accuracy (e.g., MacMahan et al., 2009). Spatial scaling is very important for practical applications, since it is connected to forces that can act on structures. Temporal scaling is connected to short term (1 day) and very short term (1 hour) local forecasting problems for ship route planning, oil platforms, oil spills and ice pressure on ships.

In this work the frequency spectrum of sea ice drift is examined based on theoretical analysis of the equations of ice dynamics and on observations. The purpose is to combine theoretical analysis and ideal models with ice motion data to obtain a better understanding of the velocity spectrum of drift ice. We consider the structure and shape of the spectra and spectral response to forcing. First, the theory of sea ice drift is briefly introduced based on Leppäranta (2011). It is then extended to examine the ice velocity frequency spectrum. Then observed spectra, covering frequencies from synoptic time scales up to more than one cycle per hour, are analysed, and their correspondence with theory is discussed. The shape and level of observed ice velocity spectra can be well understood with the existing theory down to frequencies of about 1/3 cph (cycles per hour).

2. Sea ice dynamics theory and models

2.1. General laws

The present knowledge of the structure and mechanics of drift ice was developed during the twentieth century. The linear theory was produced by several authors (Doronin and Kheysin, 1975; Ekman, 1902; Laikhtman, 1958; Nansen, 1902; Nikiforov, 1957; Rossby and Montgomery, 1935; Zubov, 1945), and the nonlinear contribution was given by the AIDJEX (Arctic Ice Dynamics Joint Experiment) sea ice team in the 1970s (Coon, 1974; Coon et al., 1974). Since then satellite remote sensing has brought much new information, in particular in sea ice kinematics (Agnew et al., 1997; Kwok et al., 1990). Numerical models have made great progress (Coon et al., 1998; Girard et al., 2009; Hunke and Dukewicz, 1997), and ice–ocean and ice–atmosphere interaction have become much better understood (Andreas, 1998; McPhee, 2008). But the fundamental theory of sea ice dynamics holds much as it was in the 1970s. It has gained support from observations and its applicability has been widened, but detail field and remote sensing observations have also shown deficiencies in this theory (see Leppäranta, 2011).

The general system of equations of drift ice dynamics consists of the equation of motion and ice conservation law:

$$\rho h\left(\frac{\partial \boldsymbol{u}}{\partial t}+\boldsymbol{u}\cdot\nabla\boldsymbol{u}+f\boldsymbol{k}\times\boldsymbol{u}\right)=\nabla\cdot\sigma+\tau_a+\tau_w-\rho g h\nabla\xi \tag{1a}$$

$$\frac{\partial J}{\partial t}+\boldsymbol{u}\cdot\nabla J=\psi+\phi \tag{1b}$$

Here ρ is ice density, h is mean ice thickness, $\boldsymbol{u}$ is ice velocity, t is time, f is Coriolis parameter, $\mathbf{k}$ is unit vector vertically upward, $\sigma=\sigma(J,\varepsilon,\dot{\varepsilon})$ is internal ice stress, $\varepsilon$is strain and $\dot{\varepsilon}$ is strain-rate, J is the ice state containing the relevant material properties of drift ice, $\boldsymbol{\tau}_a$ is wind stress, $\boldsymbol{\tau}_w$ is water stress, g is acceleration due to Earth's gravity, ξ is sea surface elevation, ψ is ice state change due to mechanical deformation, and ϕ is ice state change due to freezing and melting. Internal stress is related to the deformation of the continuum, while stress divergence contributes to the momentum balance. In the case of sea ice these forces are frictional — they consume mechanical energy in an irrecoverable manner.

Ice state should contain at least ice compactness A and mean ice thickness, $J=\{A, h\}$, or a more complete ice thickness distribution (Thorndike et al., 1975). Free drift ($\sigma\equiv0$) assumption is valid for $A<0.7$–0.8, but for higher compactness, a plastic flow law (Coon et al., 1974; Hibler, 1979) is employed. Then the strength of drift ice is determined by ice thickness and compactness. In floe collision models (Shen et al., 1986), valid for compactness less than about 0.8 or less, the strength depends also on the floe size, but the resulting internal stress remains low.

Ice–ocean or ice–atmosphere interaction takes place in the boundary layer or Ekman layer of ocean or atmosphere. Assuming that the ocean depth is more than Ekman depth or the boundary layer thickness, the sea surface pressure gradient term can be determined using the geostrophic flow law: $-g\nabla\xi=f\mathbf{k}\times\boldsymbol{U}_{\mathbf{wg}}$, where $\boldsymbol{U}_{\mathrm{wg}}$ is the geostrophic current velocity (e.g., Gill, 1982; McPhee, 2008). Quadratic drag laws are normally employed for the air and water stresses on ice (Brown, 1980; McPhee, 1980, 2008):

$$\tau_a=\rho_a C_a U_a(cos\theta_a\mathbf{U}_a+sin\theta_a\mathbf{k}\times\mathbf{U}_a) \tag{2a}$$

$$\tau_w=\rho_w C_w|\mathbf{U}_w-\mathbf{u}|[\cos\theta_w(\mathbf{U}_w-\mathbf{u})+\sin\theta_w\mathbf{k}\times(\mathbf{U}_w-\mathbf{u})] \tag{2b}$$

where ρ_a and ρ_w are air and water densities, C_a and C_w are air and water drag coefficients, $\boldsymbol{U}_a$ and $\boldsymbol{U}_w$ are air and water velocities, and θ_a and θ_w are air and water turning angles. In exact terms, in Eq. (2a) wind velocity should be replaced by the relative velocity of wind with respect to ice velocity, $\boldsymbol{U}_a-\boldsymbol{u}$. But since $\boldsymbol{u}\ll\boldsymbol{U}_a$, the used approximation is good. Parameterization of these drag laws was thoroughly examined in AIDJEX programme in the 1970s (Brown, 1980; McPhee, 1980).

The system of equations of sea ice dynamics (Eqs. (1a), (1b)) contains three time scales. The immediate response is determined by the time scale of ice inertia:

$$T_I=\frac{H}{C_w U} \tag{3}$$

where H and U are the ice thickness and velocity scales, respectively. Since $H\sim1$ m, $U\sim0.1$ m s^{-1}, and $C_w\sim5\times10^{-3}$ (McPhee, 1980), we have $T_I\sim1/2$ h. The second time scale is given by the pendulum day $2\pi f^{-1}$, which is about 14 h in the Baltic Sea and about 17 h in the Sea of Okhotsk, and the third time scale is the deformation time scale, which can be taken as the inverse of strain rate magnitude, in the seasonal sea ice zone $|\dot{\varepsilon}|^{-1}\sim10$ *days*. Timescale of ice inertia is determined by the ice–water drag force, pendulum day is determined by the Coriolis acceleration, and deformation time scale is determined by the ice strength. Clearly we have

$$T_I<<2\pi f^{-1}<<|\dot{\varepsilon}|^{-1} \tag{4}$$

Inertial timescale of very thin ice (less than 10 cm) is down to 5 min, and in the Central Arctic the deformation time scale is up to 100 days. Inertial timescale is proportional to the thickness of ice, while deformation time scale is related to thickness via ice strength.

The dynamics of sea ice is strongly coupled with the dynamics of the oceanic boundary layer (OBL) beneath. In the linear theory, advection is ignored and ocean current velocity can be split into geostrophic and Ekman flow parts (e.g., Gill, 1982; McPhee, 2008), $\boldsymbol{U}_w = \boldsymbol{U}_{wg} + \boldsymbol{U}_{wE}$. The former part is obtained from large-scale geostrophic dynamics, while the latter part is closely coupled with ice:

$$\frac{\partial \boldsymbol{U}_{wE}}{\partial t} + f\mathbf{k} \times \boldsymbol{U}_{wE} = \frac{\partial}{\partial z}\left(K_v \frac{\partial \boldsymbol{U}_{wE}}{\partial z}\right) + K_H \nabla^2 \boldsymbol{U}_{wE} \tag{5a}$$

$$z = 0 : K_v \frac{\partial \boldsymbol{U}_{wE}}{\partial z} = -\frac{\tau_w}{\rho_w}; z \to -\infty : \boldsymbol{U}_{wE} \to 0 \tag{5b}$$

where K_v and K_H are the vertical and horizontal turbulent viscosities, and z is the vertical co-ordinate.

2.2. Linear free drift

In free drift, the internal ice stress is ignored. It is easy to see by scaling analysis that momentum advection is practically always a small term in sea ice drift (Leppäranta, 2011, Section 5.4). In more exact terms, the ice–water drag coefficient is larger than 10^{-3}, and the length scale in free drift is limited from below by the baroclinic Rossby radius of deformation in the OBL. Assuming $H/L < 10^{-4}$, where L is the length scale, the ratio of advection to ice–water stress can be estimated as

$$\frac{\rho U^2 H/L}{\rho_w C_w \hat{U}^2} \approx \frac{(H/L)U^2}{C_w \hat{U}^2} < 10^{-1} \times \left(\frac{U}{\hat{U}}\right)^2 \tag{6}$$

where U is ice velocity scale, and $\hat{U} = |\mathbf{u} - \mathbf{U}_w|$ is the scale of ice–water velocity difference. Thus only when $\hat{U} \ll U$ can advection be important; this means that ice must basically follow the surface current, with insignificant wind stress or internal friction. Sea ice drift is then solved as part of the ocean dynamics problem, and momentum advection may be important in intensive dynamics situations.

Ignoring momentum advection, free drift becomes a local problem, $\boldsymbol{u} = \boldsymbol{u}(t)$. The steady-state free drift equation can be easily solved for the ice velocity relative to the geostrophic ocean current, $\hat{\mathbf{u}}_g = \mathbf{u} - \mathbf{U}_{wg}$, showing that ice motion is the sum of pure wind-driven drift and geostrophic current (e.g., Leppäranta, 2011, Section 6.1). The non-steady situation can be analysed by subtracting the time derivative of geostrophic current from both sides of the free drift equation. Eq. (1a), ignoring advection and ice stress, gives:

$$\rho h\left(\frac{d\hat{\mathbf{u}}_g}{dt} + \boldsymbol{f}k \times \hat{\boldsymbol{u}}_g\right) = \tau_a + \rho_w C_w \left|\boldsymbol{U}_{wE} - \hat{\boldsymbol{u}}_g\right|\left(\boldsymbol{U}_{wE} - \hat{\boldsymbol{u}}_g\right) - \frac{d\boldsymbol{U}_{wg}}{dt} \tag{7}$$

The negative time derivative of geostrophic current becomes a driving force for $\hat{\mathbf{u}}_g$. However, the inertial time scales of ice velocity and geostrophic current differ by one order of magnitude: their ratio is $T_i f \sim 10^{-1}$. Thus inertial ice processes can be examined with fixed geostrophic current, while for variable geostrophic current, quasi-steady ice dynamics can be assumed.

In the linear theory, a linearized drag coefficient is employed: $C_{w1} = C_w \hat{U}$. Integrating Eq. (5a) and (5b) across the OBL, assuming horizontal homogeneity, ice and oceanic boundary layer dynamics can be written in general form as:

$$\frac{d\hat{\mathbf{u}}_g}{dt} = \frac{\rho_w C_{w1}}{\rho h}\left(\tilde{\mathbf{U}}_{we} - \hat{\mathbf{u}}_g\right) - f\mathbf{k} \times \hat{\mathbf{u}}_g + \frac{\tau_a}{\rho h} - \frac{d\boldsymbol{U}_{wg}}{dt} \tag{8a}$$

$$\frac{d\tilde{\boldsymbol{U}}_{wE}}{dt} = \frac{\rho_w C_{w1}\left(\hat{\boldsymbol{u}}_g - \tilde{\boldsymbol{U}}_{wE}\right)}{\rho_w D} - f\boldsymbol{k} \times \tilde{\boldsymbol{U}}_{wE} \tag{8b}$$

where D is sea depth and $\tilde{\mathbf{U}}_{wE}$ is the vertically averaged Ekman current velocity. We have taken, for simplicity, zero turning angle in the ice–water stress formula. Forcing of this coupled system is by wind stress and geostrophic ocean current. Eqs. (8a), (8b) form a pair of linear equations, and they can be easily solved using the elimination method (Leppäranta, 2011, Section 6.3; also consult basic calculus textbooks, such as Adams, 1995). Briefly, $\tilde{\mathbf{U}}_{wE}$ is eliminated and then a second-order equation is obtained for $\boldsymbol{u}$. The ice velocity is then is a linear function of the forcing, and the spectrum is directly obtained from the forcing spectrum (e.g., Jenkins and Watts, 1968). The resulting spectrum $p = p(\omega)$ of the relative sea ice velocity $\hat{\mathbf{u}}_g$ is:

$$p(\omega) = \frac{\lambda_i^2 + \omega^2 + f^2}{\left[(\lambda_i + \lambda_w)^2 + (\omega + f)^2\right](\omega + f)^2} p_F(\omega)$$
$$\lambda_i = \frac{\rho_w C_{w1}}{\rho_i h}, \lambda_w = \frac{C_{w1}}{D} \tag{9}$$

where ω is frequency, λ_i and λ_w are ice and Ekman layer inverse response times, respectively, and $p_F(\omega)$ is the spectrum of the forcing. The spectrum can be expressed as $p = a p_F$, where $a = a(\omega)$ is the spectral modulation factor; a can be taken as the spectral response to white noise forcing. There is one singularity, at the Coriolis frequency $\omega = -f$. Coriolis acceleration (or "Coriolis force") acts perpendicular to the direction of ice drift, to the right in the northern hemisphere, giving rise to clockwise inertial oscillation in the ice drift (e.g., Gill, 1982).

Fig. 1 shows the rotary spectrum (see Gonella, 1972) of ice drift based on the coupled ice–ocean model (Eqs. (8a), (8b)). Positive (negative) frequencies describe counterclockwise (clockwise) cycles. The modulation factor a is dominated by the ice response, since $\lambda_i \gg \lambda_w, f$, and by the singularity at the Coriolis frequency. Asymptotically, $a(\omega) \to$ constant as $\omega \to 0$, and $a(\omega) \propto \omega^{-2}$ as $\omega \to \pm\infty$. At frequencies smaller than 0.016 cph (2.6-day period) the modulation factor becomes flat, and at frequencies larger than 1 cph the power law of -2 appears. The spectral density is higher in the negative side for all frequencies. One may question how the simple drag law works for high frequencies. Omstedt et al. (1996) showed that the quadratic drag force differs little from the drag force obtained directly from a 2nd order turbulence model down to frequency of 0.25 cph (their analysis did not go to higher frequencies).

The full free drift spectrum can be compared with two specific cases (Fig. 2): (a) Ice-only, where the ocean is passive (i.e., Eq. (8a) with $\boldsymbol{U}_{wg} =$ constant and $\tilde{\mathbf{U}}_{wE} = 0$), and (b) Locked ice–ocean (McPhee, 1978), where together (Eqs. (8a) and (8b) added together):

$$p_i(\omega) = \frac{p_F(\omega)}{\lambda_i^2 + (\omega + f)^2} \tag{10a}$$

$$p_{iw}(\omega) = \frac{1}{(\omega + f)^2} \cdot \left(\frac{\rho h}{\rho h + \rho_w D}\right)^2 p_F(\omega) \tag{10b}$$

respectively. The factor in parenthesis in Eq. (7) is due to that much larger mass is driven in locked ice–OBL case; it is of the order of 10^{-3}. Both peak at $\omega = -f$, but the peak is very weak in the ice-only case. They both decay as ω^{-2} when $\omega \to \pm\infty$. The ice response time dominates the ice–only spectrum, and the red band starts at the frequency of about 0.3 cph. In the locked ice–OBL case, Coriolis frequency dominates. The spectrum is similar to the coupled case but the level of variance is much lower. An ice model with 'inertial embedding' was presented by Heil and Hibler (2002). Sea ice velocity is extracted from the locked ice–ocean velocity by assuming a drag coefficient and a turning angle. The stationary solution is correct,

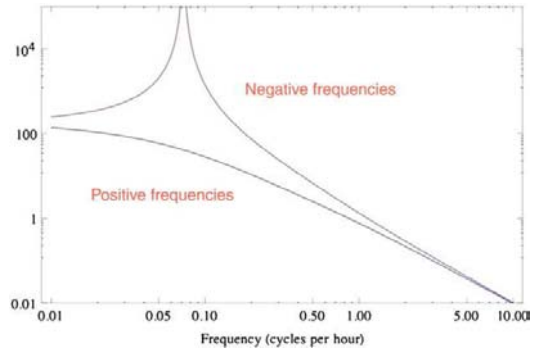

Fig. 1. Spectral response of free ice drift to white noise forcing based on a coupled ice–ocean boundary layer model shown by rotary spectrum. Upper curve: negative frequencies; lower curve: positive frequencies. Vertical scale is arbitrary.

and therefore low frequencies are reproduced very well in the ice velocity spectrum. Also the inertial peak comes out well but at higher frequencies the spectrum falls off too fast.

The obtained spectra are based on the linear theory. Next we consider how the nonlinearities in free drift may influence on the spectrum of ice velocity. The full equation (Eqs. (1a) and (2b)) has two nonlinear terms: momentum advection and ice–water stress. The former would transfer energy to higher frequencies — as usually in turbulent flow — but it is a very small term in sea ice dynamics. In free drift driven by intensive ocean dynamics advection can become important but then the ice essentially traces ocean currents (see Eq. (6) and discussion there). Ice–water stress is well approximated by a quadratic law but the dependency is of the form $\tau_w \propto |\hat{\mathbf{u}}|\hat{\mathbf{u}}$, which transforms the form of a forced sine wave for sea ice velocity but does not influence on the frequency (Fig. 3). In the quadratic case, ice responds faster to changes in forcing than in the linear case.

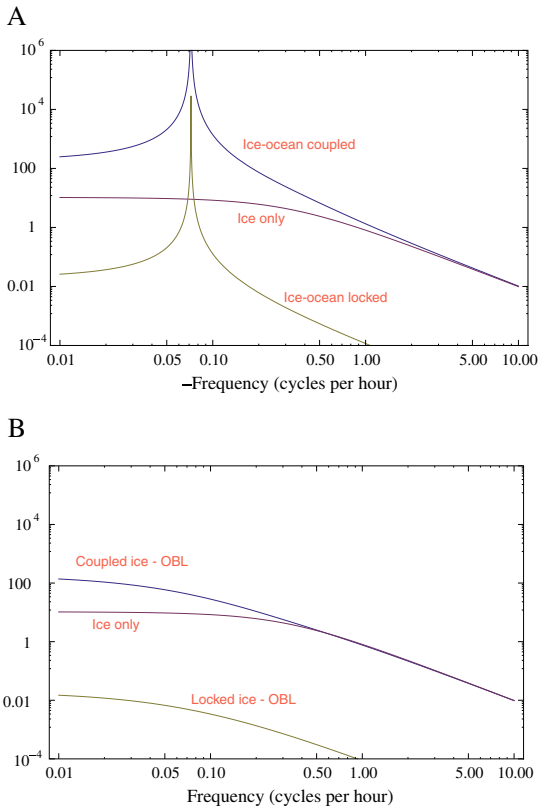

Fig. 2. Sea ice velocity spectra normalized by forcing, from top down ice–ocean coupled model, ice only model, and locked ice–ocean model: (a) Negative frequencies, (b) Positive frequencies. Latitude is 60°N, where Coriolis period is 13.9 h.

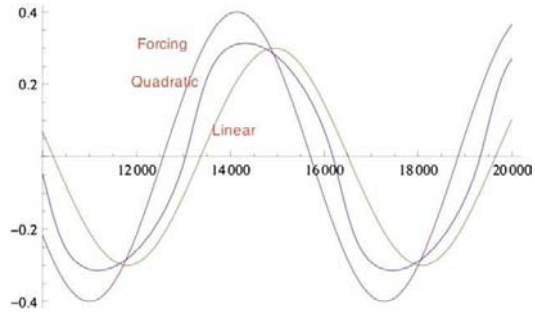

Fig. 3. Simulated time series of free drift ice velocity for quadratic and linear water drag forced by a sine wave. Horizontal scale is in seconds, vertical in m s^{-1}. Drag law parameters have been tuned to give the same ice velocity amplitude in both cases.

2.3. Drift in the presence of internal stress

Internal stress in drift ice is due to interaction between ice floes (see, e.g., Leppäranta, 2011, Chapters 4 and 7). Plasticity of drift ice is characterized by high compressive strength and low tensile strength and sensitivity to ice compactness (Coon et al., 1974). Also drift ice is strain hardening under compression but becomes unstable in shear.

In general, internal stress ranges from stress-free state to plastic flow (e.g., Leppäranta, 2011, Section 7.1). The effect on motion therefore ranges from zero in free drift to dominant when stress is on the yield surface. We can examine the range of rheologies by a family of viscous models:

$$\sigma = g_n(\dot{\varepsilon}_I, \dot{\varepsilon}_{II})\dot{\varepsilon}, n \geq -1 \tag{11}$$

where g_n is nth degree homogeneous function (i.e., $g_n(ax, ay) = a^n g(x, y)$), and $\dot{\varepsilon}_I$ and $\dot{\varepsilon}_{II}$ are strain-rate invariants equal to the sum and difference of the principal strain rates. At compactness ~0.8, stress is transferred by collisions between ice floes, and the resulting rheology is super-linear, $n = 1$ (Shen et al., 1986); however, the resulting stresses are then small. For $n = 0$, a linear viscous law results, while for $-1 < n < 0$ we have sub-linear viscous laws approaching a plastic law as $n \to -1$. For a harmonic velocity component $u = u(x, y)\exp(-i\omega t)$, the acceleration has frequency $(n+1)\omega$, and the internal friction is comparable to the acceleration. If $n < 0$ ($n > 0$), kinetic energy is transferred toward lower (higher) frequencies, while for $n = 0$ the system is linear and no cross-frequency energy transfer takes place.

Thus in sub-linear viscous flow, kinetic energy is transferred from higher to lower frequencies. In the case of drift ice, however, the rheology possesses asymmetry in that there is strong resistance to compression but very small resistance to tension. Coupling the ice conservation and momentum equations introduces some interesting features. Since the ice stress is nonzero only during convergence, the frequency of an opening/closing cycle is transferred to the ice velocity spectrum. Thus, for any n is the ice moves, its velocity is forced into the deformation frequency, and deformation frequency follows the forcing frequency. Summer and winter ice velocity spectra from the Arctic Ocean illustrate the influence of the internal stress (Thorndike and Colony, 1980); the summer situation is closer to free drift while in winter, internal stress is important. The spectra

look similar, and the main differences are that in winter the overall level of spectral density is one order of magnitude lower and the semidiurnal peak is weak. There is no indication of cross-frequency energy transfer due to internal stress.

Consider a one-dimensional channel closed at one end (see Leppäranta, 2011, Section 7.2). Assume that the wind blows toward the channel end with small, cyclic variation around the mean. Then the ice will move toward the closed end but less during each wind cycle until it finally stops. The steady state situation is a stationary ice field. The ice velocity spectrum has a peak at the wind frequency and the height of the peak goes to zero with time due to the strain hardening of the ice field. In coastal shear flow (see Leppäranta and Hibler, 1985) a steady oscillating plastic flow solution is possible as $v = a|\boldsymbol{U}_a|$, where the coefficient a is a non-linear function of the wind direction. Again, the ice motion follows the wind frequencies. In both channel flow and shear flow cases, however, the behaviour of ice motion is unclear at very high frequencies where neither observations nor detailed model studies are available. Thus we must ask to how high are frequencies for which the above results are valid.

To examine the spectra of ice velocity in the presence of internal stress, a series of numerical experiments was performed by Leppäranta et al. (2009). Ice response was simulated with an oscillating wind in a rectangular basin. Wind speed was constant but the direction turned clockwise one cycle in a given periods. Different periods were used in a number of simulations. The Hibler (1979) viscous-plastic rheology was employed. Phase shift followed the forcing but no change in the frequency space was observed. However, there was a limitation in these experiments because the momentum advection term was ignored.

The above more or less heuristic reasoning based on the theory of sea ice drift suggests that in the presence of internal stress the frequency of ice drift follows the forcing frequencies but amplitude response is highly nonlinear. No observational evidence contradicts this. However, at very high frequencies the situation is unclear due to lack of accurate observed drift data.

3. Observations

3.1. Data collected

Many observation programmes have been performed on sea ice kinematics, and, consequently a number of papers have been published on ice velocity time series analyses (e.g., Geiger and Perovich, 2008; Hibler et al., 1974; Hutchings and Hibler, 2008; Leppäranta, 1981; McPhee, 1980; Ono, 1978; Schevchenko et al., 2004; Thorndike and Colony, 1980). Here ice motion data from two different kinds of basins are used to extend the empirical knowledge toward higher frequencies and to compare the observed spectra of ideal models.

Observations of ice motions from the Baltic Sea and Sea of Okhotsk are used. These basins are located in the seasonal sea ice zone; the thickness of ice is of the order of half meter. The latitudes of the sites are close to 65°N in the Baltic Sea site and 45°–50°N in the Sea of Okhotsk. The data, collected in field experiments in 2005 (Sea of Okhotsk) and 2009 (Baltic Sea), include both Lagrangian and Eulerian velocities. They were obtained from drifting stations, drift buoys and Acoustic Doppler Current Profiler (ADCP). Fig. 4 shows maps of the drift paths. In the Sea of Okhotsk, one buoy was drifting close to an ADCP mooring site and consequently simultaneous Eulerian and Lagrangian velocities were obtained.

In the Baltic Sea the ice season lasts on average seven months with the northern basins freezing over in normal years (Leppäranta and Myrberg, 2009). The surface area is 0.40×10^6 km^2 and the average depth of the Baltic Sea is 54 m. Strong winds blow mainly from southwest to west directions. Water circulation is wind-driven with weak permanent currents, and consequently sea ice dynamics is primarily

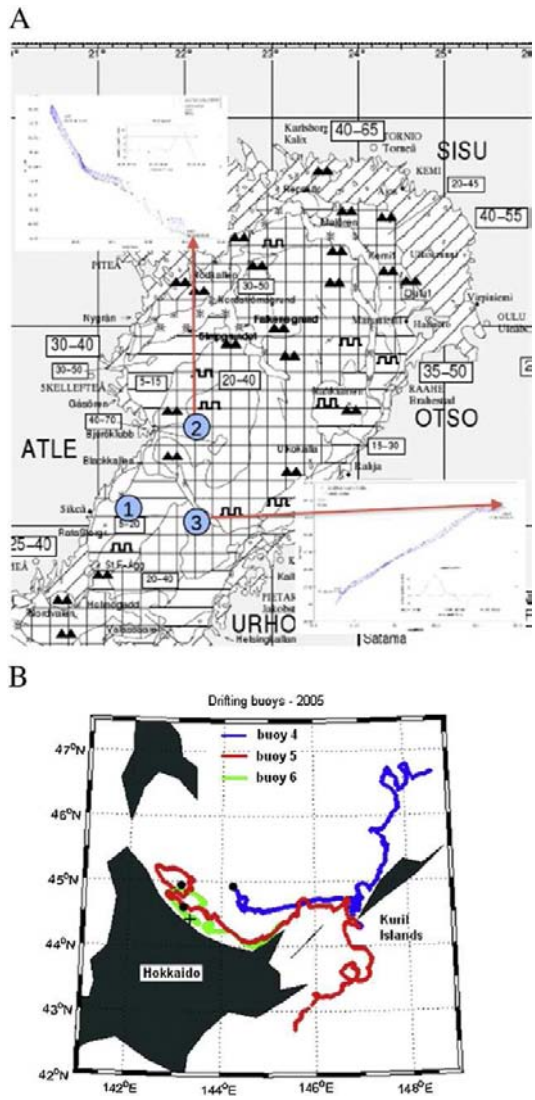

Fig. 4. The drift data. (a) Baltic Sea drifting stations S2 and S3, March 2009. Ice chart is shown on the background map (width 290 km) and drift paths enlarged in the rectangles (long sides 20 km).(b) Sea of Okhotsk drift buoys #4–6 and ADCP mooring site (×), winter 2005, shown on map of the southern Sea of Okhotsk.

wind-driven. The Sea of Okhotsk is a much larger basin (surface area 1.5×10^6 km^2 and mean depth 838 m), and the ice season coverage is 60–75% of the total area at its annual maximum. Sea ice drift is driven by wind, permanent current system and tides. The permanent water circulation contains a basin-wide gyre with warm Soya current flowing east along the northern coast of Hokkaido. The tides are dominated by the diurnal constituents.

Lagrangian velocities have been obtained by first-order differencing of positions. Assuming positioning error to be white noise with variance σ_e^2, the velocity error becomes blue noise with variance spectrum

$$\sigma^2(\omega) = \frac{\sigma_e^2[1-cos(\omega\delta t)]}{\pi\delta t},\ 0\le\omega\le\frac{\pi}{\delta t} \tag{12}$$

where ω is frequency and δt is the observation time interval. Especially good positioning accuracy is needed to obtain the very high frequency spectra of sea ice velocity. GPS noise decreases at high frequencies (Hutchings and Hibler, 2008; MacMahan et al., 2009) and thus the white noise assumption above is a conservative underestimate of the GPS accuracy. Eulerian velocities are included in the ADCP data directly, and their error can be taken as white noise with variance depending on the instrument.

The Baltic Sea data are from a field campaign aboard R/V Aranda in March 2009 in the northern basin, the Bay of Bothnia. Ice motion has been obtained from positions of the ship moored to ice. Furuno Differential GPS was used for this, its accuracy according to the manufacturer is better than 5 m; thus we take 5 m to represent the accuracy as twice the standard deviation of error. The positions were recorded at every 10 seconds and averaged over 5-minute intervals, and ice velocity was determined from these average positions at the same intervals. The time series of two drifting stations (S2 and S3) were taken for the present analysis (see Fig. 4a).

In the Sea of Okhotsk, three GPS buoys (#4, #5 and #6) were deployed on sea ice on the coastal zone at Hokkaido. The location of the buoys was recorded every hour, with positioning accuracy of 10 m. Two (#5 and #6) stayed close to each other in the vicinity of Hokkaido coast, although Buoy #5 drifted south through a strait in Kuril Islands. Buoy #4 drifted further out from the coast and stayed in the southeastern part of the Sea of Okhotsk. After drifting nearly two months it was about 400 km northeast from Hokkaido. Buoys No. 5 and 6 remained close to the coast of Hokkaido during the entire time.

During the ice drift experiment an ADCP (RD Instruments WH-Sentinel 300 kHz) was moored in the proximity of the north coast of Hokkaido (position 44°28.3'N, 143°25'E, depth 48 m). The ADCP was, using bottom tracking, measuring the Eulerian velocity of ice drifting over the mooring site with sampling interval of 15 min. Single ping standard deviations were 0.7, 1, and 1.5 cm for speeds of 1, 3, and 5 m s^{-1}. Using the first value and bottom-track ping, the accuracy of velocity is 0.22 cm s^{-1}. For the spectral analyses 1 h average velocities were used. ADCP was deployed for over 2.5 months, from 6 January through 25 March 2005; however it provides ice velocity measurements only when ice is present above the instrument. Since the ice concentration in the southern Sea of Okhotsk varies greatly over a few days, continuous ice velocity time series exist only for duration of 3–7 days. Buoy #6 drifted most of the time in the proximity of the ADCP, and the data that it collected less than 100 km away from the ADCP mooring site is used for the comparison of Eulerian and Lagrangian frequency spectra.

3.2. Ice velocity spectra from drifter data

The spectral calculations were performed with MatLab software using the Welch method. In the Baltic Sea case, Hann window was used on the 5-minute interval data. Segment length was 120 measurements and segment overlap was 75%. In the Sea of Okhotsk case, the time series were divided into 5 days long overlapping segments (75% overlap) and the segments were weighted using Kaiser–Bessel window. Due to the shortness of the segment needed to increase the statistical reliability, the low frequency threshold is 0.2 cpd (cycles per day). However, this enables the distinction between diurnal tidal, Coriolis and semidiurnal tidal responses with periods of 24 h, 16.9 h (latitude 45ºN) and 12 h, respectively. The spectral resolution is anyhow insufficient for the separation of main diurnal tidal constituents, K1 and O1. To have good outcome for confidence intervals, different weighting windows were used because of the large differences in the lengths of the individual time series. The confidence intervals plotted in the spectra were provided automatically by MatLab software.

First, consider the basic structure of sea ice velocity spectra. In the Baltic Sea ice velocity spectra are dominated by synoptic frequencies (Leppäranta and Omstedt, 1990). Here the focus is on frequencies higher than one cycle per day. Fig. 5 shows spectra from the Baltic Sea together with the corresponding wind spectra (wind velocity has been scaled by the factor of 0.02 to represent linear free drift approximation). Station S3 represents free drift while in Station S2 strong pressure was observed in the drifting ice (see Fig. 4a). The difference between the spectra of S2 and S3 is, however, small: S2 has higher level at frequencies higher than 0.1 cph, while at lower frequencies the situation is opposite. Wind, on the other hand, shows similar spectral characteristics in both cases.

Coriolis or inertial oscillation (0.075 cph) is not present in these spectra although the free drift theory includes a singularity at this frequency (see Eq. (9)). This oscillation develops in the ocean boundary layer and from there it is fed into ice drift. In this basin inertial oscillations are weak in winter because of frictional damping by bottom friction due to shallow depth and lack of stratification, although in summer inertial oscillations show up well (Leppäranta and Omstedt, 1990). Internal friction of ice also damps the Coriolis acceleration (Thorndike and Colony, 1980), but the present data support the bottom friction as the main factor.

The spectra are falling down from the synoptic scales, and through 0.1 to 0.5 cph the fall is steepest with slope quite close to $-5/3$. This is inherited from the atmospheric and oceanic boundary layers, and tells of wind acting as the driving force since the spectral level of the ice velocity is close to the level of 2%-wind. Interestingly, in the presence of internal stress (Station S2) ice drift is below 2%-wind up to 0.15 cph but thereafter above, while the free drift case (Station S3) is slightly below 2%-wind at high frequencies; however, these features are too weak for firm conclusions.

In the Sea of Okhotsk, although the drifting paths of the buoys separated and the buoys drifted in distinct regions with different ice and oceanographic conditions (Fig. 4b), their mean velocities varied only slightly, between 25 and 29 cm/s. In February 2005 all the buoys

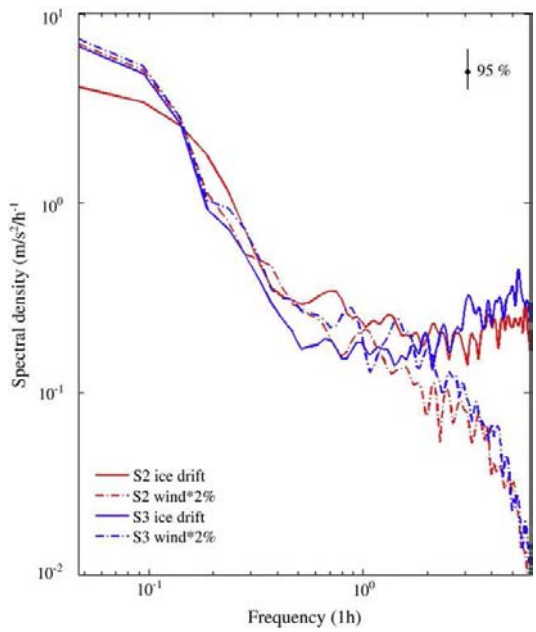

Fig. 5. Ice velocity spectra (solid lines) and corresponding wind spectra (dashed lines) for the drifting stations S2 and S3 in the Baltic Sea, winter 2009. The ice velocities are based on R/V Aranda moored to ice floe.

were located in compact ice fields with concentrations of 80–100%. After a few days, ice concentration decreased and the buoys started to diverge. Later on, ice concentration varied strongly, but generally the highest concentrations occurred close to the northeast coast of Hokkaido and along the north coast of Kuril Islands. During the nearly 2 month period of ice drift, the wind speed was generally weak, exceeding 8 m/s only twice, although it varied strongly.

Fig. 6 shows ice velocity spectra from the Sea of Okhotsk based on three drift buoys in winter 2005. The spectral range from 0.1 to 5 cpd is above the measurement noise. Compared with the Baltic Sea, there are similarities and differences. In low frequencies there are more variations in the Sea of Okhotsk due to current and tidal systems. The spectral slope above synoptic frequencies is similar but in the Sea of Okhotsk tidal and Coriolis signals are seen. Diurnal tide gives a strong and wide peak, and inertial (Coriolis) oscillations (1.41 cpd) can also be identified. The presence of inertial signal in this region was shown by Ono (1978). Semidiurnal tide is not clear. In frequencies higher than 1 cpd the spectra fall down at about the slope of −5/3 up to 5 cpd as in the Baltic Sea. Here higher frequencies are not available.

3.3. Very high frequencies

In sea ice dynamics it is convenient to define 'very high frequencies' by the frequencies where the inertia of ice plays an important role. Scaling the equation motion, it is seen that the importance of inertia is characterised by the Strouhal number $\mathrm{Sr} = UT/H$ (see Leppäranta, 2011), which provides the inertial time-scale as shown in Eq. (3), $T_\mathrm{I} = H/(C_\mathrm{w}U) \sim 1/2$ h. We can take the band of very high frequencies to start from somewhat below T_I^{-1}. To examine these frequencies requires excellent measurement accuracy, such as there is in the present Baltic Sea data. Hourly velocity fluctuations are of the order of 1 cm s^{-1}, which cause displacements up to 36 m in one hour. The positioning accuracy should be at least an order of magnitude better. With accuracy of 5 m or better in the Baltic Sea drifting stations, the present work has acceptable accuracy, although still one order of magnitude better would be desirable. The present accuracy is enough to produce spectra up to a little above 1 cph.

Above the frequency of 0.1 cph, the Baltic Sea spectra first fall following the −5/3 power law (Fig. 5). Then the slope changes at about 0.5 cph. At higher frequencies the spectral density is flatter, falling weaker than power law of −1. The change in the power reflects changing in the dynamics of ice from quasi-steady drift under air–ocean forcing to a non-steady ice regime. The measured ice drift spectra reach the measurement noise given by Eq. (12) above 1 cph (Fig. 5). At 0.5 cph the measured spectra are well above the noise level. The blue form of the noise spectrum is clearly revealed at higher frequencies, coming as rising line toward higher frequencies.

In the linear free drift theory, in very high frequencies the spectral modulation factor (see Eq. (9) and the lines below it) approaches asymptotically a power law of −2 as $\omega \to \pm\infty$. This power law comes from the inertia of ice. The power of ice velocity spectrum is then equal to the sum of powers of the modulation factor and wind spectrum, asymptotically equal to $-2-5/3 = -11/3$ as $\omega \to \infty$. The linear theory is an idealized case and the results here suggest that features not present in the linear theory become important in high frequencies.

A remarkable feature is that the fall of ice velocity spectrum becomes weaker instead of becoming stronger as predicted by the linear free drift theory (Eq. (9)). Possible reasons behind this weak slope above 0.5 cph could be the following: (i) random shifts of ice floes due to floe–floe interactions, (ii) quadratic ice–water drag law, and (iii) shallow water waves in the water body. There is a natural variation in the drift of individual floes due to their different thicknesses and form drags, since free drift is determined by the drag parameters, Rossby number $U/(Hf)$, and the inertial time scale. The response time in ice motion is independent of actual ice speed in the linear drag law but in the quadratic case it is inversely proportional to ice speed:

$$T_{I1} = \frac{H}{C_{w1}} = \frac{H}{C_w \hat{U}}, \; T_I = \frac{H}{C_w U} \tag{13}$$

where $\hat{U}$ is a fixed scaling speed to determine the linear drag coefficient. This means that in the quadratic case the response time becomes larger than in the linear case at very high frequencies resulting in the weaker fall of the velocity spectrum. The research basin, Bay of Bothnia is weakly stratified in winter, it is shallow (mean depth is 40 m), and its size 100 km × 250 km. Transverse and longitudinal shallow water waves are observed there, providing sources to force very high frequency oscillations in ice velocity; the existence of Kelvin and Poincaré waves has been hypothesized but not proved.

The band spectral power weakening is, however, rather narrow for the range it can be seen, and for frequencies higher than about 2 h^{-1} the spectrum is in the noise and remains unknown. Earlier published ice velocity spectra do not go into the very high frequencies and do not show clear indications of this weakening band. Also it is unclear

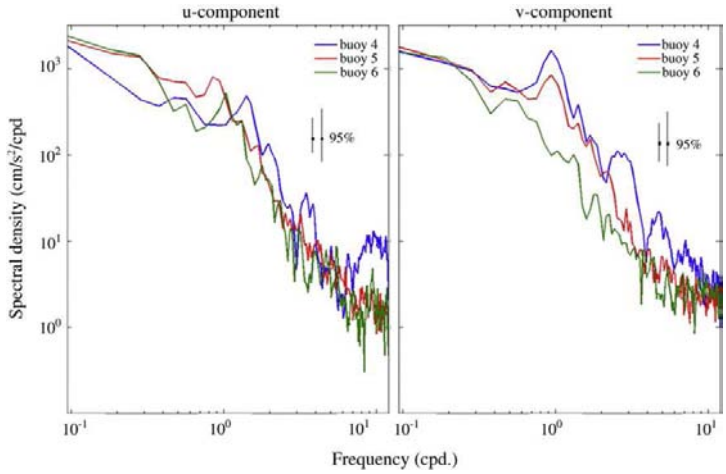

Fig. 6. Ice velocity spectra for three drift buoys from the Sea of Okhotsk, winter 2005: Buoy #4 (blue), Buoy #5 (red) and Buoy #6 (green). Buoy #4 drifted in southeastern Sea of Okhotsk and Buoys #5 and #6 were close to Hokkaido coast. Short error bar is for #4 and #5, longer one for #6. The spectra are above the measurement noise up to about 5 cpd.

whether the present sea ice dynamics theory can explain the phenomenon.

3.4. Lagrangian and Eulerian spectra

The connection of Lagrangian and Eulerian is non-trivial, and in sea ice dynamics there is also a very clear distinction in them due to the finite size of ice floes. Lagrangian dynamics follow a fixed a ice floe, which responds to forcing by its shape and drag properties, while Eulerian dynamics see different ice floes passing fixed points is space. Thus Eulerian ice velocity spectra should contain the variance due to variations in the floe characteristics and therefore should be on a higher level than the Lagrangian spectra. In free drift, the difference in the spectra shows the influence of floe characteristics exactly, but the stronger is the internal stress the more individuality of ice floes is merged into large-scale continuum floe of the ice field.

Most ice kinematics investigations are based in Lagrangian data collected by drifters and alike. Eulerian data have also been analysed (e.g., Schevchenko et al., 2004) but no simultaneous Lagrangian and Eulerian ice velocity analyses are available. The present experimental data from the Sea of Okhotsk provides both Lagrangian and Eulerian velocities in the same region and time (Fig. 7). The drifter moved in the region of the mooring location. This is the first time such simultaneous Lagrangian and Eulerian spectra can be examined in sea ice kinematics. Eulerian spectra are here well above the measurement noise level (about 1 $cm^2\ s^{-1}$/cpd), Lagrangian is good up to the frequency of about 5 cpd.

In the observations, Eulerian spectrum is at higher level than the Lagrangian spectrum as anticipated. The difference does not show significant variations across the spectrum, but the slopes of the spectra show indication to differ at high frequencies. In this case the ice field was not compact and likely not far from free drift, and the difference in the spectra reflects to a large degree the influence of variability of ice floe characteristics. The linear free drift theory presented in Section 2.2 exactly corresponds to Lagrangian dynamics. Its modification into Eulerian dynamics would necessitate a two-dimensional grid with marked ice floes. In simple approach, a random forcing could be added into the free drift equation and that would then raise the Lagrangian spectrum to a higher level.

4. Conclusions

In this work the frequency spectrum of sea ice drift has been examined based on theoretical analysis of the equations of ice dynamics and observations. The observations sites are from the Baltic Sea and Sea of Okhotsk, both in the seasonal sea ice zone. The former basin is shallow and ice drift is mostly wind-driven, while the latter basin is deeper with strong tidal currents. The resulting ice velocity spectra show differences due to external forcing conditions and basin characteristics but also similarities due to invariances in ice–ocean dynamics.

Linear free drift forms the basic theoretical model, coupled with the ocean boundary layer. Ice dynamics modifies the spectrum of forcing, which is due to wind and tidal and geostrophic ocean currents, determined by relaxation time scales of ice and oceanic boundary layer and Coriolis acceleration. The modulation falls asymptotically with frequency in the power of -2 at high frequencies and contains a singularity in the inertial (Coriolis) frequency. Inertia of the ice itself shows up in frequencies higher than about 0.5 cph. Nonlinearities in free drift do not cause significant transfer in the frequency space. Momentum advection is a weak factor, and the quadratic ice–water stress modifies the waveform of a sine wave forcing but does not influence the frequency. Internal stress of drift ice is plastic — strongly nonlinear. The plastic rheology of drift ice is asymmetric in that it gives strong resistance to compression but weak resistance to tension. Convergence and divergence of ice tend to follow the forcing and consequently the internal friction does so, and therefore ice motion inherits the forcing frequency. In spin-up and spin-down of plastic ice drift the situation becomes more complicated.

In the observed spectra the main spectral peak is wide at the synoptic time scales, and toward higher frequencies the spectrum shows red noise with inertial and tidal signals peaking up from it. In the absence of geostrophic currents, wind dominates the ice velocity spectra at frequencies below one cycle per day. At higher frequencies, the tidal and inertial signals are commonly observed. In the red noise band, the slope is close to $-5/3$ from semidiurnal frequency down to 0.5 cph. In very high frequencies, above 0.5 cph there was indication that the power of the in the spectral fall was changed from $-5/3$ to weaker than -1. The reason for this was suggested to be due to nonlinearity of the ice–water interfacial stress, mechanical interactions between ice floes, or shallow water waves in the basin. One case was presented from the Sea of Okhotsk where Eulerian velocities were measured with fixed ADCP mooring and simultaneously Lagrangian measurements were collected with drift buoys in the same region. Eulerian velocity spectrum was above Lagrangian velocity spectrum over all frequencies (0.1–5 cpd). The difference in Lagrangian and Eulerian spectra is well covered by the theory.

The linear free drift theory can explain the observed free drift spectra with their synoptic, inertial and tidal peaks and the power

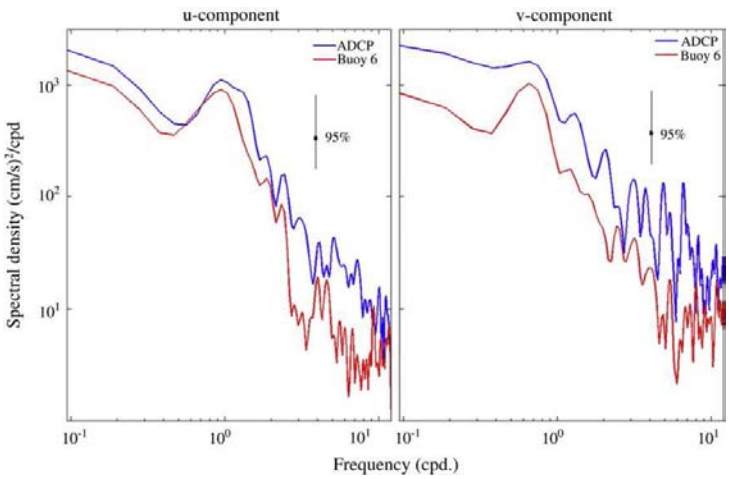

Fig. 7. Eulerian (blue line) and Lagrangian (red line) ice velocity spectra from the Sea of Okhotsk. Eulerian spectrum was obtained from ADCP mooring site and Lagrangian spectrum from a drifter in the region of the mooring site.

law of the spectral density at high frequencies. The very high frequency remains, however, a major problem. Theory suggests that the spectral power law becomes stronger asymptotically but observations indicate that the power becomes weaker at least up to 2 cph. To solve this question needs first of all ice drift velocity observations with very high accuracy (positioning accuracy better than 1 m). When internal stress becomes stronger and stronger, the velocity spectrum goes to zero everywhere as known from observations. Another problem is that how this decrease takes place across the whole spectrum. The existing empirical data does not cover this question well. Understanding the very high frequencies in sea ice dynamics is important in development of short-term forecasting method for ice forces on platforms and ships and for drift and dispersion of oil spills in ice fields.

Acknowledgements

We want to thank Dr. Robert Pritchard for most helpful comments on the manuscript. This work has been financially supported by the Academy of Finland, project *Mesoscale dynamic–thermodynamic modelling of sea ice* (122412).

References

Adams, R.A., 1995. Calculus: a Complete Course, 3rd edn. Addison-Wesley, Don Mills, Ontario.
Agnew, T.A., Le, H., Hirose, T., 1997. Estimation of large scale sea ice motion from SSM/I 85.5 GHz imagery. Annals of Glaciology 25, 305–311.
Andreas, E.L., 1998. The atmospheric boundary layer over polar marine surfaces. The Physics of Ice-covered Seas, Vol. 2. University of Helsinki Press, Helsinki, Finland, pp. 715–773.
Brown, R.A., 1980. Planetary boundary layer modeling for AIDJEX. In: Pritchard, R.S. (Ed.), Proceedings of ICSI/AIDJEX Symposium on Sea Ice Processes and Models. University of Washington, Seattle, pp. 387–401.
Coon, M.D., 1974. Mechanical behaviour of compacted Arctic ice floes. Journal of Petroleum Technology 257, 466–479.
Coon, M.D., Maykut, G.A., Pritchard, R.S., Rothrock, D.A., Thorndike, A.S., 1974. Modeling the pack ice as an elastic–plastic material. AIDJEX Bulletin 24, 1–105.
Coon, M.D., Knoke, G.S., Echert, D.C., Pritchard, R.S., 1998. The architecture of an anisotropic sea ice mechanics constitutive law. Journal of Geophysical Research 103 (C10), 21,915–21,925.
Doronin, Yu.P., Kheysin, D.Ye., 1975. *Morskoi led* (Sea Ice). . (318 pp.) Gidrometeoizdat, Leningrad. (English transl. 1977 by Amerind, New Delhi).
Ekman, V.W., 1902. Om jordrotationens inverkan på vindströmmar i hafvet. Nyt Magasin för Naturvidenskab B 40, 1.
Geiger, C.A., Perovich, D.K., 2008. Springtime ice motion in the Western Antarctic Peninsula Region (US GLOBEC contribution number 515). Deep-Sea Research II 55, 338–350.
Gill, A.E., 1982. Atmosphere–ocean Dynamics. Academic Press, New York. (662 pp.).
Girard, L., Weiss, J., Molines, J.M., Barnier, B., Bouillon, B., 2009. Evaluation of high-resolution sea ice models on the basis of statistical and scaling properties of Arctic sea ice drift and deformation. Journal of Geophysical Research 114 (C8).
Goldstein, R.V., Osipenko, N.M., Leppäranta, M., 2009. Relaxation scales and the structure of fractures in the dynamics of sea ice. Cold Regions Science and Technology 58, 29–35.
Gonella, J., 1972. A rotary component method for analyzing meteorological and oceanographic vector time series. Deep Sea Research 19, 833–846.
Heil, P., Hibler III, W.D., 2002. Modeling the high-frequency component of Arctic sea ice drift and deformation. Journal of Physical Oceanography 32, 3039–3057.
Hibler III, W.D., 1979. A dynamic–thermodynamic sea ice model. Journal of Physical Oceanography 9, 815–846.
Hibler III, W.D., Weeks, W.F., Kovacs, A., Ackley, S.F., 1974. Differential sea-ice drift. I. Spatial and temporal variations in sea ice deformation. Journal of Glaciology 13 (69), 437–455.
Hunke, E., Dukewicz, J.K., 1997. An elastic–viscous–plastic model for sea ice dynamics. Journal of Physical Oceanography 27, 1849–1867.
Hutchings, J.K., Hibler III, W.D., 2008. Small-scale sea ice deformation in the Beaufort Sea seasonal ice zone. Journal of Geophysical Research 113 (C8).
Jenkins, G.M., Watts, D., 1968. Spectral Analysis and its Applications. Holden-Day, San Fransisco, CA.
Kheysin, D.Ye., 1978. Relationship between mean stresses and local values of internal forces in a drifting ice cover. Oceanology 18 (3), 285–286.
Kwok, R., Curlander, J.C., McConnell, R., Pang, S.S., 1990. An ice-motion tracking system at the Alaska SAR facility. IEEE Journal of Oceanic Engineering 15 (1), 44–54.
Laikhtman, D.L., 1958. O vetrovom dreife ledjanykh poley [On the wind drift of polar ice]. Trudy Leningradskiy Gidrometeorologicheskiy Institut 7, 129–137.
Leppäranta, M., 1981. On the structure and mechanics of pack ice in the Bothnian Bay. Finnish Marine Research 248, 3–86.
Leppäranta, M., 2011. The Drift of Sea Ice, 2nd edition. Springer-Praxis, Heidelberg, Germany. (350 pp.).
Leppäranta, M., Hibler III, W.D., 1985. The role of plastic ice interaction in marginal ice zone dynamics. Journal of Geophysical Research 90 (C6), 11899–11909.
Leppäranta, M., Myrberg, K., 2009. Physical Oceanography of the Baltic Sea. Springer-Praxis, Heidelberg, Germany.
Leppäranta, M., Omstedt, A., 1990. Dynamic coupling of sea ice and water for an ice field with free boundaries. Tellus 42A, 482–495.
Leppäranta, M., Sun, Y., Haapala, J., 1998. Comparisons of sea-ice velocity fields from ERS-1 SAR and a dynamic model. Journal of Glaciology 44 (147), 248–262.
Leppäranta, M., Wang, K., Oikkonen, A., 2009. Modelling studies of the frequency spectrum of sea ice velocity. Proceedings of the 20th International Conference on Port and Ocean Engineering under Arctic Conditions, Paper #8. Luleå University of Technology, Sweden.
MacMahan, J., Brown, J., Thornton, E., 2009. Low-cost handheld global positioning system for measuring surf-zone currents. Journal of Coastal Research 25 (3), 744–754. doi:10.2112/08-1000.1.
Marsan, D., Stern, H., Lindsay, R., Weiss, J., 2004. Scale dependence and localization of the deformation of Arctic Sea Ice. Physical Review Letters 93 (17).
McPhee, M.G., 1978. A simulation of the inertial oscillation in drifting pack ice. Dynamics of Atmospheres and Oceans 2, 107–122.
McPhee, M.G., 1980. An analysis of pack ice drift in summer. In: Pritchard, R.S. (Ed.), Proceedings of ICSI/AIDJEX Symposium on Sea Ice Processes and Models. University of Washington, Seattle, pp. 62–75.
McPhee, M.G., 2008. Air–ice–ocean interaction: turbulent ocean boundary layer exchange processes. Springer, Berlin, Germany.
Nansen, F., 1902. The oceanography of the North Polar Basin. Norwegian North Polar Expedition 1893–1896. Scientific Results (Vol. III, No. 9, pp. 427 pp.). Longman Green & Co., Kristiania, Norway.
Nikiforov, E.G., 1957. Changes in the Compactness of the Ice Cover in Relation to its Dynamics. *Problemy Arktiki* (Vyp. 2). Morskoi Transport Press, Leningrad. (in Russian).
Omstedt, A., Nyberg, L., Leppäranta, M., 1996. The role of ice inertia in ice–ocean dynamics. Tellus 48A, 593–606.
Ono, N., 1978. Inertial period motions of drifting ice. Low Temperature Science A37, 107–113.
Overland, J.E., Walter, B.A., Curtin, T.B., Turet, P., 1995. Hierarchy in sea ice mechanics: a case study from the Beaufort Sea. Journal of Geophysical Research 100 (C3), 4559–4571.
Pritchard, R.S., 1975. An elastic–plastic constitutive law for sea ice. Journal of Applied Mechanics 42E, 379–384.
Rampal, P., Weiss, J., Marsan, D., Bourgoin, M., 2009. Arctic sea ice velocity field: general circulation and turbulent-like fluctuations. Journal of Geophysical Research 114, C10014. doi:10.1029/2008JC005227.
Richter-Menge, J., McNutt, S.L., Overland, J.E., Kwok, R., 2002. Relating arctic pack ice stress and deformation under winter conditions. Journal of Geophysical Research 107 (C10). doi:10.1029/2000JC000477 (SHE 15).
Rossby, C.G., Montgomery, R.G., 1935. Frictional influence in wind and ocean currents. Papers in Physical Oceanography and Meteorology Vol. 3, No. 3, 101 pp. Massachusetts Institute of Technology and Woods Hole Oceanographic Institute, Cambridge, MA.
Sanderson, T.J.O., 1988. Ice Mechanics. Risks to Offshore Structures. (253 pp.) Graham & Trotman, Boston.
Schevchenko, G.V., Rabinovich, A.B., Thomson, R.E., 2004. Sea-ice drift on the northeastern shelf of Sakhalin island. Journal of Physical Oceanography 34, 2470–2491.
Shen, H.H., Hibler III, W.D., Leppäranta, M., 1986. On applying granular flow theory to a deforming broken ice field. Acta Mechanica 63, 143–160.
Shuleikin, V.V., 1938. Drift of ice fields. Doklady Academy of Sciences USSR 19 (8), 589–594.
Stern, H.L., Lindsay, R.W., 2009. Spatial scaling of Arctic sea ice deformation. Journal of Geophysical Research 114 (C10).
Thorndike, A.S., 1986. Kinematics of sea ice. In: Untersteiner, N. (Ed.), Geophysics of Sea Ice. Plenum Press, New York, pp. 489–549.
Thorndike, A.S., Colony, R., 1980. Large-scale ice motion in the Beaufort Sea. In: Pritchard, R.S. (Ed.), Sea Ice Processes and Models. University of Washington Press, Seattle, pp. 249–260.
Thorndike, A.S., Rothrock, D.A., Maykut, G.A., Colony, R., 1975. The thickness distribution of sea ice. Journal of Geophysical Research 80, 4501–4513.
Zubov, N.N., 1945. *L'dy Arktiki* (Arctic Ice). Izdatel'stvo Glavsermorputi, Moscow. (English translation 1963 by US Naval Oceanographic Office and American Meteorological Society, San Diego).

III

Reprtinted, with permission, from
Geophysical Research Letters, 43, 10303-10310
doi:10.1002/2016GL069632

AGU PUBLICATIONS

Geophysical Research Letters

RESEARCH LETTER
10.1002/2016GL069632

Key Points:
- Sea ice deformation is studied in smaller scale than before
- Deformations of relatively thin and warm Baltic Sea ice follow power law scaling but with exponent of greater magnitude than in the Arctic
- We find a connection between air temperature and sea ice deformation

Supporting Information:
- Supporting Information S1

Correspondence to:
A. Oikkonen,
annu.oikkonen@fmi.fi

Citation:
Oikkonen, A., J. Haapala, M. Lensu, and J. Karvonen (2016), Sea ice drift and deformation in the coastal boundary zone, *Geophys. Res. Lett.*, *43*, 10,303–10,310, doi:10.1002/2016GL069632.

Received 18 MAY 2016
Accepted 14 SEP 2016
Accepted article online 19 SEP 2016
Published online 13 OCT 2016

Sea ice drift and deformation in the coastal boundary zone

Annu Oikkonen[1], Jari Haapala[1], Mikko Lensu[1], and Juha Karvonen[1]

[1] Finnish Meteorological Institute, Helsinki, Finland

Abstract Small-scale sea ice deformation was studied in the coastal boundary zone (CBZ). Sequences of coastal radar images from the northern Baltic Sea (13 February to 13 May 2011) were used and trajectories of identifiable objects calculated. Average drift velocities in CBZ are small (<0.01 m/s), and events of high drift speeds are short and local. Deformations follow power law scaling but with an exponent of greater magnitude than in the Arctic. We discovered a connection between air temperature and sea ice deformation on a short time scale. During warm days, the mean deformation rate was significantly higher in all length scales than during cold days. This cannot be explained by changes in ice thickness or concentration, which suggests that the ice pack strength responds to air temperature faster than previously assumed. However, we cannot quantify how much this response is enhanced by lower ice thickness compared to the Arctic.

1. Introduction

Sea ice deformation has been studied with respect to length and time scales, and the deformation process has been shown to be intermittent and local [*Marsan et al.*, 2004; *Rampal et al.*, 2008]. Most of the research on sea ice deformation has been based on drifting buoy data [*Rampal et al.*, 2008; *Hutchings et al.*, 2012] or satellite-derived RADARSAT Geophysical Processor System (RGPS) data [*Kwok*, 2006; *Stern and Lindsay*, 2009], covering length scales from approximately 10 km to 1000 km. A deficiency of the synthetic aperture radar-derived ice motion fields is the rather long interval between two images, which is seldom less than a day.

Regionally, previous studies on sea ice deformation mostly cover central pack ice or the marginal ice zone. In addition to these sea ice regimes, the coastal region represents an area of large sea ice deformation. Research on ice dynamics in coastal region has mostly focused on the occurrence of coastal leads and polynyas [*Pärn and Haapala*, 2011], on ice production and water mass formation in polynyas [*Cavalier and Martin*, 1994; *Krumpen et al.*, 2011; *Tamura and Ohshima*, 2011], and on the stability of fast ice [*Mahoney et al.*, 2007]. A coastal ice regime is usually considered to include fast ice and shear zone. Outside the shear zone, ice velocity does not have any persistent gradient in the cross-shore direction. However, for some distance further off the coast the ice drift is still affected by the vicinity of the shore, and we demonstrate that this can be seen as an anisotropy of ice drift. We define the entire region that is affected by the coast as the coastal boundary zone (CBZ).

In order to obtain local ice kinematics at a high temporal and spatial resolution, we utilized coastal radar data from the seasonally ice-covered Baltic Sea. We formed trajectories by tracking individual objects from a sequence of coastal radar images. Methodologically, our approach is similar to previous contributions based on buoy data, but the high temporal resolution of the coastal radar data and the subpixel scale tracking method allow us to study deformations at smaller scale than has previously been possible.

The majority of research on sea ice deformation is based on data from the Arctic, with some data from the Antarctic as well. Only few studies have consider the ice deformation in other areas. However, a study on a seasonal ice zone like the Baltic Sea should serve as an interesting example of the dynamic processes of thinner ice in warmer air temperatures. Numerous studies have shown the increase in air temperature [*Bekryaev et al.*, 2010; *Serreze et al.*, 2009] as well as the decline of ice thickness [*Kwok and Rothrock*, 2009; *Renner et al.*, 2014] and sea ice age [*Comiso*, 2012] in the Arctic. Consequently, the mean drift speed has shown an increase [*Rampal et al.*, 2009; *Spreen et al.*, 2008].

In this paper, we focus on two things: the characteristics of ice drift within the CBZ and the small scale deformation of the drifting ice pack. Neither of these topics has been studied in such a detailed manner before.

Our data set covers a 3 month period from the coldest winter to the ice breakup in spring. Together with weather observations, this allowed us to examine the seasonal and even shorter-term impact of the weather conditions.

2. Data

The Finnish Meteorological Institute (FMI) has instrumented three coastal radars along the Baltic Sea coast for sea ice monitoring. The echoes from the sea ice features, which normally are treated as noise in marine applications, are digitized in high resolution. The radar system and the data collection and transmission process are described in *Karvonen* [2016].

Here we use the data from the radar station on Tankar island (63.95°N, 22.84°E, Figure S1 in the supporting information). The radar images cover an area of 40 by 40 km at a resolution of 33 m. Trajectories of ice objects are calculated using the virtual buoy (VB) tracking method developed by *Karvonen* [2016]. The tracking algorithm locates objects that can be identified reliably enough and tracks the VBs in the sequence of radar images for as long as possible. The minimum spacing between VBs is approximately 300 m. The VBs are lost when they drift out off the study area or when their detection is no longer reliable enough. Once the number of VBs has dropped below the defined cutoff value, the algorithm locates new VBs and adds them to the old ones. In this way, the number of objects being tracked remains at approximately 150–250. For VB tracking, the optimal time step is 2 min, and we used that always when possible. Time steps varied from 1 to 3 min, apart from a few first days when images were only available every 10 min. The error in the 2 min position in VB tracking, approximately 6 m, is comparable to the GPS position error [*Karvonen*, 2016].

In this study we cover a three month period between 13 February and 13 May 2011, from the cold midwinter to the ice breakup in the spring. During this period interruptions in data collection caused four gaps of 1 to 3 days and one longer break of 12 days in late April and early May.

We used hourly recorded wind and air temperature data from the weather station located on the same island as the radar. Ice thickness in the study region was recorded using an airborne EM instrument during the field campaign 2 to 7 March 2011 (Figures S1 and S3). Due to several ridging events and colder than average temperatures in early winter, the ice was thicker than during a typical winter. In the area of radar images, the mean ice thickness of EM measurements was 1.05 m. Additional information on ice conditions in the region throughout the study season was obtained from ice charts provided by FMI Ice Service.

3. Results

3.1. Spatial Variability of Sea Ice Drift

In order to capture the characteristics of the coastal ice drift, we divided the study region into 2 km wide bands aligned with the coast. Numbering of the bands starts from the shore, so that band 1 covers the area 0–2 km off the coast. We conducted our analyses using alongshore and cross-shore components of ice drift and wind in addition to scalar speeds. All velocities were calculated from 1 h average positions of VBs. The averaging reduced the error significantly. For instance, if 30 VB positions are recorded in 1 h, the error of the hourly average is $1/\sqrt{30} \approx 0.18$ times the error of the 2 min position. The hourly averaging reduces the error in position from 6 m to 1.1 m and the error in velocity from 0.05 m/s to 0.009 m/s.

Figure 1 shows the average scalar speed as well as average magnitude of the alongshore and cross-shore components of ice velocity in the different bands for the entire study season. Seasonal averages of velocity are small, even in the bands farther away from the coast (maximum 0.011 m/s in band 11), but ice drift shows large variability (shown as the upper and lower 2.5 percentile of hourly velocities). On the seasonal scale, the fast ice and drifting ice pack with the shear zone can be easily distinguished in Figure 1. The fast ice was stable and reached band 6 until 21 April, when a longer gap in the data emerged. During the last 2 weeks of the season (30 April to 13 May), the whole ice field was broken up, and no fast ice area existed anymore. The drifting ice pack is defined as the bands >6 until 30 April and as the whole area from that date onward.

Daily velocity averages of the drifting ice pack are shown in Figure 2a. The variation in daily average velocities followed the wind speed only occasionally. Ice concentration in the study area was high (90–100% in ice charts) until the ice breakup, apart from 2 days in March. As a result, the ice drift was far from the free drift speed, which can be approximated roughly as 2% of surface wind speed in the Baltic Sea [*Leppäranta*, 2005].

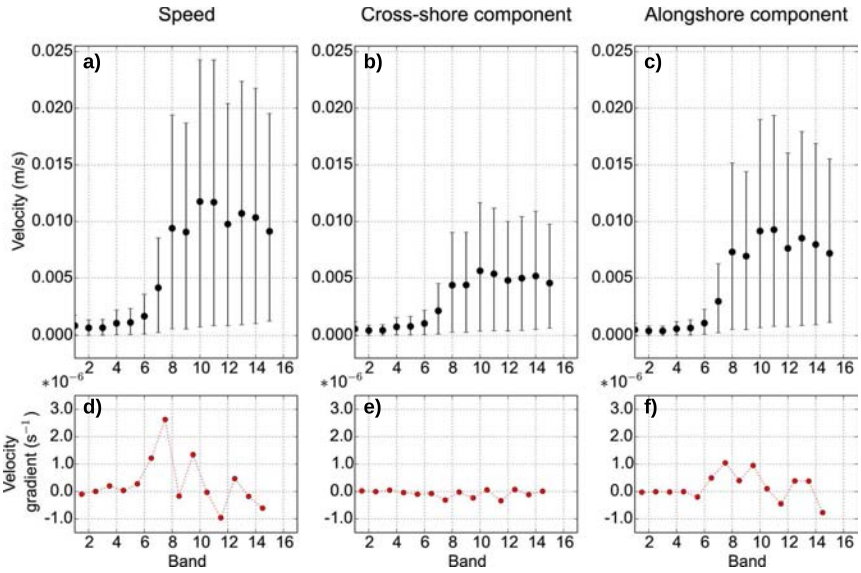

Figure 1. The whole study season average of (a) ice drift speed and of the magnitude of (b) cross shore and (c) alongshore drift component, at different bands. Bars show the range from upper to lower 2.5 percentile of hourly velocities. Seasonal averages of velocity gradients are shown in the lower panel for (d) scalar drift speed and for (e) cross shore and (f) alongshore drift. Velocity gradients are calculated hourly as the difference between mean velocity of neighboring bands divided by the width of the bands.

In general, the drift was anisotropic and the average magnitude of alongshore drift was nearly double compared to cross-shore drift. This anisotropy was clear in the shear zone, where alongshore drift speed increased faster than the cross-shore speed, but it was nearly equally strong still in the outermost bands (Figure 1). The ice response to wind differed componentwise. Drift to wind ratio (wind factor) was 1.9×10^{-3} in the cross shore and 3.4×10^{-3} in the alongshore direction. Thus, the anisotropy was not wind induced; rather, it resulted from the impact of the coast and is a characteristic of the CBZ.

During the whole study season there were only 8 days when the average drift speed in some of the bands exceeded 0.05 m/s, and the maximum daily average was 0.12 m/s. However, the study season included several events when the ice pack was drifting at a much higher velocity. These events were local and short, and they only become visible in the hourly time series. The maximum hourly velocity average of a 2 km band is 0.34 m/s (band 8). As an example, Figure 2b shows a 36 h time series (13 to 14 March) of ice drift speed in different bands. Starting at band 7, the drift speed increased as the distance from the shore increased. In some bands, the drift speed briefly almost reached the free drift estimate. Although the ice concentration was high on the scales of the radar image and the whole basin, concentration in a 2 km wide band can be temporarily clearly lower. This reflects the intermittent and local nature of deformation.

3.2. Deformations of a Drifting Ice Pack

Deformations were calculated for the drifting ice pack. For the deformation analyses, we formed triangles from VBs using Delaunay triangulation. Since the lifespan of VBs varies, depending mostly on ice drift in the area of the radar image, we formed a new set of triangles at the beginning of each day. In order to study the length scale dependency, Delaunay triangulation was applied using six different size ranges of triangles. These groups of triangles of different size were followed for 24 h, until the triangulation was reset at the beginning of the following day. By daily resetting the triangulation, we maximized the number of triangles throughout the season. We applied shape criteria to the triangles in order to avoid erroneous high deformation values caused by distorted cells. The minimum angle of a triangle corner included in the analyses was 15°.

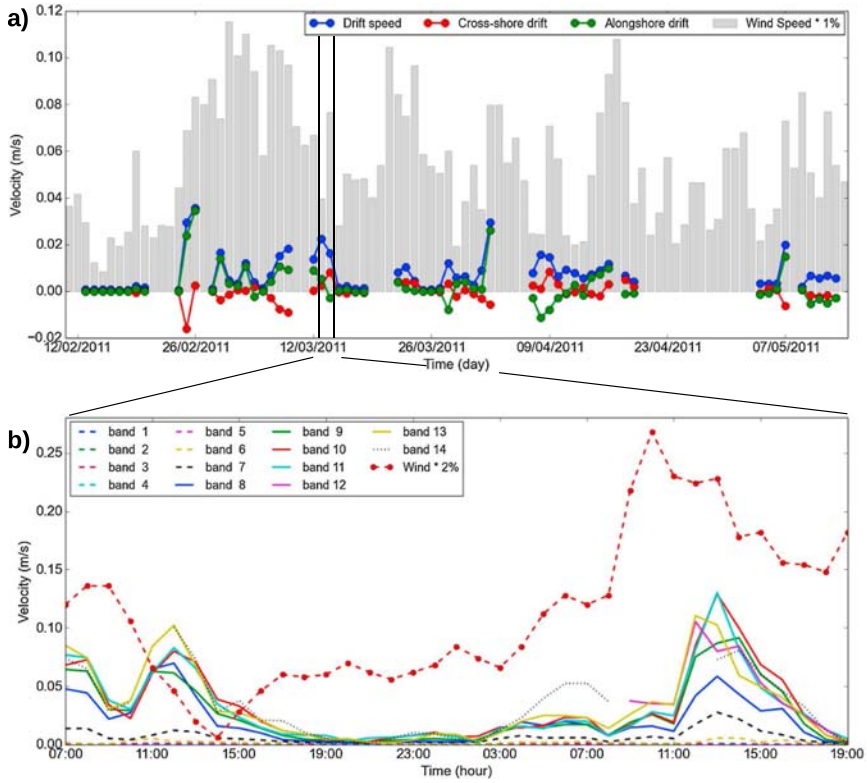

Figure 2. (a) Daily average of drift speed (blue) and its cross shore (red) and alongshore (green) components of a drifting ice pack. The positive direction of the cross shore and alongshore components is toward the coast and up in rotated images (toward 50°), respectively. Grey bars show 1% of wind speed. (b) Sea ice drift speed at different bands during a 36 h period (13 to 14 March). The red line with markers shows 2% of wind speed as an estimate of free drift speed.

The shear, divergence, and total deformation are defined following *Kwok et al.* [2008] and *Bouillon and Rampal* [2015a]:

$$\epsilon_{\text{shear}} = \sqrt{\left(u_x - v_y\right)^2 + \left(u_y + v_x\right)^2} \tag{1}$$

$$\epsilon_{\text{div}} = u_x + v_y, \tag{2}$$

$$\epsilon_{\text{total}} = \sqrt{\epsilon_{\text{shear}}^2 + \epsilon_{\text{div}}^2}, \tag{3}$$

where u_x, u_y, v_x, and v_y are the spatial derivatives of the displacement. u_x is approximated as

$$u_x = \frac{1}{A}\sum_{i=1}^{n}\left(u_{i+1} + u_i\right)\left(y_{i+1} - y_i\right), \tag{4}$$

where A is the area of triangle, i is the index of a corner of triangle, $n = 3$ and $n+1 = 1$. A similar approximation is applied to other derivatives.

Deformation depends on the distances of the corner points of triangles (at time t), their velocities (calculated from their positions at the times t and $t - 1$), and the area of the triangle (at time t). This means that each deformation value is a product of two consecutive time instants only, and it does not have history. Therefore, resetting the triangulation process does not affect the reliability of calculated deformations. The error estimate of deformation is presented in Text S1.

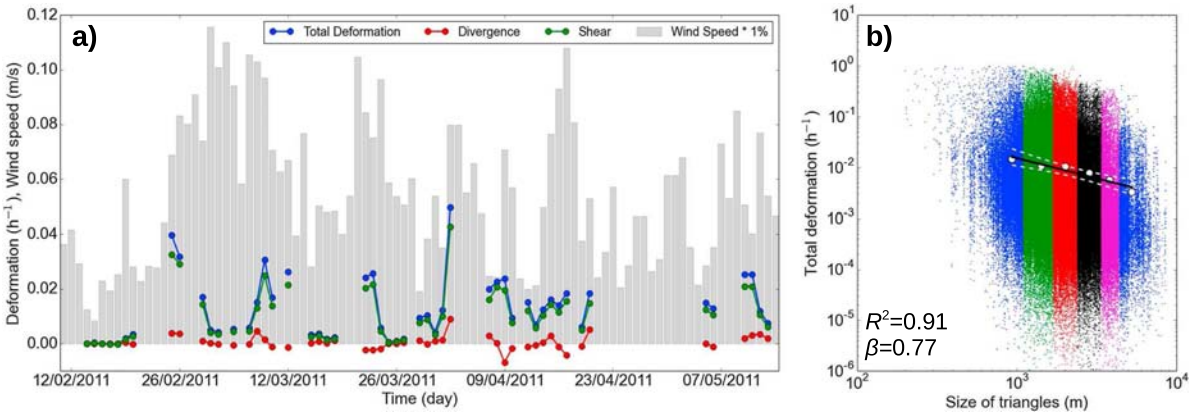

Figure 3. (a) Daily average of total deformation (blue), divergence (red), and shear (green). Grey bars show 1% of the wind speed. (b) The total deformation of different-sized triangles. Deformations are calculated with a 1 h time step. Different triangle size groups are presented with different colors, and white circles denote the averages of the groups. Black line is the least squares fit of the average deformations in log-log space, and dashed white lines show the 95% confidence interval. The fit has a gradient of −0.77 and the square correlation $R^2 = 0.91$.

Figure 3a shows the daily average of divergence, shear, and total deformation. Shear was considerably higher than divergence during the whole study season. On average, shear accounted for 74% of the total deformation. Shear has also been found to be larger than divergence in Arctic studies [*Stern and Moritz*, 2002], but in CBZ the vicinity of the coast and the dominance of alongshore drift most likely amplify the difference. Deformations showed significant day to day variation, which did not directly follow the variation in wind speed.

Figure 3b shows the deformations of different-sized triangles with a 1 h time step during the whole study season. The deformations ϵ follow the power law $\epsilon \sim L^{-\beta}$, where L is the length scale. The exponent β is obtained from a least squares fit of average deformations of different-sized triangles. For the whole study season, we obtained an exponent of 0.77. The uncertainty was estimated using the bootstrap method (10,000 repetitions), which gave an error of 0.02, determined as standard deviation of β. The deformation rates and power law scaling presented here cannot be directly compared to the results from studies on the Arctic or Antarctic, since our data represent CBZ and examine deformations on much smaller scales than did previous studies. Our largest triangles are comparable to the smallest ones in works by, e.g., *Hutchings et al.* [2012], *Marsan et al.* [2004], and *Stern and Lindsay* [2009].

However, we can put our results in the context of the results from different areas and conditions. The mean deformation rate of the largest triangles (0.13 day^{-1}, black in Figure 3b) is comparable to the deformation rate reported from a buoy experiment on Antarctic sea ice [*Hutchings et al.*, 2012] for a similar length scale. In the Arctic, the mean deformation rates for the smallest length scales (∼10 km) are generally smaller by a factor of 10, but they show both seasonal and regional variation. *Herman and Glowacki* [2012] found a minimum in the deformation rate in March, coinciding with the maximum ice thickness and extent. The deformation rates were generally higher at the beginning of the season, when ice thickness was lower, and again from April onward, after the melt season had started.

$\beta = 0.77$ is clearly of greater magnitude than shown in any of the studies on the Arctic [*Marsan et al.*, 2004; *Stern and Lindsay*, 2009], or Antarctic [*Hutchings et al.*, 2012], in which the deformation was calculated from strain rate tensor. In these previous studies, β was found to be in the range of 0.15 to 0.45. β has been shown to be larger in summertime than in wintertime [*Marsan et al.*, 2004] and in areas with a low multi year ice (MYI) fraction [*Stern and Lindsay*, 2009]. *Rampal et al.* [2008] calculated β from buoy dispersions instead of using a strain rate tensor, and they found β to be greater in the case of small length scales (<10 km). In our case, the ice was thin and the air temperature high compared with the Arctic, and β was calculated from smaller length scales. Therefore, we can conclude that the high value of β does not contradict the findings of previous studies.

3.3. Thermodynamic Effect on Sea Ice Deformations

Finally, we examined the effect of weather conditions on sea ice deformation. We test the impact of three different factors on the total deformation. These factors were scalar wind speed, cross-shore wind, and air temperature. The impact of wind speed is assumed to be significant, especially in a wind driven system like the Baltic Sea. However, this has not been quantified before. In CBZ the vicinity of the coast makes the drift system anisotropic, and therefore, we wanted to test how the direction of cross-shore wind affects. Ice dynamics and thermodynamics are coupled. Thermodynamics affects as changes of the ice thickness. Also, air temperature has a twofold impact on strength. First, ice mechanical strength decreases as the temperature of ice increases, which has been seen as an explanation for the different characteristics of winter and summer pack ice [e.g., *Kwok*, 2006; *Stern and Lindsay*, 2009]. Second, temperature impacts the overall ice pack strength as refreezing of leads and recovery of fractures depend on temperature. Recently in sea ice modeling, *Bouillon and Rampal* [2015b] introduced the term "healing" to describe this temperature-dependent factor, which determines the recovery of strength after damage. They supposed that healing is negligible on the time scale of a few days. Thus, these thermodynamic factors have been assumed to impact significantly on fairly long time scales (from weekly to seasonal). We looked for a more instantaneous thermodynamic impact. For each of the three factors studied, we applied some additional criteria in order to minimize the effect of other factors. The end of the season, when the ice concentration was low (from 30 April onward), was excluded from these analyses.

Sensitivity of deformations to weather conditions is shown in Figure 4. Higher wind speeds showed higher deformation rates, as expected (Figure 4c). There is no significant difference in length scale dependency ($\beta = 0.80$ and $\beta = 0.81$). The size group mean deformation rates deviate notably from the least squares fit in the cases of wind speed >7 m/s. In this pair of comparisons, we included only the cases when air temperature is in the range −8°C to 0°C, and the average temperature was very similar in both data groups, −2.2°C and −2.0°C. The corresponding distributions of temperature are presented in Figure S4.

The direction of cross-shore wind did not affect the mean deformation rate (Figure 4f). However, cross-shore wind directed off the coast led to higher β (0.79 with <0 m/s) than cross-shore wind directed toward the coast (0.72 with >0 m/s). Also the bootstrap method yielded to mean difference in β of 0.07. In over 80% of repetitions, the difference was larger than 0.04, which was the standard deviation of β in both opposing cases (Table S1). The greater magnitude of β indicates that internal stress is transmitted over shorter distances when the wind is directed off the shore, presumably as a consequence of lead opening. In this pair, the cases of strong alongshore wind were excluded, and the cases were limited to air temperature in the range of −8°C to 0°C.

The impact of air temperature on the deformation rate (Figure 4i) was comparable to the impact of wind speed (Figure 4c). During warm days, the deformation rate was higher on all length scales. The difference in every size group was greater than 50% in all bootstrap repetitions, while the uncertainty of the size group averages ranged from 1% to 4% of the mean deformation rates. In Figure 4, β was also of greater magnitude during warm days (0.92) than cold days (0.87). The bootstrap method gave the same mean difference for β. However, this difference is of the same magnitude than the error of corresponding values of β (Table S1) and cannot be regarded as significant. In this pair, only the cases with wind speed in the range 5 to 10 m/s were included, and the average wind speed was similar of both cold and warm cases, 7.1 and 7.4 m/s, respectively. Distribution of wind speed and wind components during the cold and warm days are shown in Figures S5 and S6. The data in this comparison are from 13 February to 20 April; during this time the air temperature altered between cold and warm periods of a few days until 31 March, when the warm spring began (Figure S2). Data in Figure 4h primarily represent the warm days that occurred in between the colder periods. Therefore, this comparison does not show seasonal behavior but rather a more immediate impact of air temperature. Limiting the comparison to the period before 31 March led to a similar result (not shown in Figure 4).

In previous studies, the seasonal maximum of deformation rate and β in the summer has been assumed to result from lower ice concentration, thickness and strength, and a less stable atmospheric boundary layer during warm summer [*Stern and Lindsay*, 2009; *Kwok*, 2006; *Herman and Glowacki*, 2012]. We discovered a significant increase in the mean deformation rate on warm days, and β indicated a possible increase as well. However, these cannot be explained by a change in ice concentration or thickness, since the results do not represent different seasons, but alternating individual cold and warm days. Therefore, we assume that the effect of air temperature is related to a decrease in the ice pack strength, as a result of a weaker healing process

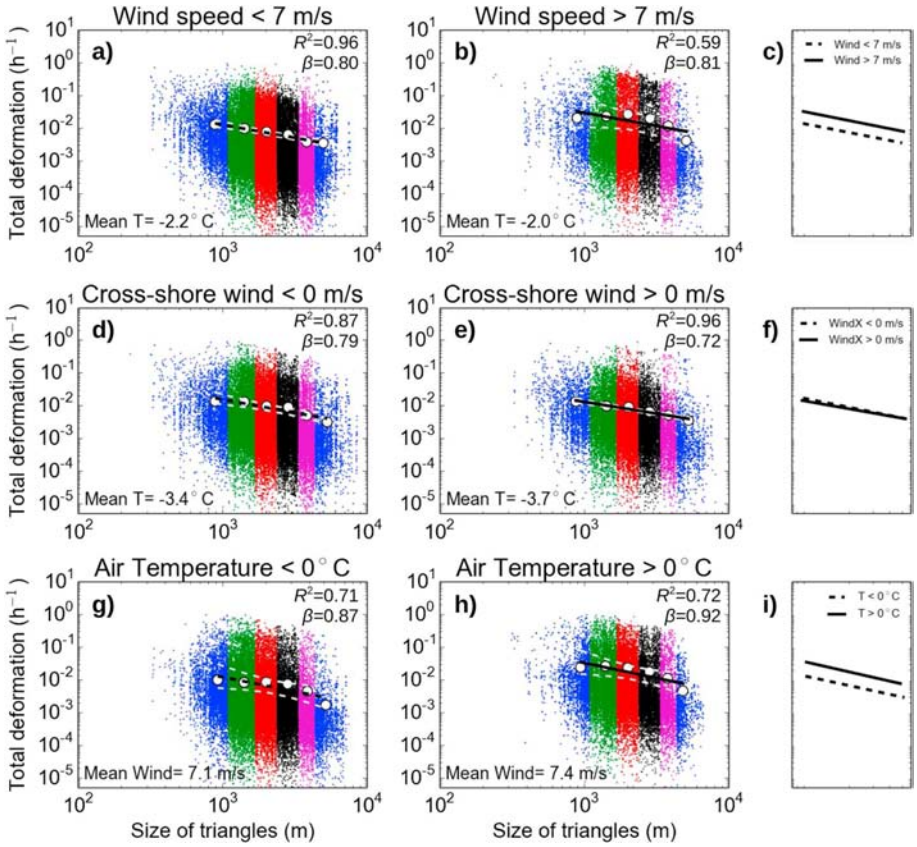

Figure 4. The total deformation of different-sized triangles under different weather conditions. The impact of weather conditions is shown by three pairs of comparisons: (a) wind speed <7 m/s versus (b) wind speed >7 m/s, cross-shore wind directed (d) off the coast versus (e) toward the coast, and air temperature (g) $T < 0$°C versus (h) $T > 0$°C. Deformations and power law scaling is calculated as in Figure 3b. The 95% confidence interval of the fit is shown with white dashed line. The fitted lines of each pair are compared in Figures 4c, 4f, and 4i. For each of three pairs we have applied additional criteria to ensure that they are comparable. In Figures 4a and 4b and 4d and 4e, only the cases with air temperature −8°C to 0°C are included. Mean temperature of included cases is shown in each figure. In Figure 4d and 4e, also the events of strong alongshore wind (>8 m/s) have been excluded. In Figures 4g and 4h, only the cases with wind speed 5 to 10 m/s have been included, and the average wind speeds are shown.

on warm days, but with a clearly shorter response time than estimated by *Bouillon and Rampal* [2015b]. This quick response may be related to low ice thickness and small floe size, compared to the Arctic.

4. Conclusions

The examination of ice drift in CBZ on a small scale revealed an alternating pattern of stationary situations and local events of high drift speed. The response of ice pack to wind forcing shows strong variation. This reflects variation in the internal stress, since the sea ice momentum equation in the Baltic Sea is dominated by wind stress and internal stress [*Leppäranta et al.*, 2001]. During a compressive situation, the internal stress in CBZ becomes so high that it largely prevents ice motion. On the other hand, the opening of a lead releases the internal stress quickly, and ice velocity can reach high values locally and temporarily.

With the coastal radar data we can study the deformation at small length scales (~0.1 to 10 km). The largest length scales in our study are comparable to the smallest ones in studies based on buoy and RGPS data. We found somewhat higher average deformation rates than have been observed in the Arctic. Also, we discovered stronger dependence on length scale, i.e., greater magnitude of β. Partly, this difference can be a characteristic

of CBZ, where shear is generally high. Also, the relatively low ice thickness and small floe size of the Baltic Sea ice have an effect. We also found a temperature dependence in the deformations. During warm days deformation rates were significantly higher. Our results suggest that a change in air temperature has a faster impact on deformation than has previously been assumed. However, we cannot quantify how much this response is enhanced by lower ice thickness compared to the Arctic.

Acknowledgments
We want to thank the Editor and the reviewers, whose constructive comments helped to improve this manuscript. The coastal radar and weather data used in this study are available by contacting FMI Marine Research Unit. We want to acknowledge Image Soft and especially Ari Niemi for the radar server development. This work was funded by Academy of Finland project 279310.

References

Bekryaev, R. V., I. V. Polyakov, and V. A. Alexeev (2010), Role of polar amplification in long-term surface air temperature variations and modern Arctic warming, *J. Clim.*, *23*, 3888–3906, doi:10.1175/2010JCLI3297.1.

Bouillon, S., and P. Rampal (2015a), On producing sea ice deformation data sets from SAR-derived sea ice motion, *Cryosphere*, *9*, 663–673, doi:10.5194/tc-9-663-2015.

Bouillon, S., and P. Rampal (2015b), Presentation of the dynamical core of neXtSIM, a new sea ice model, *Ocean Model.*, *91*, 23–37, doi:10.1016/j.ocemod.2015.04.005.

Cavalier, D. J., and S. Martin (1994), The contribution of Alaskan, Siberian, and Canadian coastal polynyas to the cold halocline layer of the Arctic Ocean, *J. Geophys. Res.*, *99*(C9), 18343–18362.

Comiso, J. C. (2012), Large decadal decline of the Arctic multiyear ice cover, *J. Clim.*, *25*, 1176–1193, doi:10.1175/JCLI-D-11-00113.1.

Herman, A., and O. Glowacki (2012), Variability of sea ice deformation rates in the Arctic and their relationship with basin-scale wind forcing, *Cryosphere*, *6*, 1553–1559, doi:10.5194/tc-6-1553-2012.

Hutchings, J. K., P. Heil, A. Steer, and D. Hibler (2012), Subsynoptic scale spatial variability of sea ice deformation in the western Weddell Sea during early summer, *J. Geophys. Res.*, *117*, C01002, doi:10.1029/2011JC006961.

Karvonen, J. (2016), Virtual radar ice buoys—A method for measuring fine-scale sea ice drift, *Cryosphere*, *10*, 29–42, doi:10.5194/tc-10-29-2016.

Krumpen, T., et al. (2011), Sea ice production and water mass modification in the eastern Laptev Sea, *J. Geophys. Res.*, *116*, C05014, doi:10.1029/2010JC006545.

Kwok, R. (2006), Contrasts in sea ice deformation and production in the Arctic seasonal and perennial ice zones, *J. Geophys. Res.*, *111*, C11S22, doi:10.1029/2005JC003246.

Kwok, R., and D. A. Rothrock (2009), Decline in Arctic sea ice thickness from submarine and ICESat records: 1958–2008, *Geophys. Res. Lett.*, *36*, L15501, doi:10.1029/2009GL039035.

Kwok, R., E. C. Hunke, W. Maslowski, D. Menemenlis, and J. Zhang (2008), Variability of sea ice simulations assessed with RGPS kinematics, *J. Geophys. Res.*, *113*, C11012, doi:10.1029/2008JC004783.

Leppäranta, M. (2005), *The Drift of Sea Ice*, Praxis Ltd, Chichester, U. K., doi:10.1007/978-3-642-04683-4.

Leppäranta, M., Z. Zhang, J. Haapala, and T. Stipa (2001), Sea ice kinematics measured with GPS drifters, *Ann. Glaciol.*, *33*, 151–156, doi:10.3189/172756401781818789.

Mahoney, A., H. Eicken, and L. Shapiro (2007), How fast is landfast ice? A study of the attachment and detachment of nearshore ice at Barrow, Alaska, *Cold Reg. Sci. Technol.*, *93*(17), 178501, doi:10.1016/j.coldregions.2006.09.005.

Marsan, D., H. Stern, R. Lindsay, and J. Weiss (2004), Scale dependence and localization of the deformation of Arctic sea ice, *Phys. Res. Lett.*, *93*(17), 178501, doi:10.1103/PhysRevLett.93.178501.

Pärn, O., and J. Haapala (2011), Occurrence of synoptic flaw leads of sea ice in the Gulf of Finland, *Boreal Environ. Res.*, *16*, 71–78.

Rampal, P., J. Weiss, and D. Marsan (2009), Positive trend in the mean speed and deformation rate of Arctic sea ice, 1979–2007, *J. Geophys. Res.*, *114*, C05013, doi:10.1029/2008JC005066.

Rampal, P., J. Weiss, D. Marsan, R. Lindsay, and H. Stern (2008), Scaling properties of sea ice deformation from buoy dispersion analysis, *J. Geophys. Res.*, *113*, C03002, doi:10.1029/2007JC004143.

Renner, A. H. H., S. Gerland, C. Haas, G. Spreen, J. F. Beckers, E. Hansen, M. Nicolaus, and H. Goodwin (2014), Evidence of Arctic sea ice thinning from direct observations, *Geophys. Res. Lett.*, *41*, 5029–5036, doi:10.1002/2014GL060369.

Serreze, M. C., A. P. Barret, J. C. Stroeve, D. N. Kindig, and M. M. Holland (2009), The emergence of surface-based Arctic amplification, *Cryosphere*, *3*, 11–19, doi:10.5194/tc-3-11-2009.

Spreen, G., R. Kwok, and D. Menemenlis (2008), Trends in Arctic sea ice drift and role of wind forcing: 1992–2009, *Geophys. Res. Lett.*, *38*, L19501, doi:10.1029/2011GL048970.

Stern, H. L., and R. W. Lindsay (2009), Spatial scaling of Arctic sea ice deformation, *J. Geophys. Res.*, *114*, C10017, doi:10.1029/2009JC005380.

Stern, H. L., and R. E. Moritz (2002), Sea ice kinematics and surface properties from RADARSAT synthetic aperture radar during the SHEBA drift, *J. Geophys. Res.*, *107*(C10), 8028, doi:10.1029/2000JC000472.

Tamura, T., and K. I. Ohshima (2011), Mapping of sea ice production in the Arctic coastal polynyas, *J. Geophys. Res.*, *116*, C07030, doi:10.1029/2010JC006586.

Supporting Information for

"Sea ice drift and deformation in the coastal boundary zone"

Annu Oikkonen,[1] Jari Haapala,[1] Mikko Lensu,[1] Juha Karvonen[1]

[1]Finnish Meteorological Institute, Helsinki, Finland.

Contents

1. Figures S1 to S6
2. Text S1
3. Table S1

Introduction

Figures S1 to S6 provide additional detailed information about study area and weather and sea ice conditions.

In Text S1 and Table S1 we present error analysis of the deformation calculation.

Corresponding author: A. Oikkonen, annu.oikkonen@fmi.fi

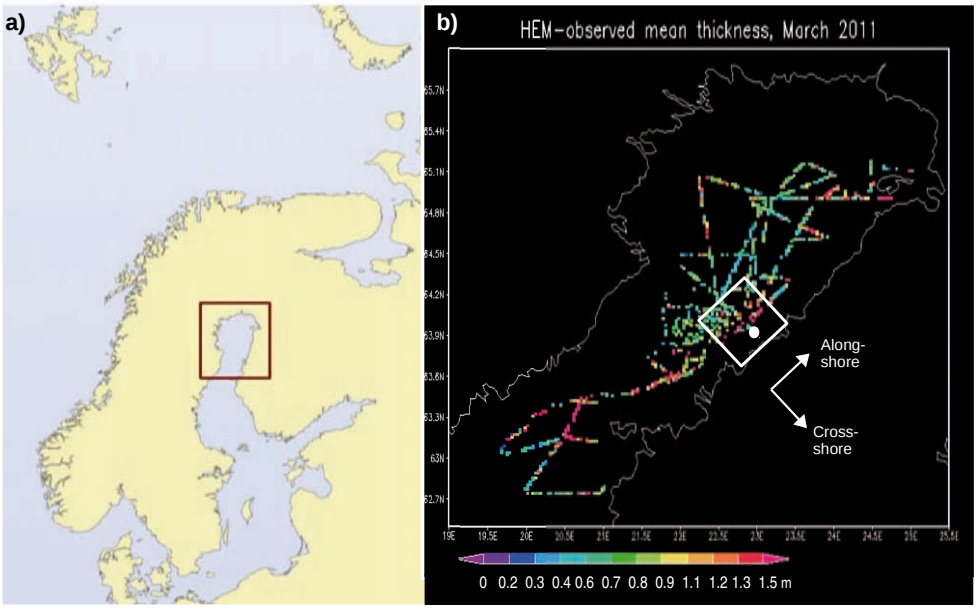

Figure S1. a) Map of the Baltic Sea. Red box is marking the area of the EM-flight map on the right. b) Mean ice thickness obtained from airborne EM measurements 2 to 7 March 2011. White circle shows the location of Tankar island with coastal radar. The area covered by coastal radar images is shown with white box. In the study area the shore line is oriented about 50 degrees clockwise from the North-South direction. For optimal coverage of the drifting ice area, the radar image area has been shifted about 10 km to the west, and the images have been rotated 50° counterclockwise. In this study, the ice drift and wind are divided into cross-shore and alongshore components. Arrows are showing the positive direction of these components.

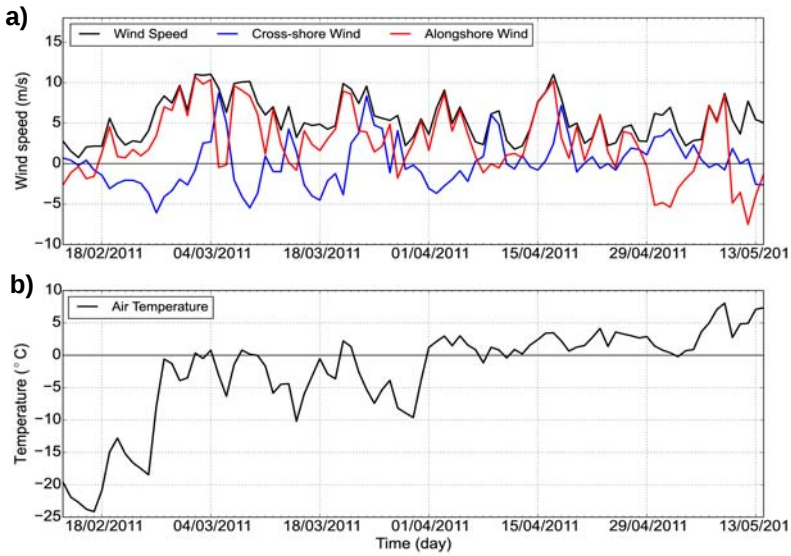

Figure S2. Weather conditions during the study season. a) Daily average of wind speed (black), and its cross-shore (blue) and alongshore (red) component. The positive direction of the components is shown in Figure S1. b) Daily average air temperature.

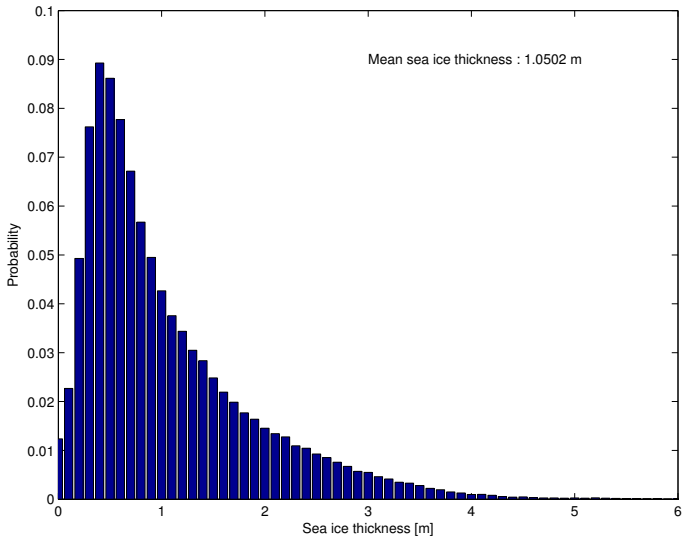

Figure S3. Ice thickness distribution obtained from airborne EM measurements in the Tankar coastal radar coverage area. Values are total thickness including the snow. Snow depth in the area varied from 0 to 50 cm, with the mean depth of 13 cm and standard deviation of 10 cm. (Haas, C. and Casey, A., 2012: Helicopter-borne EM ice thickness surveys during SafeWin 2011 field campaign, report available from the authors)

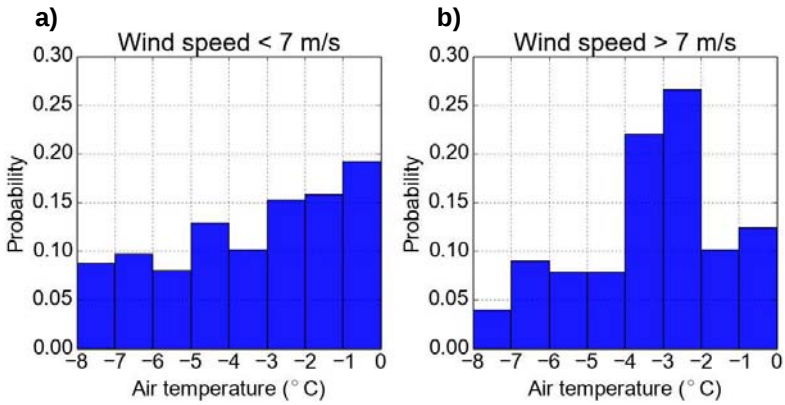

Figure S4. Distribution of air temperature when the wind speed is <7 m/s (a) and >7 m/s (b), i.e. during the cases in the pair of comparison in Figure 4.a and b. In this pair of comparison air temperature is limited to range of -8°C to 0°C. The average air temperature is -2.2°C on the left and -2.0 °C on the right.

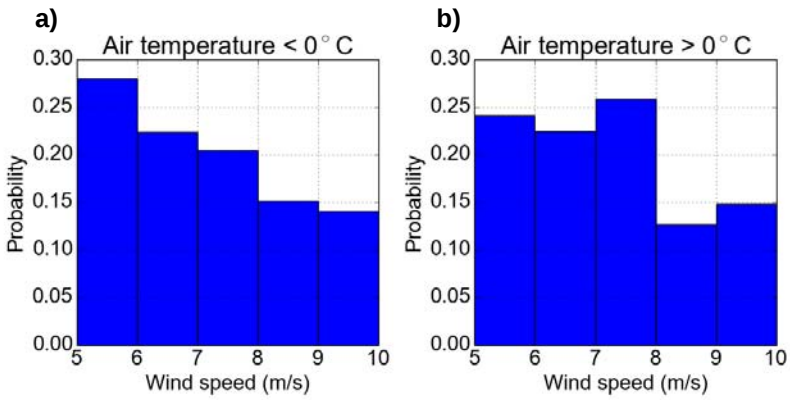

Figure S5. Distribution of wind speed when the air temperature is T<0°C (a) and T>0°C (b), i.e. during the cases in the pair of comparison in Figure 4.e and f. In this pair of comparison wind speed is limited to range of 5 to 10 m/s. The average wind speed is 7.1 m/s on the left and 7.3 m/s on the right.

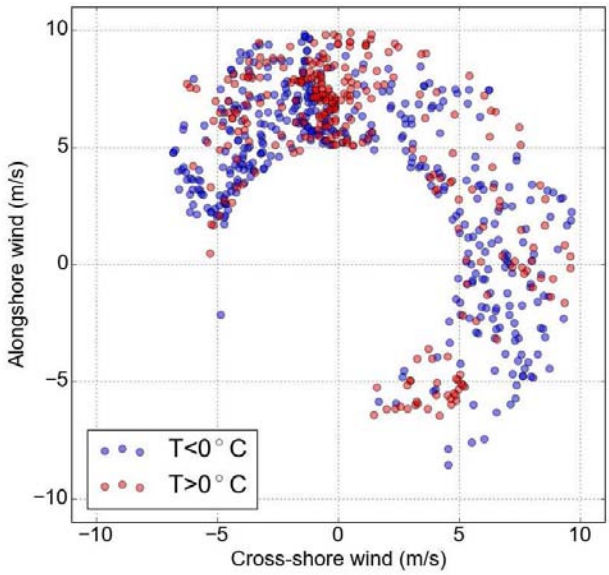

Figure S6. Cross-shore and alongshore wind components during the cold (T<0°C) and warm (T>0°C) cases that have been included in the comparison shown in Figure 4. e-f. The wind speed is limited to range 5 to 10 m/s. The average wind speed is 7.1 m/s during cold days and 7.3 m/s during warm days. The average of absolute values of cross-shore velocities of cold and warm cases are 3.8 and 3.1 m/s, respectively, and the averages of absolute values of alongshore velocities are 5.4 and 5.6 m/s, respectively.

Text S1.

S1.1 Error estimate for deformation

In order to estimate the error of deformation we need to have an estimate of error of the area of triangles, σ_A. This can be calculate as

$$\sigma_A = 2\sqrt{2}N\sqrt{A}\sigma_x \tag{S1}$$

[*Hutchings et al.*, 2012], where A is the area, N is the number of corners in the array ($N = 3$) and σ_x is the error of position. We use hourly averaged positions for the deformation calculations, which reduces the error from the error of 2 minute positions, approximately 6 m, to 1.1 m (for the average of 30 observations). The error of area becomes negligible, when $A >> 8N^2\sigma_x^2$ [*Hutchings et al.*, 2012]. $\sigma_x = 1.1$ m and $N = 3$ give us a lower limit of the area $A >>\sim 100$ m^2 and of the length scale $L >> 10$ m of the triangles, for which we can effectively resolve the deformation. In our analysis, we have included only triangles with $L \geq 200$ m. For the size of our smallest triangles ($L = 200$ m), Equation S1 gives us the noise to signal ratio of $\frac{\sigma_A}{A} = 0.05$.

The strain rate error σ_ϵ can be estimated as

$$\frac{\sigma_\epsilon}{\epsilon} = 2\left(4\frac{\sigma_x^2}{A} + 2\frac{\sigma_x^2}{U^2T^2} + \frac{\sigma_T^2}{T^2} + \frac{\sigma_A^2}{A^2}\right)^{\frac{1}{2}} \tag{S2}$$

[*Hutchings et al.*, 2012], where U is the velocity and T is the time step ($T = 1$ h). The noise to signal ratio is the highest for low drift speed and small triangles. The error in time is negligible. For our smallest triangles ($L = 200$ m) and for $U = 0.01$ m/s, the Equation S2 gives a noise to signal ratio of $\frac{\sigma_\epsilon}{\epsilon} = 0.13$. This ratio drops to $\frac{\sigma_\epsilon}{\epsilon} < 0.1$, when $L > 400$ m (for $U = 0.01$ m/s).

When the triangle size increases, the noise to signal ratio $\frac{\sigma_\epsilon}{\epsilon}$ approaches

$$\frac{\sigma_\epsilon}{\epsilon} = 2\sqrt{2}\frac{\sigma_x}{UT}. \tag{S3}$$

For $U = 0.01$ m/s this gives $\frac{\sigma_\epsilon}{\epsilon} = 0.086$ and this ratio decreases with increasing drift speed.

S1.2 Error estimate for power law scaling

Sea ice deformation follows power law scaling, $D \sim L^{-\beta}$, where L is the length scale. The exponent β is obtained from a least squares fit of average deformations of different-sized triangles, in log-log space.

In the power law scaling we fit a line in the least square sense using the average deformations and length scales of six groups of different-sized triangles. The uncertainty of these size group average deformations is estimated using bootstrap method with $B = 10000$ repetitions. The obtained standard deviation of each size group average deformation is considered as an estimate of error. The largest uncertainty, 4% of the mean deformation, is found for the group of the largest triangles, i.e. for the group with the lowest number of data. For all the other size groups, the uncertainty is in the range of 1% to 2% of the mean deformation.

The overall quality of the least square fit can be evaluated as correlation coefficient R^2

$$R^2 = \frac{\sum_{i=1}^{n}(x_i - \bar{x})(y_i - \bar{y})}{\sum_{i=1}^{n}(x_i - \bar{x})^2 \sum_{i=1}^{n}(y_i - \bar{y})^2} \tag{S4}$$

where $\bar{x}$ and $\bar{y}$ are the averages of x and y, and n is the number of points used for the fit [*Acton*, 2012]. n corresponds to the number of size groups of triangles, i.e $n = 6$. The value of R^2 describes the percentage of the variation that is explained by the least square fit. The values of β and R^2 of the fits presented in Figures 3.b and 4 are listed in Table S1.

The uncertainty of the slope of the fit in power law scaling (β) is estimated with bootstrap method, and the error is defined as the standard deviation of β. The averages and standard deviations of β obtained with $B = 10000$ bootstrap repetitions are listed in Table S1.

Table S1. The power law scaling exponent β and squared correlation coefficient R^2 of the cases presented in Figure 3.b and 4. β is obtained from the least squares fit of average deformations of different-sized triangles, in log-log space. The bootstrap method with 10 000 repetitions is used for estimating the uncertainty of the fit. The mean and standard deviation of β of all bootstrap repetitions are shown for all the cases. The standard deviation of β is considered as an estimate of error.

				Bootstrap (B=10000)	
		β	R^2	**Mean(β)**	**Std(β)**
Whole Season		0.77	0.91	0.77	0.02
Wind Speed	**$<$7 m/s**	0.80	0.96	0.80	0.03
	$>$7 m/s	0.81	0.59	0.80	0.06
Cross-shore	**$<$0 m/s**	0.79	0.87	0.80	0.04
Wind	**$>$0 m/s**	0.72	0.96	0.72	0.04
Air Temperature	**$<$0 °C**	0.87	0.71	0.87	0.05
	$>$0 °C	0.92	0.72	0.92	0.04

References

Hutchings, J. K., P. Heil, A. Steer and D. Hibler (2012), Subsynoptic scale spatial variability of sea ice deformation in the western Weddell Sea during early summer, *J. Geophys. Res.*, *117*, *C01002*.

Acton, F. S. (1966), Analysis of Straight-Line Data, New York: Dover.

IV

Reprtinted, with permission, from
Journal of Geophysical Research (Oceans), 122, 5105-5120
doi:10.1002/2016JC012387

AGU PUBLICATIONS

JGR

Journal of Geophysical Research: Oceans

RESEARCH ARTICLE

10.1002/2016JC012387

Special Section:
Atmosphere-ice-ocean-ecosystem Processes in a Thinner Arctic Sea Ice Regime: the Norwegian Young Sea ICE Cruise 2015 (N-ICE2015)

Small-scale sea ice deformation during N-ICE2015: From compact pack ice to marginal ice zone

Annu Oikkonen[1], Jari Haapala[1], Mikko Lensu[1], Juha Karvonen[1], and Polona Itkin[2]

[1]Finnish Meteorological Institute, Helsinki, Finland, [2]Norwegian Polar Institute, Tromsø, Norway

Abstract We studied small-scale (50 m to 5 km) sea ice deformation from ship radar images recorded during the N-ICE2015 campaign. The campaign consisted of four consecutive drifting ice stations (Floes 1–4) north of Svalbard, with a total duration of nearly 5 months. Deformation was calculated using 5 different time intervals from 10 min to 24 h, and the deformation rate was found to depend strongly on the time scale. Floes 1–3 had a mean deformation rate within the range of 0.06–0.07 h^{-1} with the interval of 10 min, and 0.03–0.04 h^{-1} with the interval of 1 h. Floe 4 represented marginal ice zone (MIZ) with very high deformation rate, 0.14/0.08 h^{-1} with the interval of 10 min/1 h. Deep in the ice pack, high deformation rates occurred only with high wind and drift speed, while in MIZ they were found also during calm conditions. The deformation rates were found to follow power law scaling with respect to length and time scale even on this small scale and in small domain (15 km × 15 km). The length scale dependence of deformation rate depends on the time scale: the power law scaling exponent β of the whole study period decreases from 0.82 to 0.52 with the time interval increasing from 10 min to 24 h. Ship radar images reveal the importance of the deformation history of the ice pack, since the deformation events were initialized along the lines of previous damages.

Key Points:
- Arctic sea ice deformation was studied in smaller scales than before using ship radar images recorded during the N-ICE2015 campaign
- Both the deformation rate and the localization of deformation show strong dependence on time scale
- The deformation history of an ice floe determines its behavior, as deformation events are initialized along the lines of previous damages

Correspondence to:
A. Oikkonen,
annu.oikkonen@fmi.fi

Citation:
Oikkonen, A., J. Haapala, M. Lensu, J. Karvonen, and P. Itkin (2017), Small-scale sea ice deformation during N-ICE2015: From compact pack ice to marginal ice zone, *J. Geophys. Res. Oceans*, *122*, 5105–5120, doi:10.1002/2016JC012387.

Received 30 SEP 2016
Accepted 3 MAY 2017
Accepted article online 9 MAY 2017
Published online 23 JUN 2017

1. Introduction

The response of ice pack to wind and ocean stresses depends strongly on its inherent properties including thickness, concentration, fracturing, floe size and mechanical strength. These properties are variable across the Arctic Ocean, and they also show seasonal variations. Consequently, a wide range of different types of motion are found: from a rigid body motion of thick ice in the central Arctic to a complex system of ice floes in the marginal ice zone (MIZ).

The structure of an ice cover results from the interplay of thermodynamics and dynamics. Thermodynamics changes ice thickness through the ice growth and melt as determined by the heat balance. The heat balance, on the other hand, depends on the ice thickness. The ice thickness also affects the deformation of ice cover under atmospheric and oceanic forcing. Deformation results from dynamically driven differential motion between material ice particles. The term deformation can be used in the context of the horizontal differential motion of the ice pack, which can be determined from buoy arrays or time series of images. The term deformation can also be used for the vertical processes of ridge formation and rafting. Here we use the term in its horizontal reference, where also ridging and rafting are seen only as differential motion.

Horizontal deformation can be associated with concentration changes, including opening of leads as well as ridging and rafting, but pure shear deformation with no concentration change or thickness increase is also possible. However, the presence of deformation requires the presence of fractures, leads or sliplines between the material particles. The opposite does not hold, and a large collections of discrete floes can move as coherent aggregates.

The intensity of deformation increases with the increasing intensity of driving forcing. When an intense phase ends and the heat balance is negative, fractures, leads and sliplines refreeze. *Bouillon and Rampal* [2015b] introduced a term healing to describe this process which is the more effective the lower the temperatures. In general, the smaller components of the ice cover bond into larger entities, and the floe interfaces become difficult to distinguish.

Numerous studies have shown changes in the Arctic sea ice cover: air temperature has been increasing [*Serreze et al*., 2009; *Bekryaev et al*., 2010], and both ice thickness [*Kwok and Rothrock*, 2009; *Renner et al*., 2014] and sea ice age have shown a decrease [*Comiso*, 2012]. As a result, an increase of sea ice drift speed and strain rates has been observed [*Rampal et al*., 2009; *Spreen et al*., 2011]. All these changes suggest more intense deformations in the future.

In this study we calculated sea ice deformations from the ship radar images recorded on board R/V Lance during the N-ICE2015 campaign [*Haapala et al*., 2017]. Ship radar images cover an area of 15 km ×15 km with a very high temporal (1 min) and spatial resolution (12.5 m). Differential ice motion was obtained by calculating the trajectories of individual, identifiable objects from a sequence of the ship radar images. High temporal resolution and the subpixel scale tracking method [*Karvonen*, 2016] allowed us to study deformations on much smaller length scale (∼50 m to 5 km) and time scale (10 min to 24 h) than has been possible in previous studies on Arctic sea ice deformations. They are mainly based on buoy data with a temporal scale of ∼1 h [*Rampal et al*., 2008; *Hutchings et al*., 2011] or satellite-derived RADARSAT Geophysical Processor System (RGPS) data with a temporal scale of days [*Kwok*, 1998; *Marsan et al*., 2004; *Stern and Lindsay*, 2009] covering the spatial scales of approximately 10 km to 1000 km.

During the N-ICE2015 campaign, sea ice north of Svalbard was studied in 4 drifting ice stations that lasted in total nearly 5 months [*Granskog et al*., 2016]. The data cover the period from the coldest winter to summer melt and the regions from the compact pack ice to the MIZ. In this paper, we present sea ice deformations calculated using several time and length scales, and show how the deformation rate depends on them. The intermittent and localized nature of sea ice deformation is examined by determining the impact of the time scale on the length scale dependence, as well as the impact of length scale on the time scale dependence of deformation rate. Also, we examine how the sea ice deformation rate and its length scale dependence is affected by external factors, air temperature and distance to the ice edge.

2. Data

We studied small-scale sea ice deformations using ship radar images collected during the N-ICE2015 campaign that lasted from January to June in 2015. During the campaign, sea ice north of Svalbard was studied in 4 consecutive ice stations, referred as Floes 1–4. All the time related references to Floes refer to the measurement periods of these ice stations, not to the life time of any ice floe. In each Floe, R/V Lance was frozen in and drifting with the surrounding ice pack. The drift tracks of Floes 1–4 are shown in *Granskog et al*. [2016]. The duration of Floes varied from about 10–40 days and in total the data cover nearly 5 months.

The ship radar was instrumented with an independent server for the digitization of radar images. The radar server system and the image processing is described in *Karvonen* [2016]. Temporal median filter (15–20 s) was applied to the raw data, and, in this work, we used these preprocessed images with interval of 1 min. Radar images cover the area of 15 × 15 km with a resolution of 12.5 m. Examples of ship radar images can be seen in Figure 1.

The orientation of the original ship radar images follows the orientation of the ship in such a way that the bow of the ship is always pointing to the left in the image (Figure 1). Since the ship was frozen in the surrounding ice pack, the rotation of the ice pack led to the rotation of the ship and thus to the rotation of the ship radar images. In this study, we are interested in sea ice deformation, defined as shear and divergence, and the total deformation rate as a product of the two. These are determined by the differential velocities of ice objects. Therefore, the correction to compensate the rotation of the images is not necessary, but it is considered as a potential source of additional error. We used the original images without rotation correction.

We calculated the trajectories of ice objects with the virtual buoy (VB) tracking method developed by *Karvonen* [2016]. The algorithm finds objects that can be identified reliably enough. These VBs are followed in the sequence of radar images as long as possible. VBs are lost when they drift out from the study area or when their detection is no longer reliable enough. Once the number of VBs has dropped below the defined cut-off value, the algorithm finds new VBs and adds them to the old ones. As described in *Karvonen* [2016], the uncertainty of the VB position is the smallest when the tracking is done with a short time interval between successive images. For the time interval of 10 min, the error in VB position is approximately 3 m

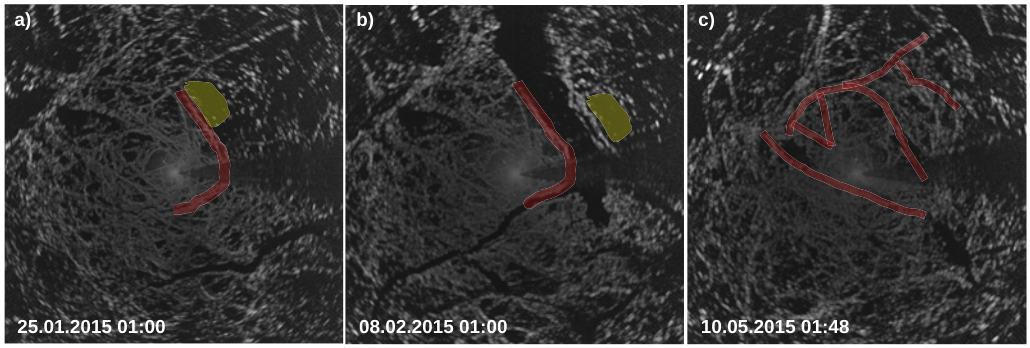

Figure 1. Ship radar image at (a) 25 January 01:00, (b) 8 February 01:00 and (c) 10 May 01:48. Red line in Figures 1a and 1b shows the line of damage, along which the opening of wide lead was initiated on 7 February. For better view of the lead opening, a level ice area that can be clearly identified both in Figures 1a and 1b is marked with yellow patch. Red lines in Figure 1c show the lines of damage that were formed during the deformation period at the beginning of Floe 3 (25–30 April). The breakup of Floe 3 (4 June) occured along the same lines. In all the images, the ship is located in the center. The images have been cropped and cover an area of approximately 9 km ×9 km.

[*Karvonen*, 2016]. For the 1 min time interval used in this study, this error is equal or smaller. There are some short gaps in the obtained time series. They are due to temporary disturbances in the ship radar images, and mainly caused by changes in the radar settings or helicopter flights.

We utilized the wind (at 10 m level) and air temperature (2 m level) measured on a meteorological tower moored on each ice Floe approximately 300–400 m away from the ship [*Hudson et al*., 2015]. During each Floe, ice and snow thickness was measured repeatedly [*Rösel et al*., 2016].

3. Deformation Calculation Method

We calculated deformation rate from 10 min average positions of VBs. We used the Delaunay triangulation method to form triangles from VBs. In order to study the time and length scale dependency of deformation rate, we calculated deformation rate using several time intervals and triangle size groups. The time intervals longer than 10 min (1 h, 3 h, 6 h and 24 h) were obtained as subsampling of the 10 min position time series. Due to the largely varying lifetime of VBs, we formed a new set of triangles at the beginning of each time step. Each time, six different size groups of triangles were formed by setting different minimum distance for the VBs for triangulation. We applied a shape criteria of triangles in order to avoid erroneous high deformation rates caused by distorted cells. The minimum angle of a triangle corner that we include in the analyses is 15°.

The shear, divergence and total deformation rate are defined following *Kwok et al*. [2008] and *Bouillon and Rampal* [2015a]:

$$\epsilon_{shear} = \sqrt{(u_x - v_y)^2 + (u_y + v_x)^2} \tag{1}$$

$$\epsilon_{div} = u_x + v_y, \tag{2}$$

$$\epsilon_{total} = \sqrt{\epsilon_{shear}^2 + \epsilon_{div}^2}, \tag{3}$$

where u_x, u_y, v_x and v_y are the spatial derivates of the displacement. u_x is approximated as

$$u_x = \frac{1}{A}\sum_{i=1}^{n}(u_{i+1} + u_i)(y_{i+1} - y_i), \tag{4}$$

where A is the area of triangle, i is the index of a corner of triangle, $n = 3$ and $n+1 = 1$. Similar approximation is applied to other derivates.

Deformation rate depends on the distances of the corner points of triangles (at the time t), their velocities (calculated from their positions at times t and t−1), and the area of the triangle (at the time t). This means

that each deformation rate value is the product of two consecutive time instants only and does not have a history. Therefore the reset of triangulation does not affect the reliability of the calculated deformation rates.

The uncertainty of calculated deformation rate can be estimated as the propagation of position error. First, we need an estimate of the error of area of triangles, σ_A. This can be calculated as

$$\sigma_A = 2\sqrt{2}N\sqrt{A}\sigma_x \tag{5}$$

[*Hutchings et al*., 2012], where A is the area, N is the number of corners in the array ($N = 3$) and σ_x is the error of position. The error of area becomes negligible, when $A \gg 8N^2\sigma_x^2$ [*Hutchings et al*., 2012].

Deformation rates are calculated from 10 min average positions of VBs. For stationary situation, this averaging reduces the error to $1/\sqrt{10} \approx 0.32$ times the error of 1 min position, i.e., from 3 to 1 m. Since this does not fully aply to averaged position of moving object, we conduct the error analyses for both $\sigma_x = 1$ m and $\sigma_x = 3$ m. For $\sigma_x = 1$ m ($\sigma_x = 3$ m) we get a lower limit of the area $A \gg \sim 70$ m^2 (650 m^2) and of the length scale $L \gg 9$ m (25 m), for which we can effectively resolve the deformation rate. In our analysis, we have included triangles with $L \geq 50$ m. For the size of our smallest triangles ($L = 50$ m), equation (5) gives us the noise to signal ratio of $\frac{\sigma_A}{A} = 0.17$ (0.51), and this ration decreases as A increases.

The strain rate error σ_ϵ can be estimated as

$$\frac{\sigma_\epsilon}{\epsilon} = 2\left(4\frac{\sigma_x^2}{A} + 2\frac{\sigma_x^2}{U^2T^2} + \frac{\sigma_T^2}{T^2} + \frac{\sigma_A^2}{A^2}\right)^{\frac{1}{2}} \tag{6}$$

[*Hutchings et al*., 2012], where U is the velocity and T is the time step (10 min, 1 h, 3 h, 6 h and 24 h). The noise to signal ratio is the highest for low drift speed, small triangles and small time step. The error in time is negligible. For our smallest triangles ($L = 50$ m) and smallest time step (10 min), and for $U = 0.01$ m/s, equation (6) gives a noise to signal ratio of $\frac{\sigma_\epsilon}{\epsilon} = 0.58$ (1.7). This ratio decreases to <0.35 (1.07) as the time steps increases to ≥ 1 h.

When the triangle size increases, the noise to signal ratio $\frac{\sigma_\epsilon}{\epsilon}$ approaches

$$\frac{\sigma_\epsilon}{\epsilon} = 2\sqrt{2}\frac{\sigma_x}{UT}. \tag{7}$$

For $U = 0.01$ m/s this gives $\frac{\sigma_\epsilon}{\epsilon}$ of 0.471, 0.079, 0.026, 0.013 and 0.003 (1.414, 0.236, 0.079, 0.039 and 0.009) for time steps of 10 min, 1 h, 3 h, 6 h, and 24 h, respectively. All the ratios $\frac{\sigma_\epsilon}{\epsilon}$ decrease with increasing drift speed.

Increase in the time interval and drift speed lowers the noise to signal ratio $\frac{\sigma_\epsilon}{\epsilon}$, but the obtained deformation rate field may be a poorer representation of the real situation. This is due to the small areal coverage of the ship radar images. The triangulation can be done only for the VBs that remain identifiable and in the radar range between the two consecutive times considered. During the days when the there is significant deformation near the edge of the radar image, loss of VBs may lead to the incomplete areal coverage of the triangles. This may cause bias in and lower the quality of the deformation fields of the longest time intervals, 6 h and 24 h, on some days.

4. Results

4.1. Deformation Time Series

The hourly time series of the total deformation rate, shear and divergence of Floes 1–4 are shown in Figures 2–5. We show both net divergence (average of the divergence of all triangles) and absolute divergence (average of the absolute divergence value of all triangles). Most of the time, the net divergence is close to zero, as both divergence and convergence occur simultaneously in the area covered by the ship radar images. In contrast to shear and absolute divergence, significant values of net divergence are found only as short peaks. The absolute divergence is clearly higher than the net divergence, but still lower than shear throughout the entire study period. Overall, shear accounts for 73% of the total deformation rate. The dominance of shear is in agreement with previous studies [*Stern and Moritz*, 2002].

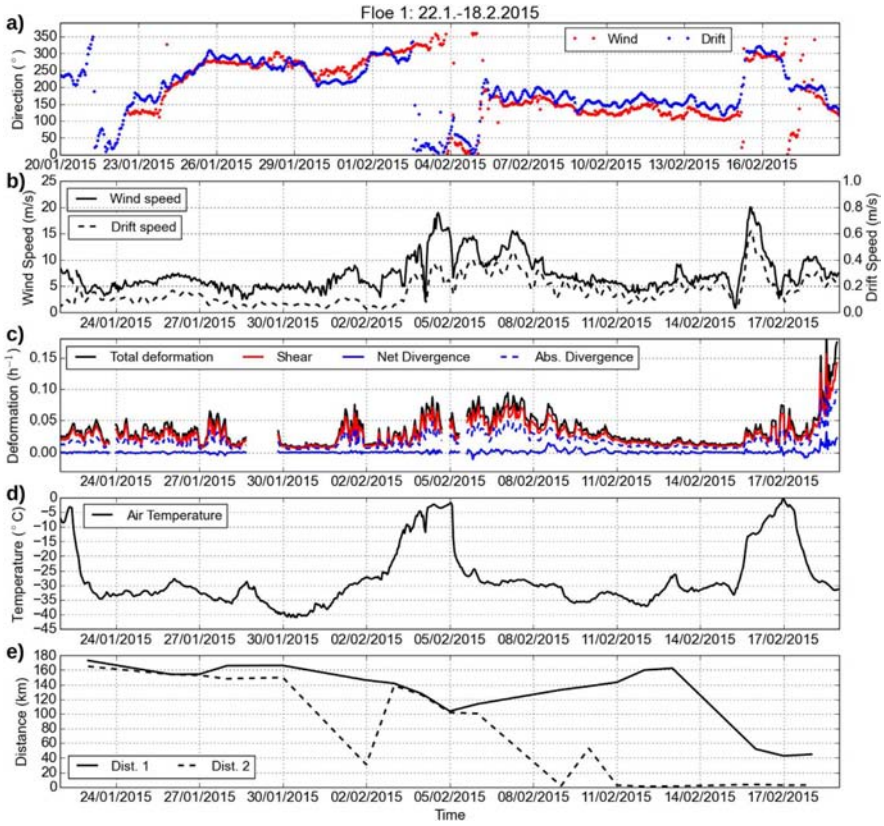

Figure 2. Hourly time series of (a) wind and drift direction, (b) wind and drift speed, (c) deformation rate, (d) air temperature and (e) distance to the ice edge during Floe 1. Wind and drift directions show where the wind and drift vectors are pointing. c shows the total deformation rate, shear, net divergence and absolute divergence. Net divergence is the average of the divergence of all triangles, and absolute divergence is the average of the absolute values of divergence of all triangles. In e, Dist 1 is the distance to the ice edge, and Dist 2 the distance to the nearest area with concentration $<$90%.

Following the storm categorization by *Cohen et al*. [2017], Floe 1 experienced two major storms (wind speed $>$ 8 m/s for a period longer than 3 h together with a air pressure drop of 5 hPa in 6 h). During the first storm, 3–9 February, the deformation rate remained on a high level and followed the variation of wind and drift speed. The change in the wind direction on 6 February did not cause any distinct signal in the deformation rates. However, the wind blowing from north led to a drift toward the ice edge, and divergence on a larger scale, observed by simultaneous buoy array [*Itkin et al*., 2017]. Consequently, in the direction of the drift, ice concentration decreased, and the distance from R/V Lance to the nearest area with the concentration of $<$ 90% started to decrease (Figure 2e). During this phase, one wide lead opened in the ship radar range (Figure 1), with some back and forth motion, resulting in peaks in net divergence on 8–10 February. From 11 to 15 February the deformation rate stayed very low despite of significant drift, most likely due to the looser ice pack.

Another storm arrived on 15 February. During the first 2 days, the deformation rate remained low compared to the wind speed reaching 20 m/s. On 17 February, the deformation rate increased quickly to a very high level. By this time, the wind speed had already decreased to about 10 m/s, and there was no such change in the wind or drift direction that could have explained this strong increase in the deformation rates leading to the breakup of Floe 1. Within approximately 24 h, the entire ice pack in the ship radar range broke into

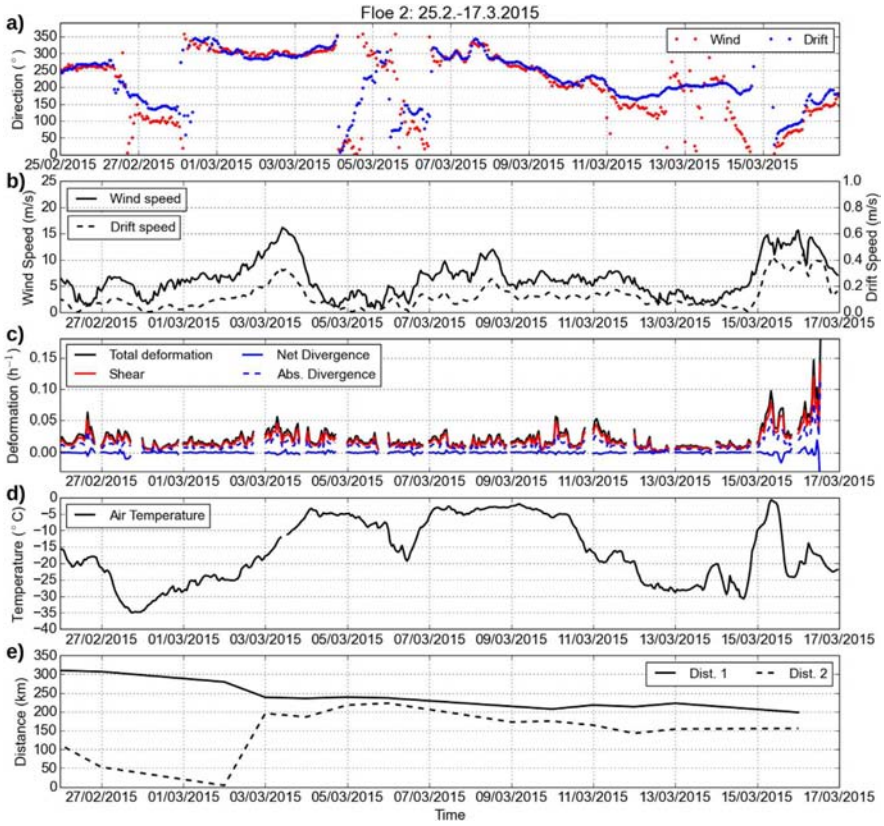

Figure 3. Hourly time series of (a) wind and drift direction, (b) wind and drift speed, (c) deformation rate, (d) air temperature and (e) distance to the ice edge during Floe 2. Wind and drift directions show where the wind and drift vectors are pointing. c shows the total deformation rate, shear, net divergence and absolute divergence. Net divergence is the average of the divergence of all triangles, and absolute divergence is the average of the absolute values of divergence of all triangles. In e, Dist 1 is the distance to the ice edge, and Dist 2 the distance to the nearest area with concentration $<$90%.

small floes and dispersed. This suddenness of the breakup, the resulting small size of floes and the rapidness of dispersion were most likely due to the vicinity of the ice edge, and to the impact of swell.

Previously damaged areas can be seen in the ship radar images as lighter color due to higher surface roughness. These lines of damage (LD) form a dense and complex matrix (Figure 1). All the deformation events were initialized along these already existing lines, and, during intense deformation events, the matrix of the LDs was partly reorganized and new LDs were formed. Previous studies have shown that large scale deformations are concentrated along narrow lines, often referred to as linear kinematic features (LKF). LKFs are large scale features which typically have a spacing of the order of tens of kilometers, remain for a few days and lengthen into the basin-scale [*Hutchings et al.*, 2005]. LDs that we find in ship radar images differ from LKFs by clearly smaller spacing, $\sim$0.1 to 1 km. Also, LKFs are temporal features of a deformation field, while LDs are a property of ice pack, seen in surface roughness, and remain, even when they are not active. the LDs seen in ship radar images remind that all the observed behavior during N-ICE2015 is impacted by the precampaign deformation history of the ice pack.

For Floe 2 (Figure 3), the deformation rate was generally lower than for Floe 1. The mean deformation rate of Floe 2 was 0.059 and 0.026 h^{-1} for 10 min and 1 h time intervals, while during Floe 1 it was 0.073 and 0.036 h^{-1} for 10 min and 1 h time intervals. Floe 2 was located much deeper in the ice pack than Floe 1, and its distance to the ice edge, *l*, remained greater than 200 km. Even the stormy winds from 2 to 3 March

Figure 4. Hourly time series of (a) wind and drift direction, (b) wind and drift speed, (c) deformation rate, (d) air temperature and (e) distance to the ice edge during Floe 3. Wind and drift directions show where the wind and drift vectors are pointing. c shows the total deformation rate, shear, net divergence and absolute divergence. Net divergence is the average of the divergence of all triangles, and absolute divergence is the average of the absolute values of divergence of all triangles. In e, Dist 1 is the distance to the ice edge, and Dist 2 the distance to the nearest area with concentration $<$90%.

caused only a very slight increase in the deformation rates. It was only at the end of the duration of Floe 2, when an intense storm caused heavy deformations in the entire area of the ship radar range. Contrary to the ending of Floe 1, breaking occurred far from open water ($l \approx 200$ km) and the broken ice pack did not disperse.

Floe 3 lasted the longest, 40 days. During this period, intense deformation occurred only during the first few days and at the very end when Floe 3 broke (Figure 4). Between these events, the deformations in the range of the ship radar were largely limited to a lead in the peripheral area of the ship radar images. The lead remained active during most of the duration of Floe 3. Even the peak in the wind speed (15 m/s) and drift speed (0.4 m/s) from 21 to 23 March did not produce any significant signal in the deformation rate. The mean deformation rate of Floe 3 was 0.071 and 0.034 h^{-1} for 10 min and 1 h time intervals.

During the intense deformation at the beginning of Floe 3, the ice field broke into small floes. This occurred along existing LDs. However, the broken ice field in the ship radar range did not disperse. When the wind calmed and the intense deformation period ended by 1 May, the resulting ice field was a new composite of the same ice as before the deformation event. This composition of Floe 3 remained for over 1 month, until the final breakup in the beginning of June. The ship radar images revealed the breakup to be an inverse event of the formation of this composition of Floe 3: the breaking occurred along the lines where smaller floes had been attached together one month earlier (Figure 1c). By the time of the breakup, Floe 3 had

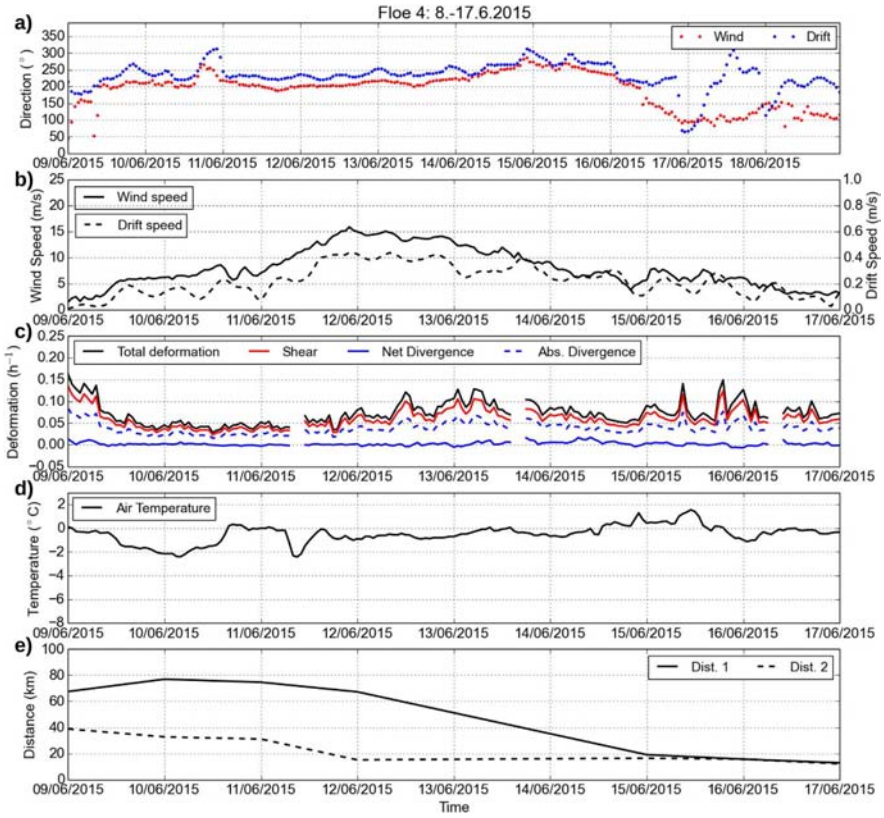

Figure 5. Hourly time series of (a) wind and drift direction, (b) wind and drift speed, (c) deformation rate, (d) air temperature and (e) distance to the ice edge during Floe 4. Wind and drift directions show where the wind and drift vectors are pointing. c shows the total deformation rate, shear, net divergence and absolute divergence. Net divergence is the average of the divergence of all triangles, and absolute divergence is the average of the absolute values of divergence of all triangles. In e, Dist 1 is the distance to the ice edge, and Dist 2 the distance to the nearest area with concentration $<$90%.

drifted very close to the ice edge ($l \approx 40$ km), and contrary to the event at the beginning, the broken ice field dispersed quickly.

Floe 4 represents conditions very different from those of the other Floes: summer ice undergoing intense melting and drifting with a high speed close to the ice edge. During the whole duration of Floe 4, the ship radar showed fast motions in an assembly of floes, and data from Floe 4 clearly represents the MIZ. Consequently, the mean deformation rate was very high: 0.140 and 0.080 h^{-1} for 10 min and 1 h time interval.

Conditions for Floes 1–4 differ from each other, and also varied largely throughout the duration of each Floe. Wind speed and direction, air temperature and the drift of the Floes, varied in the hourly time scale (Figures 2–5). The distance to the ice edge and the sea ice concentration showed variation in the time scale of days. Variation in ice thickness occurred over such a long time scale, that over the duration of each Floe it can be assumed to have negligible effect on deformations. Only Floe 4 experienced intense melting, but the duration of that Floe was also very short. The mean ice thickness in the vicinity of R/V Lance was fairly similar in all the Floes 1–4: 1.5 m, 1.2 m, 1.4 m and 1.4 m, respectively [*Rösel et al.*, 2016]. All these values are clearly lower than the typical thickness of Arctic sea ice examined in most of the previous deformation studies. the ice was also young, mostly FYI and SYI.

The distance to the ice edge (l) at the start point of the drift differed from Floe to Floe, and l also varied, generally decreased throughout the duration of each ice Floe (Figures 2–5). Presumably, this affects the

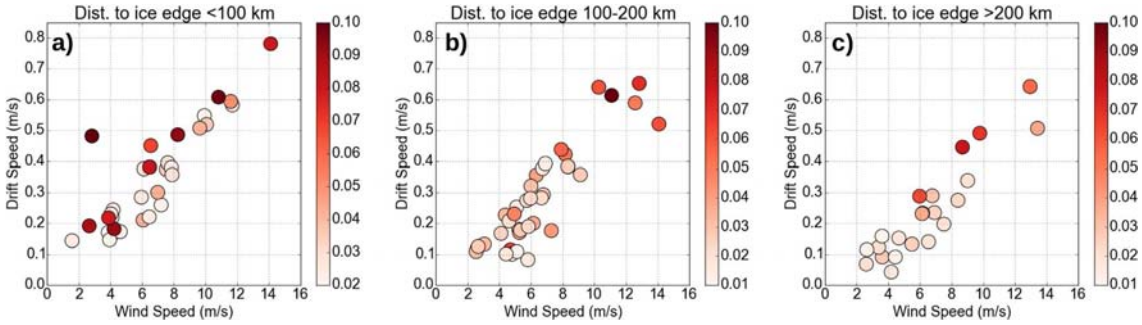

Figure 6. Relation between wind and drift speed and corresponding total deformation rate. Circles denote the daily average of wind and drift speed, and the color of the circles shows the corresponding total deformation rate. The data are divided into three clusters with respect to the distance to the ice edge: (a) $l < 100$ km, (b) 100 km $< l < 200$ km, and (c) $l > 200$ km.

deformation process due to lower internal stress and increased impact of swell. Therefore, we found it necessary to consider the distance to the ice edge when we examined the dependence of deformation rates on wind and drift speed. We divided the data into three clusters with respect to the distance to the ice edge: $l < 100$ km, 100 km $< l < 200$ km and $l > 200$ km. Figure 6 shows the relation between wind and drift speed, and the corresponding value of total deformation rate for these three clusters of l. All the values are daily averages. In all three clusters (0–100 km, 100–200 km and over 200 km), wind and drift speed show high correlation (0.88, 0.85 and 0.91, respectively). However, the drift to wind ratio, the wind factor, decreases as the distance to the ice edge increases. The average wind factors of the three clusters are 0.05, 0.04 and 0.03, respectively. These values are high, probably increased by the surface current in the region [*Quadfasel et al*., 1987]. Even deepest in the ice pack, $l > 200$, the obtained wind factor is greater than typical estimates for free drift (2.5% of surface wind [*Leppäranta*, 2005]). The highest daily deformation rates are found closest to the ice edge. This cluster with the shortest distance to the ice edge ($l < 100$ km) differs from the two others also when we compare the conditions leading to high deformation rates. With 100 km $< l < 200$ km and $l > 200$ km, the high deformation rates were connected to high wind and drift speed, but with $l < 100$ km very intense deformation occurred also with low wind and drift speed. This difference may be enhanced as the data in the cluster with $l < 100$ km is largely from late spring.

In addition to the wind speed, the wind direction may have a significant impact on sea ice deformation. Figure 7 shows the daily mean wind speed and direction, and the corresponding net divergence, shear and total deformation rate. The data are clustered with respect to the distance to the ice edge, similarly to Figure 6, described above. Overall, there is no prominent connection between wind direction and sea ice deformation rate. As described earlier, in the cluster closest to the ice edge ($l < 100$ km) intense deformation was observed even with low wind speed (Figure 6). Figure 7 shows that these events of intense deformation occurred also with varying wind directions. In this cluster, we can not see any significant wind direction dependence, not even in the divergence. Deeper in the ice pack (100 km $< l < 200$ km and $l > 200$ km), some level of dependence on the wind direction appears, as the most intense deformation occurred when wind was directed from $\sim 310^\circ$ to 20°. These northerly winds mean situations of wind blowing from the central ice pack toward the open ocean. In the distance of 100–200 km from the ice edge, the majority of significant divergence occurred during these northerly winds. In the cluster of $l > 200$ km, the net divergence was generally very low, and the situation was contrary: the only day with significant divergence had southerly wind, while the highest convergence occurred during northerly wind. However, when interpreting the results in Figure 7, we have to keep in mind that for the high wind speeds, all wind directions are not equally represented.

4.2. Length and Time Scale Dependency

Sea ice deformation is known to be a highly localized and intermittent process. The total deformation rate, ϵ_{tot}, follows the power law with respect to both the length (L) and time scale (τ): $\epsilon_{tot} \sim L^{-\beta}$ and $\epsilon_{tot} \sim \tau^{-\alpha}$. Also, the length scale dependency of sea ice deformation rate depends on the time scale in which it is studied, and similarly the time scale dependency depends on the length scale considered [*Rampal et al*., 2008].

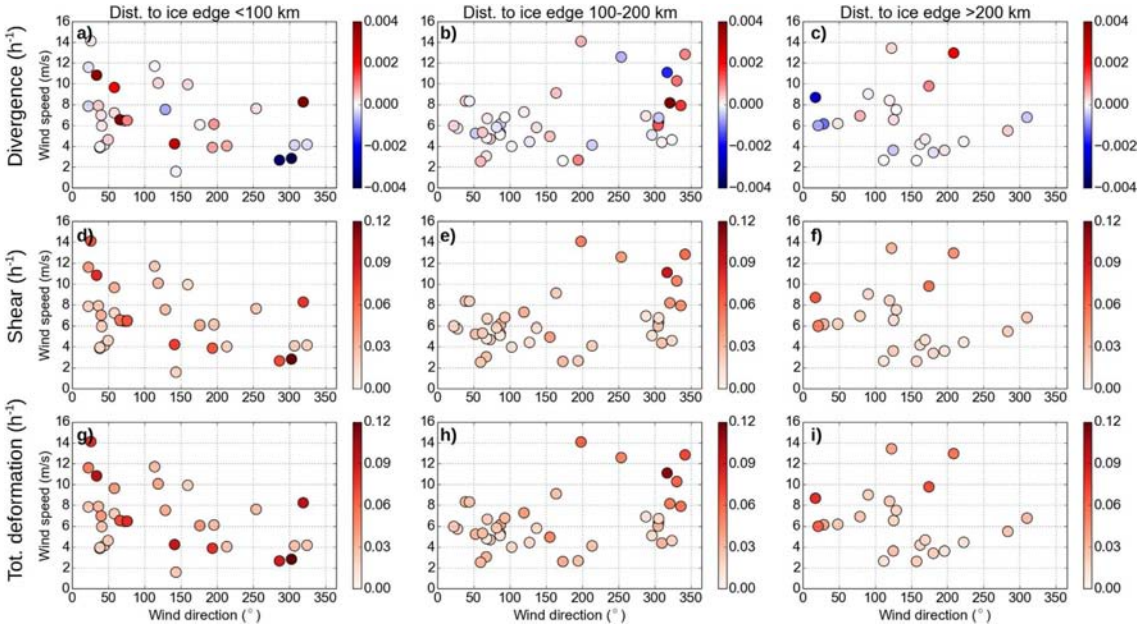

Figure 7. The daily mean wind speed and direction, and the corresponding net divergence (color of the circles in Figures 7a–7c), shear (color of the circles in Figures 7d–7f) and total deformation rate (color of the circles in Figures 7g–7i). The data are divided into three clusters with respect to the distance to the ice edge: (a, d, g) $l < 100$ km, (b, e, h) 100 km $< l <$ 200 km, and (c, f, i) $l >$ 200 km.

Therefore, $\beta = \beta(\tau)$ and $\alpha = \alpha(L)$. As we calculated the deformation rate using 6 different size groups of triangles and 5 different time intervals, we can study these dependences.

The majority of previous studies have examined the length scale dependency and determined β, while the time scale dependency (α) has been discussed less. In the RGPS-based Arctic studies covering length scales from 10 to 1000 km with 3 day time interval, β was found to be in the range of 0.15–0.45 [*Marsan et al*., 2004; *Stern and Lindsay*, 2009]. β has been shown to follow seasonal and regional variation with the greatest magnitudes in the summertime [*Marsan et al*., 2004], and in the areas with a low MYI fraction [*Stern and Lindsay*, 2009]. *Rampal et al*. [2008] studied the deformation from buoy dispersion and covered the length scales of 1–300 km and the time scales of 1 h to 1 month. They showed, that β increases with decreasing time scale and α increases with decreasing length scale.

The exponent β was obtained from a least square fit to the average deformation rates of different-sized triangles in log-log space (Figures 8a and 8b). This was done separately for all the time intervals and the obtained fits of the whole study period are shown in Figure 8c. Both the level of the deformation rate and the length scale dependency decreases clearly with an increasing time interval. As Figure 8d shows, β drops from 0.82 to 0.52 as the time interval increases from 10 min to 24 h, and its value for longer time intervals can be estimated from the line fitted. However, for $\tau = 24$ h, β may be affected by the small size of the study domain, as described in section 3. Therefore, Figure 8d includes two fits: the black dashed line is obtained using all the time intervals (10 min to 24 h) and the red dashed line results from the time intervals from 10 min to 6 h. For $\tau = 3$ d, the time interval of RGPS data, these two fits give β of 0.38 and 0.43.

Total deformation rate of Floes 1, 2 and 3 show similar length scale dependence, although the mean deformation rate was lower for Floe 2. For Floes 1, 2 and 3 β is 0.83/0.74, 0.82/0.72 and 0.84/0.75 for the time interval of 10 min/1 h (Table 1). Floe 4 represents very different conditions from those of the other Floes. As a result, both the deformation rate and the magnitude of β (0.89/0.84 for 10 min/1 h) are greater than for the other Floes. The greater magnitude of β indicates that the internal stress is transmitted over shorter distances, which corresponds well with the behavior of weak summer ice close to the ice edge.

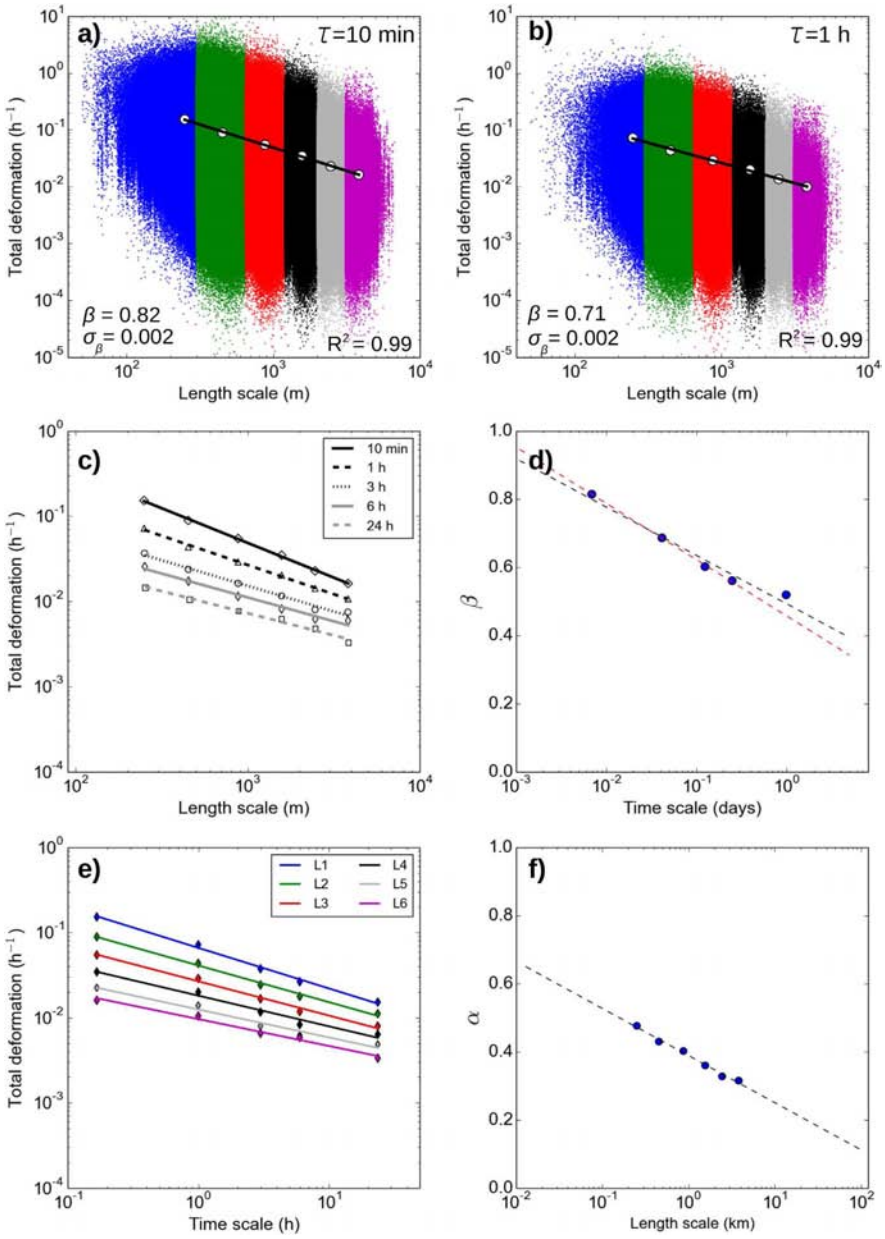

Figure 8. The total deformation rate (h^{-1}) of different-sized triangles with (a) 10 min and (b) 1 h time interval. Different triangle size groups are presented with different colors, and white circles denote the averages of the groups. Black lines show the least squares fits of the average deformation rates in log-log space. The uncertainty of β, σ_β, is estimated using the bootstrap method (with 10,000 repetitions) as a standard deviation of values obtained by bootstrap repetitions. (c) The obtained least square fits for all the time intervals (10 min, 1 h, 3 h, 6 h, and 24 h) and (d) the magnitudes of β. For all these fits, the square correlation $R^2 \geq 0.97$. (e) The mean deformation rates of each size group at different time intervals, and the least square fits (colors of the lines correspond to the colors in a and b). For all these fits, the square correlation $R^2 \geq 0.98$. (f) The exponents of fitted lines in Figure 8e.

Table 1. The Mean Deformation Rate, ϵ_{tot} (h^{-1}), and the Power Law Scaling Exponent β of the Ice Floes 1–4 Period

		Floe 1	Floe 2	Floe 3	Floe 4
10 min	ϵ_{tot} (h^{-1})	0.073	0.059	0.071	0.140
	β/σ_β	0.83/0.001	0.82/0.004	0.84/0.001	0.89/0.003
1 h	ϵ_{tot} (h^{-1})	0.036	0.026	0.034	0.080
	β/σ_β	0.74/0.004	0.72/0.009	0.75/0.004	0.84/0.008

Note: σ^β is the uncertainty of β.

An impact of distance to the ice edge *l* was found in the overall deformation rates (Figure 6). We looked for the impact of *l* on the length scale dependence as well. As we wanted to estimate the impact of *l*, we needed to ensure that other factors are not causing bias in the comparison. Therefore, we chose to use data from Floe 1 and 2 only. They both clearly represent winter conditions and show similar length scale dependence. Also, we only included cases when the wind speed was <8 m/s and the air temperature below $-15°$C. Data were divided into three clusters with $l<150$ km, $150<l<200$ km and $l<200$ km. The mean wind speeds of the cases in these clusters were similar: 6.0 m/s, 5.8 m/s and 5.5 m/s, respectively. The corresponding mean air temperatures were $-31°$C, $-33°$C and $-26°$C.

Both the level and the length scale dependence of deformation rate decrease when going deeper into the ice pack (Figure 9). The obtained power law scaling exponents have magnitudes of 0.78, 0.74 and 0.69 ($\tau = 1$ h). The differences between neighboring clusters, 0.04–0.05 are small, but clearly greater than the estimated errors (0.003, 0.007 and 0.006). The difference in the deformation rate level between clusters $l<150$ km and $150<l<200$ km is small, but the cluster with $l>200$ km differs from these two as the overall deformation rate is clearly lower.

In addition to the distance to the ice edge, we wanted to look for the impact of air temperature on deformation rate and length scale dependence. *Oikkonen et al.* [2016] found a quick response to air temperature in small-scale deformations of Baltic Sea ice. This quick response was assumed to be connected to weaker healing of damages during warm days, which lowers the ice pack strength already in a clearly shorter time than the ice mechanical stress responds to changes in air temperature.

The ship radar data represent a large variety of conditions, and, in order to avoid bias caused by other factors, we limited the data included in this analyses to Floe 2, for which the distance to the ice edge remained greater than 200 km. Also, we included only the cases with wind speed of <8 m/s. We conducted power law scaling for three temperature ranges: $T>-10°$C, $-25°$C$<T<-10°$C and $T<-25°$C. The mean wind speed of the cases included in these three clusters are 5.5 m/s, 5.4 m/s and 5.0 m/s, respectively. Also, the mean distance to the ice edge is similar in all three clusters: 226 km, 240 km and 235 km.

The level of deformation rate is clearly lowest during the coldest days with $T<-25°$C (Figure 10). The difference between two other clusters is small, but again colder days show lower deformation rates. The power law scaling exponent does not show any trend. The obtained values are 0.77, 0.79 and 0.78 ($\tau = 1$ h)

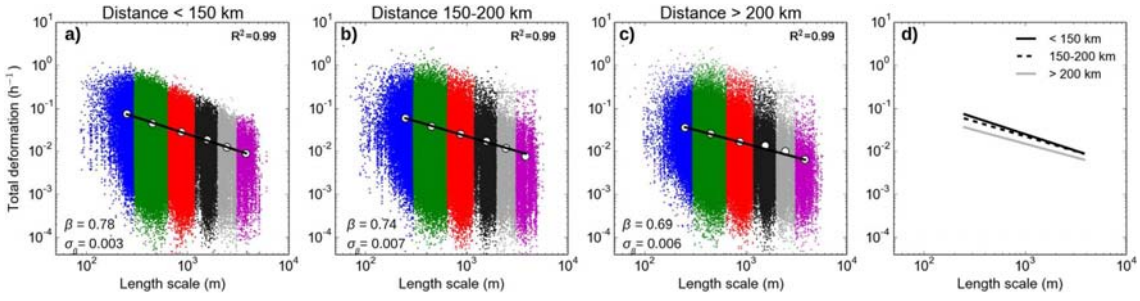

Figure 9. (a–c) Power law scaling of deformation rate with varying distance to the ice edge *l* (Floe 1 and 2). The comparison is made for three clusters with different *l*: $l<150$ km, $150<l<200$ km, and $l>200$ km. Deformation rates are calculated with 1 h time step. Different triangle size groups are presented with different colors, and white circles denote the averages of the size groups. Black lines show the least squares fits of the average deformation rates in log-log space. 95% confidence interval of the fit is shown with white dashed lines. The uncertainty of β, σ_β, is estimated using the bootstrap method (with 10,000 repetitions) as a standard deviation of values obtained by bootstrap repetitions. In the analyses, only the cases with wind speed <8 m/s and air temperature $<-15°$C were included. All the obtained slopes are shown in Figure 9d.

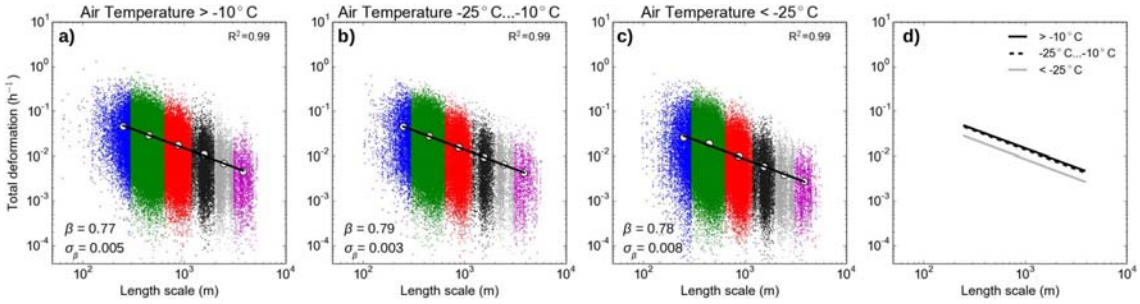

Figure 10. (a-c) Power law scaling of deformation with varying air temperature T (Floe 2). The comparison is made for three cluster with different T: $T > -10°C$, $-25°C < T < -10°C$ and $T < -25°C$. Deformation rates are calculated with 1 h time step. Different triangle size groups are presented with different colors, and white circles denote the averages of the size groups. Black lines show the least squares fits of the average deformations in log-log space. 95% confidence interval of the fit is shown with white dashed lines. The uncertainty of β, σ_β, is estimated using the bootstrap method (with 10,000 repetitions) as a standard deviation of values obtained by bootstrap repetitions. In the analyses, only the cases with wind speed < 10 m/s were included. All the obtained slopes are shown in Figure 10d.

for the three clusters from the warmest to the coldest. During Floe 2, the air temperature alternated between $-35°C$ and $0°C$ (Figure 3). The data in all three temperature clusters consist of 3–4 periods, each of them lasting 1–4 days only. Thus, the observed differences in the level of deformation rate (Figure 10d) reflect the response to air temperature in a time scale of $\lesssim$ few days, and, therefore, are more likely connected to the effectiveness of the healing process rather than to the changes in the ice mechanical strength.

4.3. Localization of Deformations

Power law scaling of the total deformation rate shows how the deformation rate depends on the length scale (Figures 8–10), reflecting the localized nature of the sea ice deformation. The localization of deformations can be studied by calculating the fractional area A_f (the percentage of the total area) that accommodates a certain percentage of the largest deformation rates. This approach has been used in *Stern and Moritz* [2002] and *Marsan et al.* [2004]. We follow this approach, but in addition the overall mean value of the fractional area, we look for the connection between localization and intensity of deformations. Also, we study the localization separately for total deformation rate, shear and absolute divergence, and with several time intervals.

We conducted the localization analysis only for Floe 1 and 2, which represent fairly similar winter conditions and show similar length scale dependence (β=0.83/0, 74 and β=0.82/0.72 for 10 min/1 h, respectively). A_f was calculated for each day from all the triangles with $L < 2000$ m, separately for all the time intervals from 10 min to 24 h. The mean values of A_f of all time intervals are shown with blue circles in Figure 11 for the

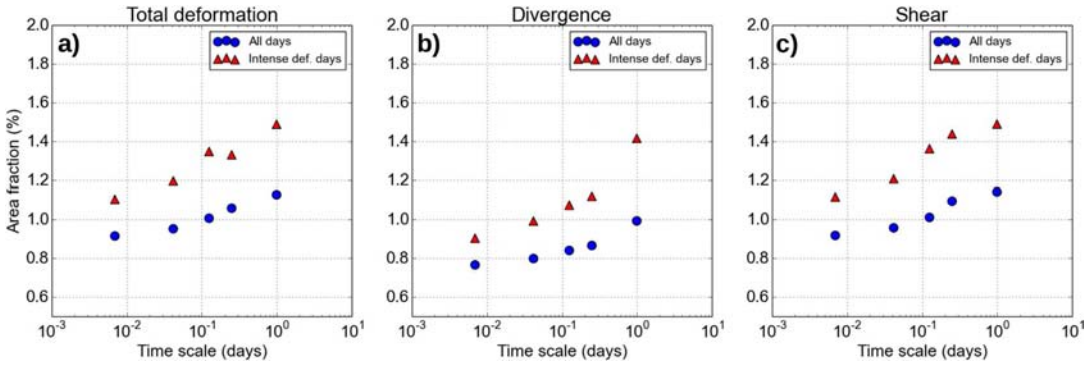

Figure 11. The fractional area that accommodates the largest 15% of (a) overall total deformation rate, (b) absolute divergence and (c) shear. The fractional area is calculated with the time intervals of 10 min, 1 h, 3 h, 6 h and 24 h. Examination is conducted separately for the whole data of Floes 1 and 2, and for the days of intense deformation (determined as days when the mean deformation rate was > 1.5 times the whole period mean).

total deformation rate (a), absolute divergence (b) and shear (c). For all these, the fractional area increase with increasing time interval, meaning that the localization of the sea ice deformation is captured better with smaller time intervals. These values are close to the fractional area (1.6%) reported for the length scales of 13–20 km by *Marsan et al*. [2004], but clearly larger than their estimation for smaller length scales. However, their values represent an Arctic-wide average in a time scale of days, while our results reflect very local conditions.

In addition to the time scale, localization depends also on the level of deformation rate. Red triangles in Figure 11 denote A_f during the days of intense deformation, defined as days when the mean deformation rate was >1.5 times the whole period mean. In all the time scales studied, A_f is increased during the days of intense deformation. This is found in the total deformation rate as well as in the shear and divergence. Deformations are less localized at the times of intense deformations. This indicates that the increase in the mean deformation rate results from an increase in the number of cells with significant deformation, rather than from an increase in the deformation rate of the cells with the largest deformations.

The time series in Figures 2 and 3 show how the level of divergence is clearly lower than the level of shear. Figure 11 reveals that these two types of deformations differ also in terms of localization: divergence is generally a more localized process than shear.

5. Discussion

Our largest length ($\sim$5 km) and time scales (24 h) are smaller than covered in RGPS-based studies of Arctic sea ice deformation [*Marsan et al*., 2004; *Stern and Lindsay*, 2009]. However, when we know how total deformation rate depends on the length and time scale, we can compare our results with these previous ones. When we extrapolate the length scale dependences obtained for 1 h and 24 h interval (Figure 8c) up to $L \approx 10$ km, we get a prediction of total deformation rate of 0.12 day^{-1} and 0.05 day^{-1} for these time intervals, respectively. These values are on a comparable level with the ones found in the Weddell Sea from the buoys with $\tau = 1$ h [*Hutchings et al*., 2012] and in the Arctic from the RGPS data with $\tau = 3$ days [*Marsan et al*., 2004; *Stern and Lindsay*, 2009] for the same length scale.

During the N-ICE2015 campaign, also buoy arrays with the length scales from 2 to 100 km were deployed [*Itkin et al*., 2015]. R/V Lance and our study area were located in the center of the arrays. The time series of deformation rate obtained from the buoy arrays cover the duration of Floe 1 and 3. During the duration of Floe 1, the smallest length scales of the buoy array ($L \sim$ 5–10 km) and the largest scales of the ship radar data ($L \sim$ 2–5 km, $\tau = 1$ h) had a same mean deformation rate, 0.01 h^{-1}. During the duration of Floe 3, these two data sets showed very different results: the mean deformation rate of 0.06 h^{-1} from the buoy array and 0.01 h^{-1} from the ship radar data. Also, the divergence of the buoy array showed a distinct oscillation with subdaily periodicity, possibly a tidal signal [*Itkin et al*., 2017], which was not found in the deformation rate time series from the ship radar. As described in section 4.1, during Floe 3 the drift speed was fairly high, but the ice pack in the ship radar range was largely drifting coherently. Excluding the intense deformation periods at the beginning and at the end of Floe 3, the differential motion in the ship radar range was mainly limited to action at one lead. This peculiar behavior is very likely associated to the vicinity of the ice edge, since such a long period ($\sim$ 1 month) with high drift speed but no significant deformation would be unlikely to occur in the central ice pack. The simultaneous buoy array covered a larger area than the ship radar images and captured more deformations. Therefore, we believe that during Floe 3 the very local conditions were dominating, and thus the results differ clearly from the deformation observed with the larger scale buoy array.

The length scale dependence of deformation rate was found to strongly depend on the time scale (Figure 8d). Similar behavior was reported by *Rampal et al*. [2008]. From the Arctic RGPS data, β has been found to be in the range of 0.15–0.45, with the greatest magnitude in the summertime [*Marsan et al*., 2004], and in the areas with a low MYI fraction [*Stern and Lindsay*, 2009]. For $\tau = 3$ d, the time interval of RGPS data, the two fits in Figure 8d give β of 0.38 and 0.43. These values represent thin first and second year ice, and can be compared to the higher end of the β range of RGPS studies. Thereby, the magnitude of β found for τ of 10 min to 24 h is in good agreement with the results reported for $\tau = 3$ days in *Marsan et al*. [2004] and *Stern and Lindsay* [2009]. This also indicates, that the length scale dependence that previously has been found for $L \sim$ 10–1000 km [*Marsan et al*., 2004; *Stern and Lindsay*, 2009] extends down to 50 m. On the other

hand, all the values of $\beta(\tau=1$ h) reported here (0.68–0.84) are of clearly greater magnitude than what was found in the Weddell Sea from the buoy array with 1 h time interval and covering $L \sim$ 5–50 km (β=0.21) [*Hutchings et al*., 2012].

Simultaneous N-ICE2015 buoy arrays ($\tau = 1$ h) showed somewhat smaller values of β (0.37–0.54) [*Itkin et al*., 2017] than the ship radar data. Also, the buoy arrays showed a clear seasonal pattern with an increasing magnitude of β from winter to summer [*Itkin et al*., 2017], which we cannot find in the small-scale deformations in the ship radar range. The transition from winter to spring conditions occurred during Floe 3 as the air temperature showed a clear increase from mid-May onward (Figure 4). However, as described earlier, the very local conditions were dominating for Floe 3 and the seasonal signal remained thereby hidden.

Previous studies have concluded that the majority of deformation is brittle in the central Arctic [*Marsan et al*., 2004; *Rampal et al*., 2008; *Stern and Lindsay*, 2009]. The failure of sea ice is found to transit from ductile to brittle when the strain rate $\epsilon_{total} > 10$ day^{-1} [*Weiss*, 2013]. By downscaling the obtained length scale dependence of Floe 2, which represent conditions closest to the central Arctic, we find the mean deformation rate exceeding 10 day^{-1}, the transition from ductile to brittle behavior, when $L <\sim 10$ m for $\tau = 1$ h. *Marsan and Weiss* [2010] showed that another feature of brittle deformation is a space/time scaling symmetry, $\beta(\tau) \sim -c\ln(\tau)$ and $\alpha(L) \sim -c\ln(L)$, where c represents the strength of the coupling. This type of symmetry is found also in Figures 8d and 8f, where both black slopes show a trend of $c = 0.06$ which is close to value (0.10) presented by *Marsan and Weiss* [2010] for larger scale buoy disepersion.

The MIZ differs clearly from the central ice pack, and the mechanical behavior changes from elasto-brittle to more granular-like [*Weiss*, 2013]. Since the granular medium, the assembly of floes, can still transmit forces, the deformation rates follow the power law scaling [*Weiss*, 2013]. This is the case for Floe 4, which clearly represents the MIZ: the deformation rates are found to exhibit scaling, but with exponent β of high magnitude (0.84 for $\tau = 1$ h), indicating that forces are transmitted over shorter distances.

6. Conclusions

We studied sea ice deformation using ship radar images recorded onboard R/V Lance during the N-ICE2015 campaign. With the ship radar data we were able to calculate deformation rates on smaller length and time scales than those previously studied in the Arctic. Also, the ship radar images provide valuable new information about the structure and history of the ice pack. The deformation history of an ice floe was found to have a strong influence on further deformations as the deformation events were initialized along the lines of previous damages. Despite of the healing process, LDs remained weaker than thermodynamically grown level ice, even during the coldest winter.

Deformation rate was calculated using 5 different time intervals and 6 different length scales. The sea ice deformation rate shows strong dependence on both time and length scale. The mean total deformation rate with 1 h time interval is approximately 50%, and the mean with 24 h time interval approximately 10%, of the mean total deformation rate obtained with 10 min interval. For Floes 1–3 we obtained mean deformation rates in the range of 0.06–0.07 h^{-1} for interval of 10 min and 0.03–0.04 h^{-1} for interval of 1 h. When considering the obtained time and length scale dependency of the deformation rate, we can conclude that these values are on a comparable level with the ones previously reported in the Arctic [*Marsan et al*., 2004; *Stern and Lindsay*, 2009; *Rampal et al*., 2008] and Antarctic [*Hutchings et al*., 2012]. Floe 4 differed from other Floes and represents the MIZ. Consequently, the mean deformation rate was approximately double compared to the other Floes (0.140 h^{-1} and 0.08 h^{-1} with time intervals of 10 min and 1 h). Deep in the winter ice pack ($l > 200$ km), high deformation rates occurred only with high wind and drift speed, while in the MIZ they were found also during calm wind and drift conditions.

Overall, we can conclude that sea ice deformation rate exhibits scaling properties with respect to length and time scale even on this small length scales ($\sim$ 50 m to 5 km) and in very local domains (15 km $\times$15 km). Also, the length scale dependence of deformation rate depends strongly on the time scale. For the entire study period, the power law scaling exponent β was found to drop from 0.82 to 0.52 with the time interval increasing from 10 min to 24 h. For the time scale of 3 days, which is used in RGPS-based studies, our results predict β of approximately 0.4, which is in good agreement with results of *Marsan et al*. [2004]

and *Stern and Lindsay* [2009]. This indicates, that the length scale dependence that previously has been found for $L \sim 10$–1000 km [*Marsan et al*., 2004; *Stern and Lindsay*, 2009] extends down to 50 m.

However, contrary to *Stern and Lindsay* [2009] and simultaneous buoy array, we did not find a seasonal signal in the length scale dependence, and β of Floes 1, 2 and 3 was very similar (0.82–0.84 for 10 min interval and 0.72–0.75 for 1 h interval). We believe this is due to the small size of the sampling area, as the seasonal signal was hidden under dominating local conditions. For Floe 4 in the MIZ we obtained β of clearly greater magnitude (0.89 and 0.84 for intervals of 10 min and 1 h).

Acknowledgments
We are very grateful to the two anonymous reviewers. Their comments inspired us to include the examination of different time scales into this paper. This work has been supported by the Norwegian Polar Institute's Centre for Ice, Climate and Ecosystems (ICE) through the N-ICE project. The work of A. Oikkonen was funded by Academy of Finland project 279310. P. Itkin was supported by the Norwegian Polar Institutes Centre for Ice, Climate and Ecosystems (ICE) through the N-ICE project and by ID Arctic (funded the by Norwegian Ministries of Foreign Affairs and Climate and Environment, programme Arktis 2030). We want to acknowledge Image Soft and especially Ari Niemi for radar server development. Data used in this study are publicly available at the Norwegian Polar Data Centre: ship radar images [*Haapala et al*., 2017], meteorological data [*Hudson et al*., 2015] and snow and ice thickness [*Rösel et al*., 2016].

References

Bekryaev, R. V., I. V. Polyakov, and V. A. Alexeev (2010), Role of polar amplification in long-term surface air temperature variations and modern arctic warming, *J. Clim.*, *23*, 3888–3906, doi:10.1175/2010JCLI3297.1.

Bouillon, S., and P. Rampal (2015a), On producing sea ice deformation data sets from SAR-derived sea ice motion, *Cryosphere*, *9*, 663–673, doi:10.5194/tc-9-663-2015.

Bouillon, S., and P. Rampal (2015b), Presentation of the dynamical core of neXtSIM, a new sea ice model, *Ocean Modell.*, *91*, 23–37, doi:10.1016/j.ocemod.2015.04.005.

Cohen, L., S. R. Hudson, V. P. Walden, R. M. Graham, and M. A. Granskog (2017), Meteorological conditions in a thinner Arctic sea ice regime from winter through summer during the Norwegian young sea ICE expedition (N-ICE2015), *J. Geophys. Res. Atmos.*, doi:10.1002/2016JD026034, in press.

Comiso, J. C. (2012), Large decadal decline of the Arctic multiyear ice cover, *J. Clim.*, *25*, 1176–1193, doi:10.1175/JCLI-D-11-00113.1.

Granskog, M. A., P. Assmy, S. Gerland, G. Spreen, H. Steen, and L. H. Smedsrud (2016), Arctic Research on thin ice: Consequences of Arctic sea ice loss, *Eos Trans. AGU*, *97*, 97, doi:10.1029/2016EO044097.

Haapala, J., A. Oikkonen, A. Gierisch, P. Itkin, M. Nicolaus, G. Spreen, C. Wang, J. Karvonen, and M. Lensu (2017), *N-ICE2015 Ship Radar Images*, Norw. Polar Inst., Tromsö, Norway, doi:10.21334/npolar.2017.6441ca81.

Hudson, S., L. Cohen, and V. Walden (2015), *N-ICE2015 Surface Meteorology v2*, Norw. Polar Inst., Tromsö, Norway, doi:10.21334/npolar.2015.056a61d1.

Hutchings, J. K., P. Heil, and D. Hibler (2005), Modeling linear kinematic features in sea ice, *Mon. Weather Rev.*, *133*, 3481–3497, doi:10.1175/MWR3045.1.

Hutchings, J. K., A. Roberts, C. A. Geiger, and J. Richter-Menge (2011), Spatial and temporal characterisation of sea ice deformation, *Ann. Glaciol.*, *52*, 360–368, doi:10.3189/172756411795931769.

Hutchings, J. K., P. Heil, A. Steer, and D. Hibler (2012), Subsynoptic scale spatial variability of sea ice deformation in the western Weddell Sea during early summer, *J. Geophys. Res.*, *117*, C01002, doi:10.1029/2011JC006961.

Itkin, P., et al. (2015), *N-ICE2015 Buoy Data*, Norw. Polar Inst., Tromsö, Norway, doi:10.21334/npolar.2015.6ed9a8ca.

Itkin, P., et al. (2017), Thin ice and storms: Sea ice deformation from buoy arrays deployed during N-ICE2015, *J. Geophys. Res. Oceans*, doi:10.1002/2016JC012403, in press.

Karvonen, J. (2016), Virtual radar ice buoys—A method for measuring fine-scale sea ice drift, *Cryosphere*, *10*, 29–42, doi:10.5194/tc-10-29-2016.

Kwok, R. (1998), The RADARSAT geophysical processor system, in *Analysis of SAR Data of the Polar Oceans: Recent Advances*, edited by C. Tsatsoulis and R. Kwok, pp. 235–257, Springer, Berlin, Germany.

Kwok, R., and D. A. Rothrock (2009), Decline in Arctic sea ice thickness from submarine and ICESat records: 1958–2008, *Geophys. Res. Lett.*, *36*, L15501, doi:10.1029/2009GL039035.

Kwok, R., E. C. Hunke, W. Maslowski, D. Menemenlis, and J. Zhang (2008), Variability of sea ice simulations assessed with RGPS kinematics, *J. Geophys. Res.*, *113*, C11012, doi:10.1029/2008JC004783.

Leppäranta, M. (2005), *The Drift of Sea Ice*, Praxis Publ. Ltd, Chichester, U. K.

Marsan, D., and J. Weiss (2010), Space/time coupling in brittle deformation at geophysical scales, *Earth Planet. Sci. Lett.*, *296*, 353–359, doi:10.1016/j.epsl.2010.05.019.

Marsan, D., H. Stern, R. Lindsay, and J. Weiss (2004), Scale dependence and localization of the deformation of Arctic Sea Ice, *Phys. Res. Lett.*, *93*, 17, 178501, doi:10.1103/PhysRevLett.93.178501.

Oikkonen, A., J. Haapala, M. Lensu, and J. Karvonen (2016), Sea ice drift and deformation in the coastal boundary zone, *Geophys. Res. Lett.*, *43*, 10,303–10,310, doi:10.1002/2016GL069632.

Quadfasel, D., J. C. Gascard, and K.-P. Koltermann (1987), Large-scale oceanography in Fram Strait during the 1984 Marginal Ice Zone experiment. *J. Geophys. Res. 92*(C7), 6719–6728, doi:10.1029/JC092iC07p06719.

Rampal, P., J. Weiss, D. Marsan, R. Lindsay, and H. Stern (2008), Scaling properties of sea ice deformation from buoy dispersion analysis, *J. Geophys. Res.*, *113*, C03002, doi:10.1029/2007JC004143.

Rampal, P., J. Weiss, and D. Marsan (2009), Positive trend in the mean speed and deformation rate of Arctic Sea ice, 1979–2007, *J. Geophys. Res.*, *114*, C05013, doi:10.1029/2008JC005066.

Renner, A. H. H., S. Gerland, C. Haas, G. Spreen, J. F. Beckers, E. Hansen, M. Nicolaus, and H. Goodwin (2014), Evidence of Arctic sea ice thinning from direct observations, *Geophys. Res. Lett.*, *41*, 5029–5036, doi:10.1002/2014GL060369.

Rösel, A., et al. (2016), *N-ICE2015 Total (Snowand Ice) Thicknessdata From em31*, Norw. Polar Inst., Tromsö, Norway, doi:10.21334/npolar.2016.70352512.

Serreze, M. C., A. P. Barret, J. C. Stroeve, D. N. Kindig, and M. M. Holland (2009), The emergence of surface-based Arctic amplification, *Cryosphere*, *3*, 11–19, doi:10.5194/tc-3-11-2009.

Spreen, G., R. Kwok, and D. Menemenlis (2011), Trends in Arctic sea ice drift and role of wind forcing: 1992–2009, *Geophys. Res. Lett.*, *38*, L19501, doi:10.1029/2011GL048970.

Stern, H. L., and R. W. Lindsay (2009), Spatial scaling of Arctic sea ice deformation, *J. Geophys. Res.*, *114*, C10017, doi:10.1029/2009JC005380.

Stern, H. L., and R. E. Moritz (2002), Sea ice kinematics and surface properties from RADARSAT synthetic aperture radar during the SHEBA drift, *J. Geophys. Res.*, *107*(C10), 8028, doi:10.1029/2000JC000472.

Weiss, J. (2013), *Drift, Deformation and Fracture of Sea Ice*, *Springer Brief Earth Sci.*, Springer, Netherlands, doi:10.1007/978-94-007-6202-2.

FINNISH METEOROLOGICAL INSTITUTE
Erik Palménin aukio 1
P.O. Box 503
FI-00101 HELSINKI
tel. +358 29 539 1000
WWW.FMI.FI

FINNISH METEOROLOGICAL INSTITUTE
CONTRIBUTIONS No. 138
ISBN 978-952-336-034-1 (paperback)
ISSN 0782-6117
Erweko
Helsinki 2017

ISBN 978-952-336-035-8 (pdf)
Helsinki 2017